

# **Low speed aerofoil optimisation (versão final após defesa)**

**Ricardo Jorge Faria Palmeira**

Dissertação para obtenção do Grau de Mestre em  
**Engenharia Aeronáutica**  
(Ciclo de estudos integrado)

Orientador: Prof. Doutor Pedro Vieira Gamboa

**março de 2022**



# **Dedication**

To my family for their encouragement, patience and support.  
To my friends for helping me in this journey and for all the moments  
we spent together.



# Resumo

A topologia de perfis aerodinâmicos tem uma influência significativa no desempenho de aeronaves. Múltiplas metodologias podem ser aplicadas para definir perfis, tais como projeto direto, projeto inverso ou projeto por desempenho. Com o desenvolvimento da tecnologia computacional, tem havido uma tendência contínua para automatizar o projeto de perfis utilizando projeto por desempenho e algoritmos de otimização formais. A parametrização de perfis tem avançado lado a lado, alguns exemplos são B-Spline, funções de tipo morfológicas, funções de Hicks-Henne e Bezier-PARSEC 3333. As principais comparações entre estes métodos têm-se focado na morfologia, espaço de projeto e consistência aerodinâmica.

No presente trabalho, os tipos de parameterização mencionados são utilizados para otimização de perfis e uma comparação é feita para diferentes números de variáveis com o objetivo de avaliar diferenças para a otimização. Projeto por desempenho é utilizado numa abordagem multi-ponto nesta dissertação, com uma função objetivo de agregação de pesos determinados via dados de projeto da aeronave, para maximizar a pontuação para a competição Air Cargo Challenge (ACC2019 e ACC2022), através do uso da ferramenta XFOIL para análise aerodinâmica e otimização por enxame de partículas sobre uma versão modificada da ferramenta XOPTFOIL. O perfil inicial foi obtido via projeto inverso de forma iterativa durante trabalhos anteriores. A otimização inclui a corda do flap e o ângulo de deflexão para diferentes condições de voo como variáveis de projeto. A população inicial é delimitada por limites máximos e mínimos determinados através das variáveis de projeto do perfil inicial e uma perturbação inicial.

O perfil é constrangido pelas máxima e mínima espessuras, um ângulo de bordo de fuga mínimo e uma espessura de bordo de fuga fixa. Outras restrições adicionais são também impostas ao perfil para evitar a análise desnecessária de geometrias cujo solução do XFOIL não converge. Estas incluem os ângulos máximos, mínimos e a diferença dos dois pontos mais próximos ao bordo de ataque, o ângulo máximo entre quaisquer três pontos ao longo do perfil e o número máximo de mudanças de sinal da curvatura do perfil na superfície superior e inferior. Para lidar com estes constrangimentos e restrições utilizou-se uma função de penalidade com valores normalizados. De forma a garantir que estas não restringem o domínio de exploração da otimização, um limite dinâmico é aplicado à função penalidade. Este diminui linearmente durante a otimização.

A partir de dois casos de estudo é possível demonstrar a capacidade de otimização da ferramenta. No primeiro, o uso de B-Splines alcançou melhores resultados comparativamente aos outros métodos. No segundo, o limite dinâmico, método para consistência e método de recuperação de convergência para a ferramenta XFOIL são estudados. Tendo este último o maior efeito na otimização.

# Palavras chave

Projeto de perfis, otimização de formas aerodinâmicas, otimização por enxame de partículas, métodos de parametrização de perfis, otimização multi-ponto

# Abstract

Aerofoil shape has a significant influence on aircraft performance. Multiple methodologies can be applied, such as direct design, inverse design or performance design. With the improvement of computer technology there has been a continuing trend of automating this process by using performance-based methods and formal optimisation algorithms. Parametrization formulations of aerofoils have continually advanced, some examples are B-Spline, Class Shape Functions, Hicks-Henne functions and Bezier-PARSEC 3333. Main comparisons of parametrizations have focussed on morphology, design space and aerodynamic consistency.

In the present work, the parametrizations mentioned are applied to aerofoil optimisation and their results compared for different numbers of design variables, in order to ascertain optimisation differences. Performance design optimisation is used in a multi-point approach with an aggregated objective function using weights that are determined using the aircraft design data, to maximize the score for the competition Air Cargo Challenge (ACC2019 and ACC2022), using XFOIL for aerodynamic analysis and particle swarm optimisation (PSO) under a modified version of the XOPTFOIL tool. The initial aerofoil was obtained by iterative inverse design during previous works, the optimisation includes the flap chord and deflection angle for the different selected lift coefficient conditions as design variables. The initial population is bounded between maximum and minimum limits set by the initial aerofoil design variables and an initial perturbation.

The aerofoil is constrained by minimum and maximum thicknesses, a minimum trailing edge angle and a specified trailing edge thickness. Several additional restrictions are also imposed on the aerofoil to avoid unneeded analysis of a geometry with an expected non converged solution in XFOIL. These include the angles' maximum, minimum and difference values of the two points closest to the leading edge, the maximum angle between any three consecutive points and the number of curvature sign reversals at the upper surface and lower surface of the aerofoil. To deal with the constraints and restrictions a penalty function is used, each penalty being normalised by a maximum set value. To ensure that these do not unduly constrain the domain exploration of the optimisation, a dynamic limit to the penalties is used. During the optimisation, this limit decreases linearly with the iterations.

From two case studies, it was possible to demonstrate the tool ability to optimize aerofoils. In the first case, utilisation of B-Splines achieved better results relative to the other methods. In the second case, the dynamic limit, consistency method and XFOIL convergence recuperation method are studied. This last one has the greatest influence on optimisation.

## Keywords

Aerofoil design, aerodynamic shape optimisation, particle swarm optimisation, aerofoil parametrization methods, multi-point optimisation





# Contents

<b>1</b>	<b>Introduction</b>	<b>1</b>
1.1	Objective . . . . .	1
1.2	Thesis Outline . . . . .	2
<b>2</b>	<b>Bibliographic Review</b>	<b>3</b>
2.1	Introduction to aerofoil optimisation . . . . .	3
2.2	Aerofoil parametrization . . . . .	6
2.3	Optimisation algorithms . . . . .	10
2.4	Existing tools . . . . .	12
<b>3</b>	<b>Methods</b>	<b>13</b>
3.1	XOPTFOIL . . . . .	13
3.2	Initial transformations . . . . .	15
3.3	Parametrization methods . . . . .	17
3.3.1	Hicks-Henne functions . . . . .	18
3.3.2	Orthogonal NACA functions . . . . .	18
3.3.3	B-Splines . . . . .	19
3.3.4	Class shape functions . . . . .	21
3.3.5	Bezier-PARSEC 3333 . . . . .	22
3.4	Aerofoil evaluation . . . . .	24
3.4.1	Penalties . . . . .	25
3.4.2	XFOIL analysis . . . . .	28
3.4.3	Objective function . . . . .	32
3.4.4	Weight determination . . . . .	33
3.5	Optimisation . . . . .	37
<b>4</b>	<b>Analysis cases</b>	<b>43</b>
4.1	Aircraft parameters and properties . . . . .	43
4.2	Case 1 - Air Cargo Challenge 2019 . . . . .	45
4.2.1	Problem definition . . . . .	45
4.2.2	Relative derivatives - Case 1 . . . . .	48
4.2.3	Optimisation cases and conditions . . . . .	49
4.2.4	Results and discussion . . . . .	50
4.3	Case 2 - Air Cargo Challenge 2022 . . . . .	59
4.3.1	Problem definition . . . . .	59
4.3.2	Relative derivatives - Case 2 . . . . .	62
4.3.3	Optimisation case and conditions . . . . .	62
4.3.4	Results and discussion . . . . .	63
<b>5</b>	<b>Conclusions</b>	<b>73</b>
5.1	Future work . . . . .	74

**Bibliography** 75

**A Full weights equations** 81

A.1 Analysis case 1 . . . . . 81

A.2 Analysis case 2 . . . . . 82

# List of Figures

2.1	Aerofoil characteristics. . . . .	3
2.2	Percentage of aerofoils database within Kulfan tolerance for different parametrization methods by Masters et al. [32]. . . . .	10
2.3	Residuals for different parametrization methods with six design variables for the top surface of the NASA SC(2)-0414 aerofoil by Zhang et al. [33]. . . . .	10
3.1	Modified XOPTFOIL tool flowchart. . . . .	14
3.2	Initial parametrization routine flowchart. . . . .	15
3.3	Aerofoil after transformations. . . . .	16
3.4	Bezier-PARSEC 3333 aerofoil geometry and Bezier control points defined by twelve basic aerodynamic parameters as set by Derksen et al. [24]. . . . .	22
3.5	Aerofoil evaluation flowchart. . . . .	25
3.6	Potential aerofoil thickness distribution and relevant thickness properties for penalty calculation. . . . .	26
3.7	Potential aerofoil thickness distribution near trailing edge and angles for penalty calculation. . . . .	27
3.8	Potential aerofoil upper surface and respective curvature distribution for penalty calculation. . . . .	28
3.9	Flowchart of the Xfoil analysis routine. . . . .	30
3.10	Optimisation algorithm flowchart. . . . .	40
4.1	Aircraft used by the AERO@UBI team in the ACC2019 competition. . . . .	43
4.2	Optimised aerofoils (solid line) and original aerofoil (dashed line) for all study cases. . . . .	52
4.3	Violin graph of all design variables up to iteration 100. Red line marks initial variables and green line the best design variables at iteration 100. . . . .	53
4.4	Design radius during optimisation for all study cases. . . . .	55
4.5	BSP case <i>C</i> polars (solid lines) and original aerofoil polars (dashed lines) for each operating condition near the operating point. . . . .	58
4.6	Optimised aerofoil (solid line) and original aerofoil (dashed line) for case study 2. . . . .	64
4.7	Solution objective function value in red and design radius in black during optimisation. . . . .	65
4.8	Aerofoil evaluation type count for each iteration during optimisation. . . . .	66
4.9	Total aerofoil evaluation type count for the optimisation. . . . .	67
4.10	Violin graph of design variables up to iteration 100 for case 2. . . . .	68
4.11	Take-off properties maximum (in orange), average (in green), minimum (in blue) and global best value (in red) per population for <i>Conv</i> aerofoil evaluation during optimisation. . . . .	69

4.12	Cruise, turn and climb properties maximum (in orange), average (in green), minimum (in blue) and global best value (in red) per population for <i>Conv</i> aerofoil evaluation during optimisation. . . . .	70
4.13	<i>Obj</i> and $\delta$ maximum (in orange), average (in green), minimum (in blue) and global best value (in red) per population for <i>Conv</i> aerofoil evaluation during optimisation. . . . .	70
4.14	Number of particles with a non zero penalty per iteration (blue) and number of particle best with a non zero penalty. . . . .	71

# List of Tables

2.1	Parametrization methods comparison results by Sripawadkul et al. [30]. . . .	9
2.2	Mean squared error (MSE), number of design variables ( $N_{DV}$ ) and merit for each method and aerofoil by Vicente et al. [34]. . . . .	11
4.1	General aircraft parameters and air properties. . . . .	44
4.2	Relevant take-off properties. . . . .	44
4.3	Relevant climb properties. . . . .	44
4.4	Relevant level flight properties. . . . .	45
4.5	Relevant sustained turn properties. . . . .	45
4.6	Values of weights $w_i$ and normalised weights $\bar{w}_i$ used during optimisation. . .	47
4.7	Operating points for case 1. . . . .	47
4.8	Used relative derivatives related to take-off for case 1. . . . .	48
4.9	Used relative derivatives related to flight time for case 1. . . . .	48
4.10	Actual relative derivatives related to take-off for case 1. . . . .	48
4.11	Actual relative derivatives related to flight time for case 1. . . . .	48
4.12	Actual weights for case 1. . . . .	48
4.13	Total number of design variables used in each optimisation case for each parametrization method. . . . .	49
4.14	Initial perturbations for each parametrization method. . . . .	49
4.15	Optimisation constants for analysis case 1. . . . .	49
4.16	XFOIL panelling variables . . . . .	50
4.17	XFOIL initialization analysis parameters. . . . .	50
4.18	Resulting aerofoil properties for each study case. . . . .	50
4.19	Count of the optimisation evaluation type for each optimisation case. . . . .	51
4.20	Resulting flap design variables. . . . .	54
4.21	Aerodynamic properties for the resulting aerofoil of each study case. . . . .	56
4.22	Accuracy of the parametrized original aerofoil. . . . .	56
4.23	Relevant aerodynamic properties for the initial aerofoil and its initial objective value for each case. . . . .	57
4.24	Off-design conditions. . . . .	57
4.25	Values of weights $w_i$ and normalised weights $\bar{w}_i$ used during optimisation for case 2. . . . .	61
4.26	Operating points for case 2. . . . .	61
4.27	Relative derivatives related to take-off. . . . .	62
4.28	Relative derivatives related to climb. . . . .	62
4.29	Relative derivatives related to flight distance. . . . .	62
4.30	Optimisation constants for analysis case 2. . . . .	63
4.31	XFOIL panelling variables . . . . .	63
4.32	XFOIL initialization analysis parameters. . . . .	63
4.33	Resulting aerofoil properties. . . . .	63

4.34	Resulting flap design variables. . . . .	64
4.35	Aerodynamic properties for the resulting aerofoil. . . . .	64
4.36	Number of particles, particle best and global best with a non zero penalty value. . . . .	69
4.37	XFOIL analysis count for the optimisation. . . . .	71
4.38	Total XFOIL analysis and Viscal counts. . . . .	72

# Nomenclature

$A$	Coefficients vector	—
$a$	Coefficient or weight for parametrization	—
$C_l$	Lift coefficient sequence for XFOIL initialization analysis	—
$C$	B-spline coordinates vector	—
$C$	Class function	—
$C_D$	Aircraft drag coefficient	—
$C_d$	Aerofoil drag coefficient	—
$C_L$	Aircraft lift coefficient	—
$C_l$	Aerofoil lift coefficient	—
$C_m$	Aerofoil moment coefficient	—
$C_{d,min,i}$	Minimum drag coefficient for operating point $i$ during optimisation	—
$C_{l,0,init}$	Reference lift coefficient for XFOIL initialization analysis	—
$C_{l,max,i}$	Maximum lift coefficient for operating point $i$ during optimisation	—
$CTERAT$	Trailing edge over leading edge panel density ratio for XFOIL panelling	—
$CTRRAT$	Refining area over leading edge panel density ratio for XFOIL panelling	—
$CVPAR$	Panel bunching parameter for XFOIL panelling	—
$c$	Aerofoil chord	$m$
$c_1$	PSO cognitive acceleration factor	—
$c_2$	PSO social acceleration factor	—
$D$	Drag	$N$

$D_S$	Degree of the Bernstein polynomials	—
$\bar{f}_{naca}$	Expanded NACA modes normalised by the maximum mode	—
$f_{naca}$	Expanded NACA modes	—
$h_1, h_2$	Hicks-Henne parameters	—
$L$	Lift	$N$
$LIPAN, LBLINI$	XFOIL variables indicating boundary layer reinitialization	—
$M$	Least square approximation matrix	—
$M$	Mach number	—
$N_1, N_2$	Class function parameters	—
$N_{functions}$	Number of functions	—
$N_{i,k}$	B-spline basis functions	—
$N_{op}$	Number of operating points	—
$N_{pop}$	Population size	—
$N_{ps}$	Number of points in surface	—
$N_p$	Number of aerofoil points	—
$N_{crit}$	Transition criterion parameter for XFOIL	—
$NPAN$	Number of panels for XFOIL panelling	—
$n_\psi$	Number of aerodynamic properties to optimise	—
$n_\sigma$	Number of operational objectives	—
$N_{cp}$	Number of B-spline control points	—
$n_{init}$	Number of points for XFOIL initialization analysis	—
$Obj$	Objective function	—



$P$	B-spline control points matrix	—
$P_X$	Control points $x$ coordinate vector	—
$P_Z$	Control points $z$ coordinate vector	—
$p$	Non-dimensional sequence for XFOIL initialization analysis	—
$p_{0,init}$	Non-dimensional starting position for XFOIL initialization analysis	—
$prop$	Aerodynamic property	—
$prop_{target}$	Aerodynamic property target	—
$q$	Dynamic pressure	$Pa$
$Re$	Reynolds number	—
$RMSBL$	XFOIL variable indicating convergence value	—
$r$	Design radius	—
$r_t, r_c$	BPP parameters	—
$r_{LE}$	Leading edge radius on thickness curve	—
$S$	Shape function	—
$S$	Wing area	$m^2$
$S_G$	Take-off distance	$m$
$Score$	ACC score	—
$\hat{S}$	Distance flown	$m$
$s$	Aerofoil spline position	—
$T$	Knot vector	—
$T$	Thrust	$N$
$t$	Knot vector corresponding to the aerofoil $x$ coordinates	—

$t_{flight}$	Time flown	$s$
$th_{TE}$	Trailing edge thickness	—
$tol_{drag}$	Drag coefficient tolerance for XFOIL initialization analysis	—
$tol_{lift}$	Lift coefficient tolerance for XFOIL initialization analysis	—
$t$	Knot position	—
$\mathbf{V}$	Particles velocity matrix	—
$V$	Velocity	$m s^{-1}$
$V_f$	Final velocity	$m s^{-1}$
$V_i$	Initial velocity	$m s^{-1}$
$V_{AV}$	Average velocity during acceleration	$m s^{-1}$
$V_{LO}$	Lift-off velocity	$m s^{-1}$
$V_S$	Stall velocity	$m s^{-1}$
$V_V$	Vertical velocity	$m s^{-1}$
$V_W$	Wind velocity	$m s^{-1}$
$V_{ACCEL}$	XFOIL viscous solution acceleration variable	—
$W$	Aircraft weight	$N$
$W_{payload}$	Payload weight	$N$
$\bar{w}_i$	Operating point i normalised weight	—
$w_0$	Initial inertia weight for PSO	—
$w_f$	Final inertia weight for PSO	—
$w_t$	Inertia weight for PSO	—
$w_{rate}$	Inertia weight iteration rate for PSO	—

$w_i$	Operating point i non-normalised weight	—
$\mathbf{X}$	Particles position matrix	—
$\mathbf{X}_{init}$	Initial design variables vector	—
$\mathbf{X}_{max}$	Upper design variables limit vector	—
$\mathbf{X}_{min}$	Lower design variables limit vector	—
$XPREF1, XPREF2$	Lower surface refining area limits for XFOIL panelling	—
$XSREF1, XSREF2$	Upper surface refining area limits for XFOIL panelling	—
$\tilde{x}$	Aerofoil original $\tilde{x}$ coordinates vector	$m$
$\mathbf{x}_{base}, \mathbf{z}_{base}$	Transformed aerofoil coordinates vectors before deformation	—
$\mathbf{x}$	Aerofoil transformed $x$ coordinates vector	—
$\tilde{x}$	Aerofoil original chordwise direction axis	$m$
$x$	Aerofoil transformed chordwise direction axis	—
$x_0^c, x_1^c, x_3^c, x_4^c$	BPP control points $x$ coordinates	—
$x_c$	Maximum camber position	—
$x_t$	Maximum thickness position	—
$\hat{z}$	Vector for least square approximation in CSF	—
$\tilde{z}$	Aerofoil original $\tilde{z}$ coordinates vector	$m$
$\mathbf{z}$	Aerofoil transformed $z$ coordinates vector	—
$\tilde{z}$	Aerofoil original vertical direction axis	$m$
$z$	Aerofoil transformed vertical direction axis	—
$z_0^c, z_1^c, z_3^c, z_4^c$	BPP control points $z$ coordinates	—
$z_c$	Maximum camber value	—

$z_t$	Maximum thickness value	—
$z_{TE}$	Trailing edge vertical displacement	—

### **Greek Letters**

$\alpha$	Angle of attack	deg
$\alpha_0$	Aerofoil original angle of attack	deg
$\alpha_{0,init}$	Reference angle of attack for XFOIL initialization analysis	deg
$\alpha_{TE}$	Trailing edge angle on camber curve	deg
$\alpha$	Angle of attack sequence for XFOIL initialization analysis	deg
$\beta_{TE}$	Trailing edge angle on thickness curve	deg
$\delta$	Total penalty value	—
$\delta_j$	Penalty value for property $j$	—
$\delta_{limit}$	Penalty limit value for each constraint	—
$\gamma_{LE}$	leading edge angle on camber curve	—
$\kappa_c$	Maximum camber curvature	—
$\kappa_t$	Maximum thickness curvature	—
$\mu$	Fluid viscosity	$kg\ m^{-1}\ s^{-1}$
$\mu_G$	Ground friction coefficient	—
$\psi$	Aerodynamic property to optimise	—
$\rho$	Fluid density	$kg\ m^{-3}$
$\sigma$	Operational objective	$m\ or\ N\ or\ s$
$\sigma_j$	Property value	—
$\varphi_i$	Operating point $i$ aerodynamic objective	—

$\xi_{abs}$	Initial absolute pertubation	—
$\xi_{rel}$	Initial relative pertubation	—

### **Superscripts and subscripts**

<i>cruise</i>	Level flight
<i>DV</i>	Design variables
<i>g, best</i>	Global best
<i>i</i>	$i^{th}$ position
<i>j</i>	$j^{th}$ position
<i>k</i>	$k^{th}$ position
<i>LE</i>	Leading Edge
<i>Lo</i>	Lower surface
<i>p, best</i>	Particle best
<i>para</i>	Parametrized
<i>ref</i>	Reference value
<i>Rot</i>	Rotated
<i>s</i>	Surface
<i>spec</i>	Specified value
<i>T</i>	Transposed
<i>t</i>	Optimisation iteration
<i>TE</i>	Trailing Edge
<i>Tr</i>	Translated
<i>turn</i>	Sustained turn

$U_p$

Upper surface

# Acronyms

**ACC** Air Cargo Challenge.

**BPP** Bezier-PARSEC 3333 Parametrization.

**BSP** B-Spline Parametrization.

**CFD** Computational Fluid Dynamics.

**CSF** Class Shape Functions.

**MSE** Mean Squared Error.

**NACA** National Advisory Committee for Aeronautics.

**NURBS** Non Uniform Rational Basis Splines.

**PARSEC** Parametrized Sections method.

**PSO** Particle Swarm Optimization.

**RBF** Radial Basis Functions.

**RMSE** Root Mean Square Error.

**SVD** Singular Value Decomposition.

**UAV** Unnamed Aerial Vehicle.

**UIUC** University of Illinois Urbana-Champaign.





# Chapter 1

## Introduction

Considering that aerofoil design is a key part of the design phase of fixed and rotary wings, tools that facilitate this process are of interest, in particular for low speed and low Reynolds aerofoil design, which concerns unmanned aerial vehicle design and wind turbine design. Aerofoil optimisation automates this, leading to lower costs of development.

As stated by recent research [1], UAVs have had significantly development and its popularity has increased worldwide over the last decades. UAVs applications range from military use, such as reconnaissance, surveillance and security reinforcement, to civilian use, in traffic surveillance, disaster management, infrastructure inspection, law enforcement, and vegetation monitoring. The global UAV market is projected to grow by USD 20.58 billion until 2024, at a compound annual growth rate of nearly 16% over the forecast period, [2]. A fraction of this market corresponds to small fixed wing UAVs, which can use a low speed aerofoil design tool during their preliminary design phase.

According to Tummala et al. [3], renewable energy demand has been increasing due to the depletion of conventional energy sources and an increase in carbon dioxide emissions. Since wind energy is renewable and easily available, it has become an alternate source of energy. However, large scale wind farms have adverse effects on the climatic conditions on its location, [4–6]. Therefore, a possible solution is to employ decentralized small wing turbines, which would mitigate the climatic effects. Low speed aerofoil design tools are of interest to the preliminary design phase of these turbines.

### 1.1 Objective

The aim of this work is to develop a tool capable of aerofoil optimisation at low speeds that can be of use in the design phase of UAVs by adapting an existing one. Therefore, the tool must be able to analyse the aerofoil aerodynamics, generate and evaluate aerofoils and verify whether the aerofoil follows its geometric constrains and aerodynamic constrains. Since this tool involves several research areas, such as aerodynamics, parametrization and optimisation, not all the areas will share the same focus in this work. This work focuses primarily on different aerofoils parametrizations while using the same aerodynamic and optimisation models.

In order to adapt the existing tool, it is necessary to understand and verify the implementation of the aerodynamic model, the parametrization methods and the optimisation algo-

rithms. To this effect the existing tool is presented along with its changes for the development of the new tool.

To show case the tool capabilities two real life conditions will be optimized for the same UAV, albeit under different design conditions. The first one is the air cargo challenge of 2019, in witch different aerofoil parametrizations are compared. The second is the more recent edition of the same event, air cargo challenge 2021 (currently, postponed to 2022), where the original aerofoil is optimized a single time focusing in the analysis of the optimisation scheme.

## **1.2 Thesis Outline**

The present dissertation is organized into five distinct chapters. The current chapter, Chapter 1, provides the general scope of this dissertation, its motivation, and objectives behind the research. Chapter 2 addresses aerofoil design by detailing the work performed in this area during the last years and presenting a theoretical review. Chapter 3 presents the computational tool that was adapted for this dissertation and the methods used in its modification. Chapter 4 describes the study cases and results. Chapter 5 summarizes the most important conclusions of this research and presents future work suggestions.

# Chapter 2

## Bibliographic Review

This chapter presents the bibliographic review of the main areas concerning aerofoil optimisation. Section 2.1 introduces aerofoil optimisation in general. Section 2.2 presents the different aerofoil parametrization methods in use. Section 2.3 discusses the optimisation algorithms types in use. Section 2.4 presents the current tools for aerofoil optimisation.

### 2.1 Introduction to aerofoil optimisation

Aerofoil optimisation is a way of aerofoil design. Aerofoil design consists of choosing an aerofoil shape with appropriate performance to a particular application.

An aerofoil is a section geometry to be used in lifting plane surfaces. According to the book by Brederote [7], the main aerofoil characteristics, summarized by Figure 2.1, are the following:

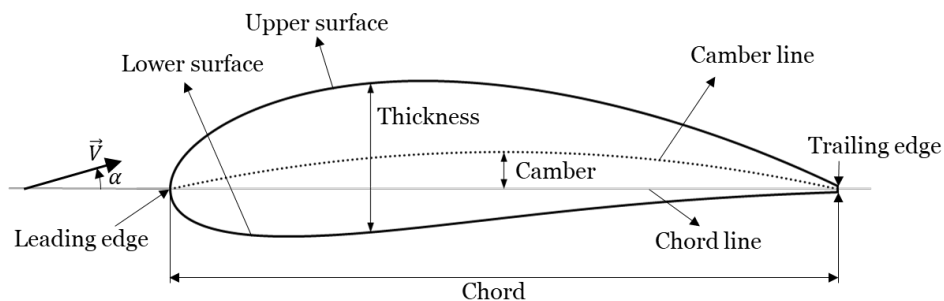


Figure 2.1: Aerofoil characteristics.

- Leading edge denotes the anterior extremity which first comes in contact with the incoming flow;
- Trailing edge refers to posterior surface where the flow leaves the aerofoil;
- Upper surface is the top curve between the leading edge and trailing edge;
- Lower surface is the bottom curve between the leading edge and trailing edge;
- Camber line is the medium line between the upper and lower surfaces;
- Aerofoil thickness denotes the maximum distance between the upper and lower surfaces;
- Aerofoil camber denotes the maximum distance between the chord line and the camber line;
- Chord denotes the distance between the leading edge and trailing edge, while the chord

line is the line between those points;

- Angle of attack  $\alpha$  refers to the angle between the uniform incoming flow velocity  $\vec{V}$  and the chord line.

In addition to these, the thickness distribution is also often used. The thickness distribution represents the thickness value along the chord.

To measure and compare aerodynamic performance of aerofoils, the scientific community resorted to several dimensionless numbers: lift coefficient  $C_l$ , drag coefficient  $C_d$ , pitching moment coefficient  $C_m$ , Reynolds number  $Re$  and Mach number  $M$ .  $C_l$ ,  $C_d$  and  $C_m$  normalise the lift force  $l$ , drag force  $d$  and moment  $m$  on the aerofoil by the freestream dynamic pressure  $q$  and chord  $c$ , Equations 2.1a, 2.1b, 2.1c.  $q$  is determined via Equation 2.1d, where  $\rho$  is the fluid density and  $V$  is the freestream velocity.

$$C_l = \frac{l}{qc} \quad (2.1a)$$

$$C_d = \frac{d}{qc} \quad (2.1b)$$

$$C_m = \frac{m}{qc^2} \quad (2.1c)$$

$$q = \frac{\rho V^2}{2} \quad (2.1d)$$

The Reynolds number relates the inertial forces to the viscous forces. This number is given by Equation 2.2 in which  $\mu$  is the fluid dynamic viscosity. Low values of Reynolds indicate that the flow is laminar, while high values are linked to turbulent flows.

$$Re = \frac{\rho V c}{\mu} \quad (2.2)$$

The Mach number is the ratio of the freestream velocity  $V$  by the speed of sound  $a$ , Equation 2.3. This number is related to compressibility effects which should be considered starting at 0.4 of the speed of sound.

$$M = \frac{V}{a} \quad (2.3)$$

A set of aerofoil geometry, angle of attack, Reynolds number and Mach number constitute a single analysis point. Alternatively, the lift coefficient can be used instead of the angle of

attack.

According to Selig [8], there are three different approaches to aerofoil design: the direct method in which the geometry is directly modified; the inverse method where the velocity distribution or the aerofoil boundary layer is controlled leading to the aerofoil geometry; and the performance method in which the aerodynamic performance is specified and its geometry obtained using an optimisation scheme. Aerofoil optimisation includes any aerofoil design method which utilises an optimisation scheme, therefore the performance method is a type of aerofoil optimisation.

Historically the direct design methods were the first to be employed, the aerofoil shape would be modified, a wing section built and wind tunnel tests would be performed to measure the aerofoil aerodynamic characteristics, that is lift coefficient, drag coefficient and moment coefficient, for a specified Reynolds number and Mach number. Until advances in computer technology this was the only means to aerofoil shape design.

By the 1970s rapid adoption of computers led to development of inverse methods and computational analysis via panel methods. In the inverse method, modification of the velocity distribution or pressure distribution lead to new aerofoil shapes.

Further developments in computer processors reduced the time required for machine analysis of aerofoil performance allowing for aerofoil optimisation in a timely manner. This phenomenon has led to continuous research on aerofoil optimisation.

Aerofoil shape optimisation consists of:

1. Problem formulation, i.e. selection of initial aerofoil shape, aerodynamic conditions, constrains and objectives;
2. Parametrization of initial aerofoil geometry to design variables;
3. Analysis of initial aerofoil and calculation of initial performance;
4. Application of the optimisation algorithm, which must be capable of:
  - (a) Generation of new values for the aerofoil design variables;
  - (b) Computation of new aerofoil geometries from the design variables values;
  - (c) Analysis of the new aerofoils and evaluation of the design variables values' merit;
  - (d) Checking the stop conditions. If those are not met, return to 4a;
5. Storing of the final aerofoil or aerofoils.

Problem formulation is one of the most important aspects in optimisation. Skinner et al. [9] presents the basic problem formulation for single objective optimisation mathematically as:

Minimize  $F(X)$  objective function with respect to  $X$  design variables,

$$\text{subject to } \begin{cases} g_i(\mathbf{X}) \leq 0 & i = 1, N_{IN} \text{ Inequality constraints} \\ h_j(\mathbf{X}) = 0 & j = 1, N_{EQ} \text{ Equality constraints} \\ X_k^l \leq X_k \leq X_k^u & k = 1, N_{DV} \text{ Parametrized constraints} \end{cases}$$

where  $\mathbf{X} = \{X_1 \ X_2 \ \dots \ X_{N_{DV}}\}^T$

This formulation requires that an objective function be defined based on the aerodynamic performance of the aerofoil. It leads to the determination of the aerodynamic conditions and constraints based on the overall objective and operation.

An initial set of design variables is equivalent to an initial aerofoil geometry due to the parametrization of the geometry.

## 2.2 Aerofoil parametrization

Aerofoil shape optimisation requires the shape to be parametrized so that a single vector defines the entire shape.

The use of a parametrization method leads to an aerofoil shape design space, that is the set of all possible aerofoil shapes possible with the model. Consider a model where the design variables are the aerofoil surface coordinates, this model has the largest possible design space since it is possible to have complete control over the surfaces. On the other end, in a model where the surfaces are represented by sixth degree polynomials, the shape can not represent a higher order polynomial or a non-polynomial curve.

According to Masters et al [10] a broad scope of methods have been used for aerofoil shape parametrization. These can be divided in two categories; constructive and deformative methods. For constructive methods the aerofoil shape is completely defined by the design variables, while deformative methods require an aerofoil shape and its design variables define the deformation on that shape.

Constructive methods include polynomials [11], splines [12, 13] and class–shape transformations [14, 15]. Deformative methods include discrete [16], analytical [17] and free-form deformation based [18, 19] methods. It is important to note that the methods previously referred do not represent the totality of parametrization schemes.

For polynomial representation of aerofoil shape a set of two polynomials define either the upper and lower surfaces or the camber and thickness lines. Several polynomials have been used for aerofoil shape optimisation such as the Daniel Nelson polynomial [11] and Chebyshev polynomials [20].

Spline based methods are widely applied in commercial CAD software mainly due to its local modifiability and flexible properties [21, 22]. There exist several spline based methods

for instance bezier curves, basis splines (B-splines) and non uniform rational basis splines (NURBS). These methods are related to each other, as each is a generalization of the previous one.

Bezier curves use a linear combination of the Bernstein polynomials with its coefficients known as control points. While it provides a basis for shape representation, there are two main problems with this scheme. The first is that to create more complex shapes either the number of control increases leading to higher degree polynomials or multiple curves are required with continuity conditions. The second is that the control points position globally affect the curve.

B-spline method employs a linear combination of basis functions with its coefficients known as control points and its basis functions are determined by the knot vector. When the knot vector has no interior knots the B-spline is equivalent to the bezier curve. Additionally the use of knot vector addresses the problems with the bezier curve, meaning that it allows for local modifiability and it permits higher shape complexity by increasing the knot vector size without the need for a higher degree.

The NURBS scheme further increases the design space by introducing a weight to each B-spline basis function and using the ratio of the weighted B-splines by the weighted B-splines basis functions. When the weights are unitary the NURBS shape becomes a B-spline curve.

Aerofoil shape representation using aerofoil geometric properties as design variables usually use polynomials or splines. Sobieczky's [23] parametrized sections method (PARSEC) is one of these, where each aerofoil surface is approximated by a sixth order polynomial, leading to 12 design variables. In 2010, Derksen et al. [24] proposed two additional methods; Bezier-PARSEC 3333, where each surface is defined by two third degree Bezier curves, and Bezier-PARSEC 3434, in which each surface is determined by a third degree Bezier curve near the leading edge and a fourth degree Bezier near the trailing edge. Leading to 12 and 15 design variables, respectively. The main disadvantage of these schemes is a limited number of design variables, meaning that these have reduced flexibility.

Regarding Kulfan and Bussoletti's class shape functions [14, 15], it uses a linear combinations of Bernstein polynomials with an aerofoil class shape or even multiple classes [25]. This method allows for flexible control over its fidelity, however a higher number of design variables requires polynomials of higher degree, meaning that its local modifiability is reduced.

Aerofoil shapes can also be defined via a set of orthogonal modes from a collection of aerofoils, Chang et al. [26] analytically derived the modes for the 4-digits NACA series and supercritical shapes. Formal methods also exist, such as singular value decomposition (SVD) [10, 27], where orthogonal decomposition is applied to an initial set of aerofoils to obtain the main modes. These serve as the basis for new aerofoils. Toal et al. [27] used a set of 30

aerofoils shapes to numerically determine its basis functions and define a design space based on orthogonal decomposition. Masters et al. [10] applied singular value decomposition on the University of Illinois Urbana-Champaign aerofoil database library to get a general set of modes mapping the shapes.

The discrete method [16] uses the aerofoil points coordinates as the design variables. This allows for absolute control over the shape and no restrictions on the design space, however, this also presents several difficulties. A single design variable change leads to loss of curve smoothness affecting adversely the aerodynamic analysis or even preventing analysis. The extremely high number of design variables increases optimisation time and cost substantially. Due to these, other parametrization methods are generally preferred.

The Hicks and Henne's [17] bump functions analytical formulation employs a linear combination of sine bump functions to deform a base aerofoil on the upper and lower surfaces. The bump function allows for control over its position, width and height, meaning that the scheme is capable of local changes in the aerofoil.

Free-form deformation for shape parametrization is based on the creation of a deformation field over the aerofoil surfaces, the field control points are then manipulated to modify the shape [18]. Bèzier surfaces [28] is a scheme based on this concept, where a structured lattice of initial control points is used, leading to global modifications. Another method is radial basis functions (RBF) applied to an arbitrary domain element, where changes in the domain element (a series of control points) lead to changes on the aerofoil [29].

The use of a specific parametrization method for aerofoil shape optimisation entails setting the number of design variables and therefore the scheme accuracy and type of design space. For this reason several comparisons have been made [10, 30–33].

Sripawadkul et al. [30] compared five schemes, specifically, Ferguson's curves, Hicks Henne bump functions, B-Splines, PARSEC and class shape functions (CSF). These were analysed according to five different criteria particularly parsimony, completeness, orthogonality, flawlessness and intuitiveness resulting in Table 2.1. Parsimony compared the number of design variables required for representation of the RAE2822 aerofoil within tolerances. Completeness measured the number of aerofoil shapes out of 250 possible that each method could make good approximations. Orthogonality studied whether each method basis were orthogonal. Flawlessness refers to the existence of additional bumps on the shape or compenetration. Intuitiveness indicates whether the design variables have any relation to aerofoil geometric properties. Its results show parametrization methods characteristics differ, meaning that for each specific application an appropriate method must be selected.

Rajnarayan et al. [31] showed that the B-spline design space encompasses the design space of class shape transformations by proving the equivalence of a order  $n$  CSF to a Bezier curve of order  $2n + 3$ . Additionally, the PARSEC method was shown to be exactly equivalent to a



Table 2.1: Parametrization methods comparison results by Sripawadkul et al. [30].

Methods	Parsimony	Completeness	Orthogonality	Flawlessness	Intuitiveness
Ferguson’s Curve	4.0	2.4	0.0	4.0	2.0
Hicks-Henne	1.0	4.0	0.0	4.0	3.0
B-Splines	3.5	3.9	0.0	4.0	3.0
PARSEC	2.9	3.8	4.0	2.9	4.0
CSF	2.9	3.7	4.0	4.0	4.0

Bezier curve of order 11. In both cases the number of design variables increases substantially, for CSF from  $n$  to  $2(2n + 3)$  and for PARSEC from 12 to 22, leading to a higher optimisation time and computational cost if B-splines equivalence is used.

Masters et al. [10, 32] compared seven parametrization methods namely CSF, B-splines, Hicks-Henne bump functions, PARSEC, RBF, Bezier surfaces and SVD, along aerofoil shape accuracy and aerofoil aerodynamic accuracy. The geometric error tolerance was calculated for each aerofoil in the University of Illinois Urbana-Champaign aerofoil database library and NACA 4-series aerofoil library with each parametrization method for a range of 0 to 100 design variables when possible. It was found that 20 to 25 design variables were required to represent the entire database of aerofoils within Kulfan tolerance, shown in Figure 2.2. Regarding the aerodynamic accuracy comparison, this was studied in a set of five aerofoils for lift coefficient and drag coefficient convergence. Results showed that convergence of the geometric shape correlates with the convergence of the aerodynamic properties. The Kulfan tolerance had a lift coefficient variance of  $10^{-2}$  and a drag coefficient variance of  $10^{-3}$  leading to a proposal of a stricter geometric tolerance. Under this tolerance, 38 to 66 design variables were required to represent 80% of the aerofoil database.

Other studies also compare the geometric error of parametrization methods on a set of aerofoils [33, 34]. Zhang et al. [33] utilised five parametrization methods and studied its fitting on the NASA SC(2)-0414 aerofoil using only six design variables, the residual on the top surface is shown in Figure 2.3. Vicente et al. [34] compared the mean squared error and a merit Figure (inverse of the product of the mean squared error by the number of design variables) for four parametrization methods on four aerofoils, results presented in Table 2.2.

From Figure 2.2 it is possible to observe that only flexible methods allow for large scale shape representation within acceptable accuracy. The SVD built from the UIUC library has the highest design space by number of design variables followed by CSF, B-Spline and Hicks-Henne. This order does not hold for individual aerofoils as shown in Figure 2.3, with the PARSEC scheme having better accuracy than CSF and Hicks-Henne. Vicente et al. [34] shows that CSF and B-Spline have similar accuracy, however the B-Spline method employed is different from the one used in Masters et al. [32]. Vicente et al. [34] utilises the control points in the chord wise direction as design variables instead of following a cosine distribution.

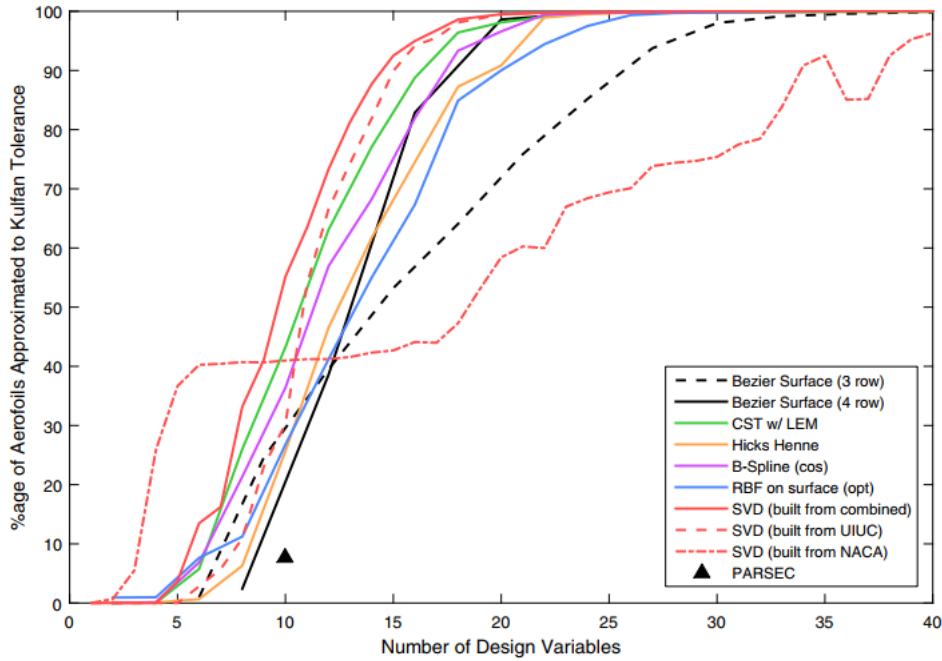


Figure 2.2: Percentage of aerofoils database within Kulfan tolerance for different parametrization methods by Masters et al. [32].

### 2.3 Optimisation algorithms

As stated in Section 2.1, aerofoil optimisation involves using a formal optimisation algorithm to maximize the aerofoil performance. In the work of Skinner et al. [9], optimisation is introduced as the method of obtaining the most suitable solution to a given problem.

optimisation algorithms can be classified as single or multi objective and gradient based or gradient free. Gradient based algorithms calculate the gradient of the objective function, utilise it to generate new design variables and eventually find a minimum. In the work of Skinner et al. [9], it is mentioned that while gradient based methods are very suitable to find local solutions it may struggle to find the global solution. However, they exhibit lower

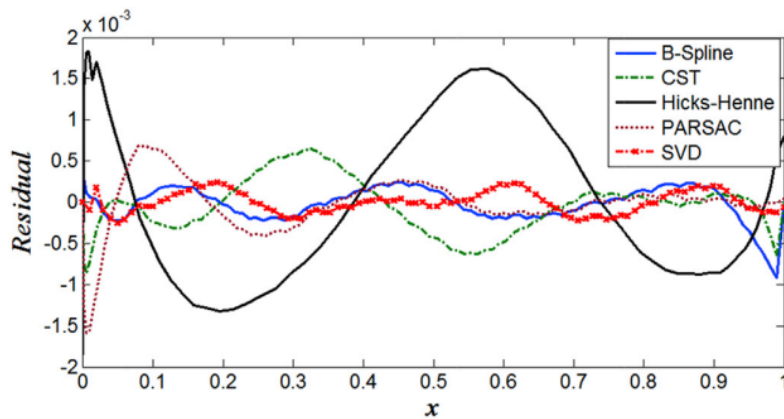


Figure 2.3: Residuals for different parametrization methods with six design variables for the top surface of the NASA SC(2)-0414 aerofoil by Zhang et al. [33].

Table 2.2: Mean squared error (MSE), number of design variables ( $N_{DV}$ ) and merit for each method and aerofoil by Vicente et al. [34].

Method	NACA 0012 (121 points)			Eppler 71 (62 points)		
	MSE	$N_{DV}$	Merit	MSE	$N_{DV}$	Merit
B-spline	1.61E-07	23	2.69E+05	8.23E-07	23	5.28E+04
DNP	2.36E-06	6	7.07E+04	6.59E-05	6	2.53E+03
CSF	8.75E-09	9	1.27E+07	2.93E-08	17	2.01E+06
BPP 3333	1.80E-07	12	4.63E+05	9.96E-08	12	8.37E+05
Method	Selig 1223 (140 points)			Selig 5020 (62 points)		
	MSE	$N_{DV}$	Merit	MSE	$N_{DV}$	Merit
B-spline	1.96E-07	23	2.22E+05	6.92E-08	23	6.29E+05
DNP	8.13E-05	6	2.05E+03	1.71E-05	6	9.72E+03
CSF	1.88E-07	27	1.97E+05	3.48E-08	19	1.37E+06
BPP 3333	2.26E-06	12	3.68E+04	1.42E-06	12	5.87E+04

computational demands for high numbers of design variables.

As the name indicates multi objective allows for more than an objective to be optimised by finding the non-dominated solutions along the Pareto front. In Montano et al. [35], this concept is presented and several multi objective algorithms used in aerofoil optimisation are discussed, with most leading to improved designs.

While the optimisation algorithm is of great importance for aerofoil optimisation, it is in the best interest of this dissertation that a single algorithm be used, since case study 1 focuses on the parametrization method and case study 2 focuses on the tool itself.

In case study 1, different parametrization methods have different scales and initial variables. Since a penalty function is utilised many combinations of variables may not be viable, making find a viable solution very improbable. The optimisation algorithm must be capable of converging to the initial design variables during optimisation to find a viable solutions near the initial variables, if no viable solutions have been found. Particle swarm optimisation fulfils these conditions.

Particle swarm optimisation (PSO) is a gradient free algorithm based on the swarm animal behaviour, found in fishes and birds. Each particle (element of the population) is assigned a position (design variables) and a velocity, each particle keeps track of its best position and the particles share what is the best position overall. Each optimisation step (time), the positions and velocities will update with each particle velocity gravitating towards their own best and overall best.

According to Skinner et al. [9] this algorithm was developed by Kennedy and Eberhart [36,37] in the 1990s. Some potential problems are how to enforce constraints and variable bounds and the selection of parameters or the way in which they vary.

While there are many other algorithms, no other will be presented in this work because they simply are not utilised.

## 2.4 Existing tools

In order to design aerofoils, several tools have been developed. However many of these are in house research codes, which are not publicly available or are not listed in an organized namer. In this section some public tools are presented. It is important to keep in mind that there exist several CFD tools that allow aerofoil optimisation either by its means or adicional software, such as ANSYS FLUENT and OpenFOAM.

For direct and inverse aerofoil design, the XFOIL tool is one with significant use and research apparatus, [38–41]. The XFOIL tool is capable of aerodynamic analysis by coupling a potential flow panel method solution with an integral boundary layer leading to rapid calculating speed with acceptable precision, for this reason it is also used as the aerodynamic solver for several aerofoil optimisation tools.

Regarding aerofoil optimisation tools without need of modification or implementation there are XOPTFOIL [42] , Python XFOIL optimization toolbox [43] and Bézier-GAN [44, 45]. These three all use XFOIL as the aerodynamic solver. XOPTFOIL uses Hicks-Henne or NACA modal functions for aerofoil parametrization and either a genetic algorithm, particle swarm optimisation or simplex for optimisation. It is of note that this tool is implemented in Fortran and the XFOIL code is embedded. Python XFOIL optimisation toolbox can use NACA 4 series or PARSEC for parametrization and particle swarm optimisation. Bézier-GAN uses generative adversarial networks and Bézier parametrization to model the design space of the UIUC database [45, 46]. This leads to a reduction of the design space but increases optimisation speed using either efficient global optimisation or a genetic algorithm.

Considering the objectives of this dissertation, it is necessary to decide whether an original tool will be developed or one of these existing tools will be adapted. Given that modification of an existing tool has a lower workload, it was chosen to adapt the XOPTFOIL software. While any of the presented codes could have been adapted, the author already had experience with the Fortran language and considered that the XFOIL being embedded was a valued asset.

# Chapter 3

## Methods

The following chapter presents the formulation of the relevant methods for this work and its implementation within XOPTFOIL. Section 3.1 introduces the tool algorithm. Section 3.2 presents the initial transformations to the aerofoil shape and discusses its limitations. Section 3.3 establishes the formulation for the parametrization methods. Section 3.4 introduces the aerofoil evaluation method. Section 3.5 presents the formulation for the optimisation algorithm in use.

### 3.1 XOPTFOIL

This tool [42] minimizes an objective function given by a set of operating points under specified constraints. The implementation of this tool is shown in Figure 3.1 and can be summarized as:

1. Read the input file, containing the initial aerofoil coordinates file location, operating points, constraints, XFOIL options, parametrization options, optimisation options and data options;
2. From the initial aerofoil coordinates, transform the aerofoil so that it has a unit chord length and zero angle of attack. Given a specified parametrization type, determine the design variables;
3. Employing the design variables, check the initial aerofoil constraint values and using XFOIL analyse the aerofoil at the operating points. Save the constraint values and aerodynamic values from the operating points as reference values;
4. Compute the initial design variables' upper and lower limits based on the reference values and initial perturbations;
  - (a) Apply the particle swarm algorithm: calculate the population positions and speeds;
5. If population has converged or if iteration number limit has been reached stop the tool, else continue to 6;
6. Compute the new aerofoil coordinates for the population according to the used parametrization;
7. Check the new aerofoil constraints and analyse its operating points using XFOIL. Calculate the objective function value from the constraints and aerodynamic analysis relative to the reference values. Return to step 4a.

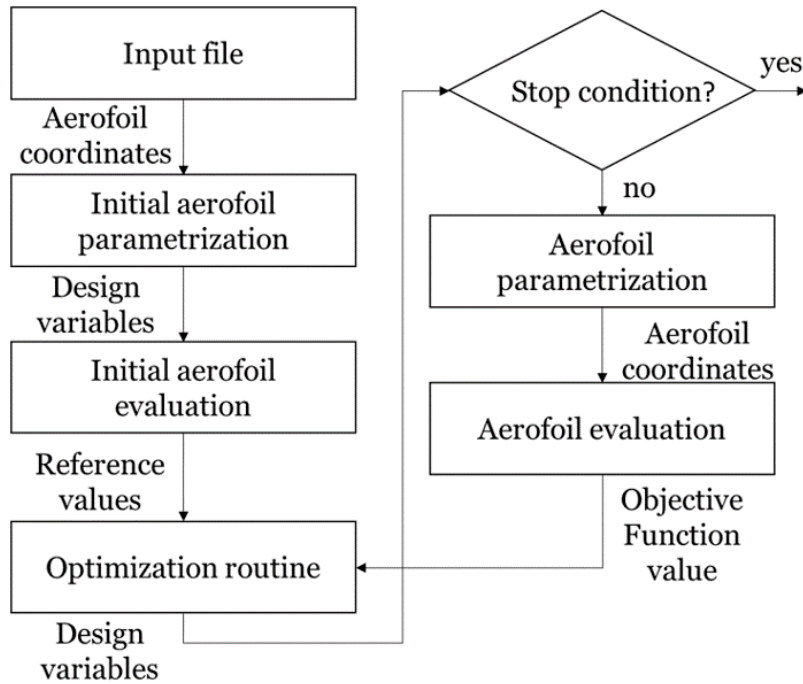


Figure 3.1: Modified XOPTFOIL tool flowchart.

The input file required by the tool contains all relevant information for the aerofoil optimisation:

- Initial aerofoil coordinates file location: it provides the tool with initial aerofoil coordinates which are used to obtain the initial set of design variables and serves as the reference for the optimisation. The coordinates must start and end at trailing edge and be ordered from the upper trailing edge towards the leading edge sequentially and then to the lower trailing edge;
- Operating conditions: whether to use a simple flap, the flap hinge coordinates, whether to optimise the flap hinge location along the chord, whether to keep the trailing edge thickness, set it or optimise it, its value, the number of operating points and each operating point specific conditions:
  - Aerodynamic conditions: whether it uses the angle of attack or lift coefficient as a constant, its value (or start, step and end for a sequence), Reynolds number, Mach number and Ncrit. Ncrit is the transition criterion parameter required by XFOIL;
  - optimisation conditions: a weight, an optimisation type/objective, whether to optimise its flap angle deflection, its value, whether to set flap angle deflection the same as other operating point and whether to use the XFOIL result from other operating point;
- Constraints: the set of geometrical and aerodynamic constraints on the aerofoil;
- XFOIL options: options regarding the analysis using XFOIL such as number of points, panelling, Ncrit for the model, number of iterations, whether the boundary layer is reinitialized and approach regarding non converged cases;

- Parametrization options: options regarding the parametrization such as the parametrization scheme, scheme parameters and number of design variables per surface;
- optimisation options: options regarding the optimisation routine such as the algorithm, algorithm parameters, maximum number of iterations, minimum design radius, initial perturbations and initialization type;
- Data options: these determine which data to store during the optimisation such as design coordinates, design variables, constraints values, objective function value and operating points objective values.

Notice that for each operating point, all the aerodynamic conditions must be specified therefore only type 1 analysis is used in XOPTFOIL. Type 1 analysis is a XFOIL analysis type, where the Reynolds number and Mach number are held constant, thus chord and velocity are fixed, and lift may vary depending on the angle of attack.

The modified version of this tool, used in this work, is available in accordance with reference [47].

### 3.2 Initial transformations

After reading the input file, the tool executes the initial parametrization routine. As stated in Section 3.1 this routine will determine the aerofoil design variables for the specified parametrization type, according to Figure 3.2.

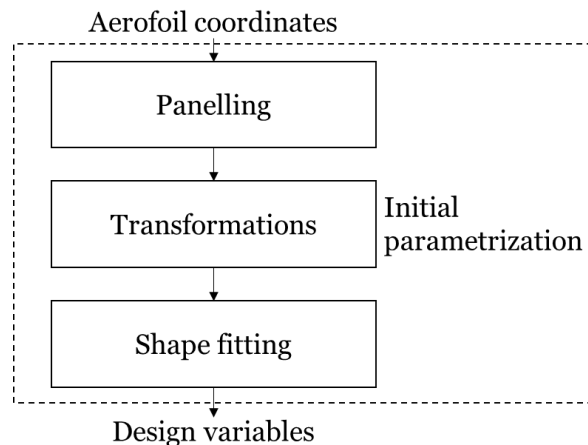


Figure 3.2: Initial parametrization routine flowchart.

This routine first re-panels the aerofoil using the XFOIL PANGEN code, where the aerofoil coordinates are interpolated using a cubic spline and new coordinates are determined, according with the XFOIL paneling options. In fact, paneling is handled by the PANGEN code in all cases.

Then, several transformations are applied to the aerofoil, so that it is in accordance with Figure 3.3. Specifically, the leading edge position coincides with the origin, the trailing edge

mid point lies on the  $x$ -axis and the aerofoil has a unit chord.

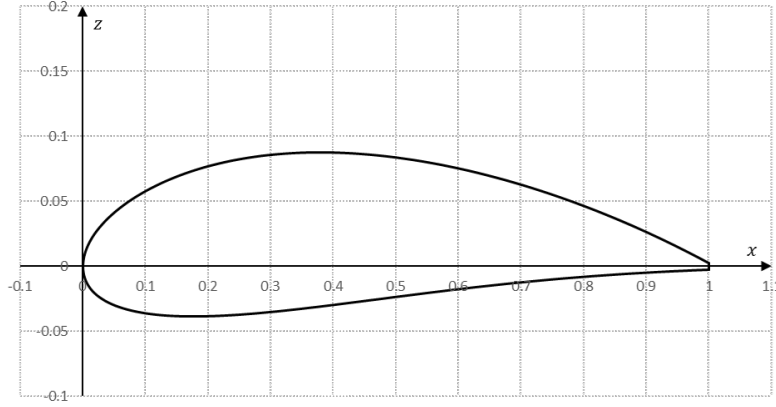


Figure 3.3: Aerofoil after transformations.

Given a set of coordinates which start and end at the trailing edge with  $N_p$  points, it is possible to immediately determine the trailing edge midpoint coordinates  $(\tilde{x}_{TE}, \tilde{z}_{TE})$  by Equation 3.1, which depends on the aerofoil  $\tilde{x}$  coordinates vector  $\tilde{\mathbf{x}}$  and  $\tilde{z}$  coordinates vector  $\tilde{\mathbf{z}}$ .

$$(\tilde{x}_{TE}, \tilde{z}_{TE}) = \left( \frac{\tilde{x}_1 + \tilde{x}_{N_p}}{2}, \frac{\tilde{z}_1 + \tilde{z}_{N_p}}{2} \right) \quad (3.1)$$

The leading edge coordinates are less obvious to determine, considering that the leading edge is the furthest point from the trailing edge and using the cubic spline interpolation of the aerofoil  $(\tilde{x}(s), \tilde{z}(s))$ , it is possible to calculate its position  $(\tilde{x}_{LE}(s_{LE}), \tilde{z}_{LE}(s_{LE}))$  with Equation 3.2. The furthest point from the trailing edge is the one where the tangent to the aerofoil surface is normal to the line from such point to the trailing edge. This Equation is numerically solved by using the Newton-Raphson method.

$$(\tilde{x}_{LE} - \tilde{x}_{TE}, \tilde{z}_{LE} - \tilde{z}_{TE}) \cdot \left( \frac{\partial \tilde{x}}{\partial s}(s_{LE}), \frac{\partial \tilde{z}}{\partial s}(s_{LE}) \right) = 0 \quad (3.2)$$

With both the reference points coordinates, the aerofoil is translated in agreement with Equation 3.3, then the original angle of attack is calculated, Equation 3.4, and the aerofoil is rotated by that angle, Equation 3.5. Finally the aerofoil is scaled, Equation 3.6, obtaining the transformed aerofoil coordinates  $(x, z)$ , which are non-dimensional.

$$(\tilde{x}_{Tr,i}, \tilde{z}_{Tr,i}) = (\tilde{x}_i - \tilde{x}_{LE}, \tilde{z}_i - \tilde{z}_{LE}), \forall i \in [1, N_p] \quad (3.3)$$



$$\alpha_0 = \text{atan} \left( \frac{\tilde{z}_{LE} - \tilde{z}_{TE}}{\tilde{x}_{LE} - \tilde{x}_{TE}} \right) \quad (3.4)$$

$$(\tilde{x}_{Rot,i}, \tilde{z}_{Rot,i}) = \begin{pmatrix} \cos(\alpha_0) & \sin(\alpha_0) \\ -\sin(\alpha_0) & \cos(\alpha_0) \end{pmatrix} \cdot \begin{pmatrix} \tilde{x}_{Tr,i} \\ \tilde{z}_{Tr,i} \end{pmatrix}, \forall i \in [1, N_p] \quad (3.5)$$

$$(x_i, z_i) = \left( \frac{\tilde{x}_{Rot,i}}{|\tilde{x}_{LE} - \tilde{x}_{TE}, \tilde{z}_{LE} - \tilde{z}_{TE}|}, \frac{\tilde{z}_{Rot,i}}{|\tilde{x}_{LE} - \tilde{x}_{TE}, \tilde{z}_{LE} - \tilde{z}_{TE}|} \right), \forall i \in [1, N_p] \quad (3.6)$$

Depending on whether the trailing edge thickness is to be set to an input value, an optional transformation to  $z$  is done, Equation 3.7a for the upper surface and 3.7b for the lower.

$$z_{Up,i} = z_{Up,i} + \frac{(x_{Up,i} - x_{ref,TE}) \cdot (th_{TE,spec} - th_{TE,o})}{2}, \forall i \in [1, N_{ps,Up}] \quad (3.7a)$$

$$z_{Lo,i} = z_{Lo,i} - \frac{(x_{Lo,i} - x_{ref,TE}) \cdot (th_{TE,spec} - th_{TE,o})}{2}, \forall i \in [1, N_{ps,Lo}] \quad (3.7b)$$

Shape fitting of the transformed aerofoil is addressed in the following Section 3.3.

### 3.3 Parametrization methods

The parametrization methods are of relevance to two different steps in XOPTFOIL, shape fitting in initial aerofoil parametrization and aerofoil geometry creation in aerofoil parametrization. In this Section the mathematical formulation for all the methods that already existed in XOPTFOIL, Hicks-Henne functions and orthogonal NACA functions, and the added methods B-spline, class shape functions and Bezier-PARSEC 3333 are presented.

Shape fitting refers to the determination of the design variables based on the aerofoil coordinates, while aerofoil geometry creation refers to the opposite process. Following the shape fitting, a new aerofoil is created based solely on the design variables named parametrized initial aerofoil. The accuracy of the parametrized initial aerofoil is measured against the transformed aerofoil using Equation 3.8.

$$RMSE_s = \sqrt{\frac{\sum_{i=1}^{N_{ps}} (z_{para,s,i} - z_{s,i})^2}{N_{ps}}} \quad (3.8)$$

### 3.3.1 Hicks-Henne functions

Hicks-Henne functions was an already exiting method in XOPTFOIL. The method proposed by Hicks and Henne [17], known as Hicks-Henne (HH) functions, consists in using a linear combination of augmented sine functions to perturb an initial geometry. Each aerofoil surface is defined by Equation 3.9.

$$z_i = z_{base,i} + \sum_{j=1}^{N_{functions}} a_j \sin^{h_{1,j}} \left( \pi x_{base,i}^{\frac{\log 0.5}{\log h_{2,j}}} \right), \forall i \in [1, N_{ps}] \quad (3.9)$$

Each function is defined by three variables, the coefficient  $a$ , the parameter controlling the width  $h_1$  and the parameter  $h_2$  which determines the location of the function maximum value. These parameters can be used as design variables or be fixed. The original implementation in XOPTFOIL had these as design variables. This work keeps them as design variables, given the results from Masters et al. [10], where  $h_1$  was varied from 0.1 to 2.0,  $h_2$  was fixed and the percentage of aerofoils possible to represent was determined, where the design space was significantly influenced by  $h_1$ .

Regarding implementation, this method uses the transformed aerofoil as the base. Given Equation 3.9, the initial design variables have coefficients with value of 0.0, however  $h_1$  and  $h_2$  can not have a zero value, their value is set to 1.0 and 0.5 respectively. These parameters are constrained  $h_1 \in [h_{1,min}, 10]$  and  $h_2 \in ]0, 1[$ , with  $h_{1,min}$  being the minimum value given by the user and 10 being a fixed limit.

### 3.3.2 Orthogonal NACA functions

The orthogonal NACA functions method was an already exiting method in XOPTFOIL. This is a hybrid method which uses an expansion of the orthogonal modes for the 4-digits NACA series and supercritical shapes derived by Chang et al. [26] for the deformation shape on top of a base aerofoil. Each aerofoil surface is given by Equation 3.10 with the expanded modes  $f_{naca,j}(x)$  given by Equation 3.11, these are then normalised by the maximum value of its mode.

$$z_i = z_{base,i} + \sum_{j=1}^{N_{functions}} a_j \bar{f}_{naca,j}(x_{base,i}), \forall i \in [1, N_{ps}] \quad (3.10)$$

$$f_{naca,j}(x_i) = \begin{cases} x_{base,i}^{\frac{1}{(j+1)/2+1}} - x_{base,i}^{\frac{1}{(j+1)/2}} & \text{if } j \text{ is odd} \\ x_{base,i}^{j/2} (1 - x_{base,i}) & \text{if } j \text{ is even} \end{cases} \quad (3.11)$$

Regarding implementation, this method uses the transformed aerofoil as the base, with the only design variables being the coefficients  $a_j$ . Given that it is a deformation method the initial coefficients have a value of 0.0. There are no constraints on these variables.

### 3.3.3 B-Splines

A B-spline curve is defined as a linear combination of basis functions  $N_{i,k}(t)$  and its coefficients known as control points  $P_i$ , Equation 3.12, with  $P_i \in \mathbb{R}^m$  and  $C(t) \in \mathbb{R}^m$ ,  $m$  being 2 for a planar curve.

$$C(t) = \sum_{i=0}^{N_{cp}-1} N_{i,k}(t) P_i, \quad N_{cp} \geq k, \quad t \in [T_{k-1}, T_{N_{cp}}] \quad (3.12)$$

where  $k$  is the order of the basis function. There are  $N_{cp}$  functions and control points and  $T_{k-1}$  and  $T_{N_{cp}}$  are elements of the knot vector  $T$  given by Equation 3.13. Notice that it starts and ends with  $k$  equal knots so that the first and last control point coordinates coincide with the start point and end point of the spline, respectively. In this work a uniform distribution is used for the knot vector.

$$T = \underbrace{[T_0, T_1, \dots, T_{k-1}]}_{k \text{ equal knots}}, \underbrace{[T_k, T_{k+1}, \dots, T_{N_{cp}-2}, T_{N_{cp}-1}]}_{N_{cp} - k \text{ internal knots}}, \underbrace{[T_{N_{cp}}, \dots, T_{N_{cp}+k-1}]}_{k \text{ equal knots}} \quad (3.13)$$

The basis functions are defined by a recurrence relation, Equation 3.14, with  $k = 1$  as the initial condition, Equation 3.15.

$$N_{i,k}(t) = \frac{t - T_i}{T_{i+k-1} - T_i} N_{i,k-1}(t) + \frac{T_{i+k} - t}{T_{i+k} - T_{i+1}} N_{i+1,k-1}(t), \quad k > 1, \quad i = 0, 1, 2, \dots, N_{cp} - 1 \quad (3.14)$$

$$N_{i,1}(t) = \begin{cases} 1 & \text{for } T_i \leq t < T_{i+1} \\ 0 & \text{otherwise} \end{cases} \quad (3.15)$$

While there is a variety of ways to represent an aerofoil using B-splines, in order to satisfy the constraints imposed in Section 3.2, two B-splines were chosen, one for the upper surface and another for the lower surface. This results in the following restrictions to the control points,

$P_0$  is coincident with the leading edge,  $P_{N_{cp}-1}$  is at the trailing edge mid point and  $P_1$  is on the  $z$  axis, these apply to both surfaces. Two variations have been considered, fixed and free  $x$  coordinates for the control points.

In the fixed variation, a cosine distribution is used for the  $x$  coordinates, Equation 3.16. Masters et al. [10, 32] has shown that the order of the basis functions has a lesser impact on the design space with a cosine distribution when compared with a linear distribution for a cubic uniform spline. Since the only free coordinates are the  $z$  coordinates of the control points 1 to  $N_{cp} - 2$ , there are  $N_{cp} - 2$  design variables for each surface.

$$P_0 = (0, 0), \quad P_i = \left( \frac{1}{2} \left[ 1 - \cos \left( \frac{\pi(i-1)}{N_{cp}-2} \right) \right], a_i \right), \quad P_{N_{cp}-1} = (1, 0) \quad (3.16)$$

Regarding implementation, in order to determine the initial design variables, several steps are taken:

1. With the aerofoil  $x$  coordinates and control points,  $x$  and  $P_X$ , the corresponding  $t$  is determined,  $t$ ;
2. Given that the same  $x$  coordinates are used during the optimisation, the basis function values are calculated and stored in matrix  $M$  via Equation 3.17;
3. Solve the least squares approximation  $z = M \cdot P_Z$  using singular value decomposition, where  $z$  are the  $z$  coordinates of the aerofoil and  $P_Z$  the  $z$  control points of the spline.

$$M_{(i,j)} = N_{j-1,k}(t_i), \quad \forall i \in [1, N_{ps}] \quad \forall j \in [1, N_{cp}] \quad (3.17)$$

The B-spline method uses De Boor's algorithm [22] for determining the basis functions value, a uniform knot vector and has the basis function order as a parameter. There are no further constraints on the design variables. During optimisation the  $z$  coordinates of the aerofoil are calculated via Equation 3.18.

$$z = M \cdot P_Z \quad (3.18)$$

In the free variation, both coordinates are free for control points 2 to  $N_{cp} - 2$  plus the  $z$  for  $P_1$ , therefore it has  $2(N_{cp} - 3) + 1$  design variables for each surface. Regarding implementation, the initial design variables used are not the best fit for the aerofoil, instead the fixed solution is used. The method assumes that the  $x$  coordinates are not ordered and sorts them,

additionally the  $x$  control points are constrained between 0 and 1.

### 3.3.4 Class shape functions

In this method, class shape functions (CSF) developed by Kulfan and Bussoletti [14], shapes are defined as the product of a class function  $C(x)$  and a shape function  $S(x)$ . Two curves are necessary to represent an aerofoil shape and considering the geometric constraints imposed, the curves represent the upper and lower surfaces, Equations 3.19a and 3.19b. An additional term is added to account for the trailing edge thickness.

$$z_{Up}(x) = C_{N_2}^{N_1}(x) \cdot S_{Up}(x) + x \frac{\Delta z_{TE}}{2} \quad (3.19a)$$

$$z_{Lo}(x) = C_{N_2}^{N_1}(x) \cdot S_{Lo}(x) + x \frac{\Delta z_{TE}}{2} \quad (3.19b)$$

The class functions parameters  $N_1$  and  $N_2$  control which class is in use, Equation 3.20. For instance the aerofoil class has  $N_1 = 0.5$  and  $N_2 = 1$ .

$$C_{N_2}^{N_1}(x) = x^{N_1} \cdot (1 - x)^{N_2} \quad (3.20)$$

Kulfan [15] suggested using a linear combination of Bernstein polynomials to define the shape function. In later works, Kulfan [25] introduced an additional term, known as leading edge modification (LEM). Equation 3.21 presents the shape function definition, where  $D_S$  is the degree of the Bernstein polynomials. Masters et al. [32] has shown that the LEM leads to an increase in the design space.

$$S(x) = \sum_{i=0}^{D_S} a_i \cdot \binom{D_S}{i} x^i (1 - x)^{D_S - i} + \underbrace{a_{D_S+1} x^{0.5} (1 - x)^{D_S - 0.5}}_{\text{LEM}} \quad (3.21)$$

Regarding implementation, the least squares approximation is used to determine the coefficients  $a_i$  in vector  $A$  at Equation 3.22, where  $\hat{z}$  elements are determined with Equation 3.23 and  $M$  with 3.24. Singular value decomposition is used to solve the linear equation system. The design variables have no constraints during optimisation.

$$\hat{z} = M \cdot A \quad (3.22)$$

$$\hat{z} = z - \frac{\Delta z_{TE}}{2} x \quad (3.23)$$

$$M_{(i,j)} = x_i^{0.5} \cdot (1 - x_i) \cdot \begin{cases} \binom{D_S}{j} x_i^j (1 - x_i)^{D_S-1} & \text{if } j \in [0, D_S] \\ x_i^{0.5} (1 - x_i)^{D_S-0.5} & \text{if } j = D_S + 1 \end{cases} \quad \forall i \in [1, N_{ps}] \quad \forall j \in [1, D_S + 1] \quad (3.24)$$

### 3.3.5 Bezier-PARSEC 3333

Derksen et al. [24] proposed the Bezier-PARSEC 3333 (BPP) method in which an aerofoil is represented by four third degree Bezier curves and defines such curves by using twelve aerodynamic parameters: leading edge radius on thickness curve -  $r_{LE}$ ; maximum thickness position, value and curvature -  $(x_t, z_t, \kappa_t)$ ; trailing edge angle on thickness curve -  $\beta_{TE}$ ; trailing edge thickness -  $th_{TE}$ ; leading edge angle on camber curve -  $\gamma_{LE}$ ; maximum camber position, value and curvature -  $(x_c, z_c, \kappa_c)$ ; trailing edge angle on camber curve -  $\alpha_{TE}$ ; and trailing edge vertical displacement -  $z_{TE}$  according with Figure 3.4.

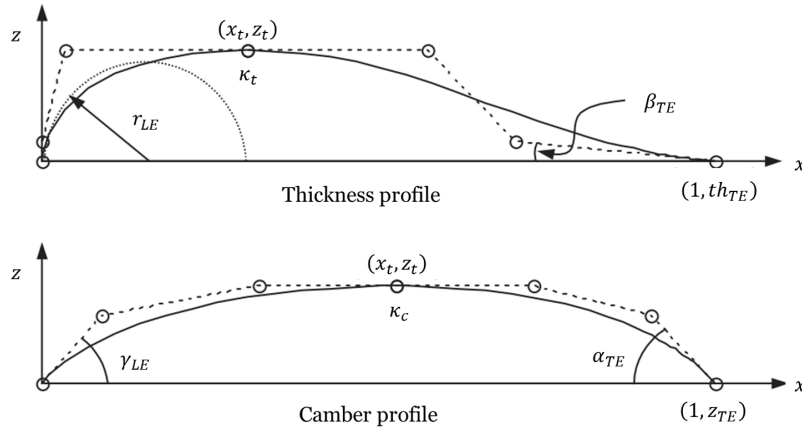


Figure 3.4: Bezier-PARSEC 3333 aerofoil geometry and Bezier control points defined by twelve basic aerodynamic parameters as set by Derksen et al. [24].

Each third degree Bézier curve is given by Equations 3.25a and 3.25b, where  $x_0^c$  to  $x_3^c$  and  $z_0^c$  to  $z_3^c$  represent the control points coordinates.

$$x(t) = x_0^c(1-t)^3 + 3x_1^c t(1-t)^2 + 3x_2^c t^2(1-t) + x_3^c t^3 \quad (3.25a)$$

$$z(t) = z_0^c(1-t)^3 + 3z_1^c t(1-t)^2 + 3z_2^c t^2(1-t) + z_3^c t^3 \quad (3.25b)$$

The leading edge thickness curve control points coordinates are determined via Equations

3.26.

$$x_0^c = 0 \qquad z_0^c = 0 \qquad (3.26a)$$

$$x_1^c = 0 \qquad z_1^c = 3\kappa_t(x_t - r_t)^2/2 + z_t \qquad (3.26b)$$

$$x_2^c = r_t \qquad z_2^c = z_t \qquad (3.26c)$$

$$x_3^c = x_t \qquad z_3^c = z_t \qquad (3.26d)$$

The trailing edge thickness curve control points coordinates are determined via Equations 3.27.

$$x_0^c = x_t \qquad z_0^c = z_t \qquad (3.27a)$$

$$x_1^c = 2x_t - r_t \qquad z_1^c = z_t \qquad (3.27b)$$

$$x_2^c = 1 + [th_{TE} - (3\kappa_t(x_t - r_t)^2/2 + z_t)] \cot \beta_{TE} \qquad z_2^c = 3\kappa_t(x_t - r_t)^2/2 + z_t \qquad (3.27c)$$

$$x_3^c = 1 \qquad z_3^c = th_{TE} \qquad (3.27d)$$

The leading edge camber curve control points coordinates are determined via Equations 3.28.

$$x_0^c = 0 \qquad z_0^c = 0 \qquad (3.28a)$$

$$x_1^c = r_c \cot \gamma_{LE} \qquad z_1^c = r_c \qquad (3.28b)$$

$$x_2^c = x_c - \sqrt{2(r_c - z_t)/3\kappa_c} \qquad z_2^c = z_c \qquad (3.28c)$$

$$x_3^c = x_c \qquad z_3^c = z_c \qquad (3.28d)$$

The trailing edge camber curve control points coordinates are determined via Equations 3.29.

$$x_0^c = x_c \qquad z_0^c = z_c \qquad (3.29a)$$

$$x_1^c = x_c + \sqrt{2(r_c - z_c)/3\kappa_c} \qquad z_1^c = z_c \qquad (3.29b)$$

$$x_2^c = 1 + (z_{TE} - r_c) \cot \alpha_{TE} \qquad z_2^c = r_c \qquad (3.29c)$$

$$x_3^c = 1 \qquad z_3^c = z_{TE} \qquad (3.29d)$$

The parameter  $r_t$  is the smallest root of Equation 3.30 that satisfies the condition  $\max(0, x_t -$

$$\sqrt{-z_t/3\kappa_t} < r_t < x_t.$$

$$27\kappa_t^2 r_t^4/4 - 27\kappa_t^2 x_t r_t^3 + (9\kappa_t z_t + 81\kappa_t^2 x_t^2/2)r_t^2 + (2r_{LE} - 18\kappa_t x_t z_t - 27\kappa_t^2 x_t^3)r_t + (3z_t^2 + 9\kappa_t x_t^2 z_t + 27\kappa_t^2 x_t^4/4) = 0 \quad (3.30)$$

The parameter  $r_c$  is calculated with Equation 3.31 and must satisfy the condition  $0 < r_c < z_c$ .

$$r_c = [16 + 3\kappa_c(\cot \gamma_{LE} + \cot \alpha_{TE})(1 + z_{TE} \cot \alpha_{TE})] / [3\kappa_c(\cot \gamma_{LE} + \cot \alpha_{TE})] \pm 4\sqrt{16 + 6\kappa_c(\cot \gamma_{LE} + \cot \alpha_{TE})(1 - z_c(\cot \gamma_{LE} + \cot \alpha_{TE}) + z_{TE} \cot \alpha_{TE})} \quad (3.31)$$

Regarding implementation, the parameters are determined directly from the initial aerofoil shape to obtain the initial design variables. If these variables do not satisfy the parameter conditions, the tool stops. During optimisation the conditions are checked for every aerofoil, if they are not fulfilled, a zero thickness aerofoil is returned.

### 3.4 Aerofoil evaluation

The aerofoil evaluation routine is responsible for the determination of the objective function value for each aerofoil, so that the optimisation algorithm is capable of ranking the design variables, more on that in Section 3.5.

The objective function value is a scalar based on the performance of the aerofoil and is obtained via the following algorithm, shown in Figure 3.5.

1. For each geometric property under constraints, compute its value and determine the penalty value. Then check whether it is over the penalty limit. If so, return the penalty value times  $10^6$  as the objective function value. However, if it is under, proceed to the next step;
2. Using XFOIL, analyse each operating point according with the input file options. Attempt to fix non convergence if the input options require it;
3. With the results from the XFOIL analysis, compare the lift and drag coefficients with previous ones for each point. Depending on the condition, analyse those points again at a perturbed Reynolds number, and keep the worst case for each property;
4. For each aerodynamic property under constraints, determine the penalty value. Upon doing so proceed in the same fashion as step 1;
5. Calculate the objective function value based on the specified aerodynamic coefficients and the total penalty value.



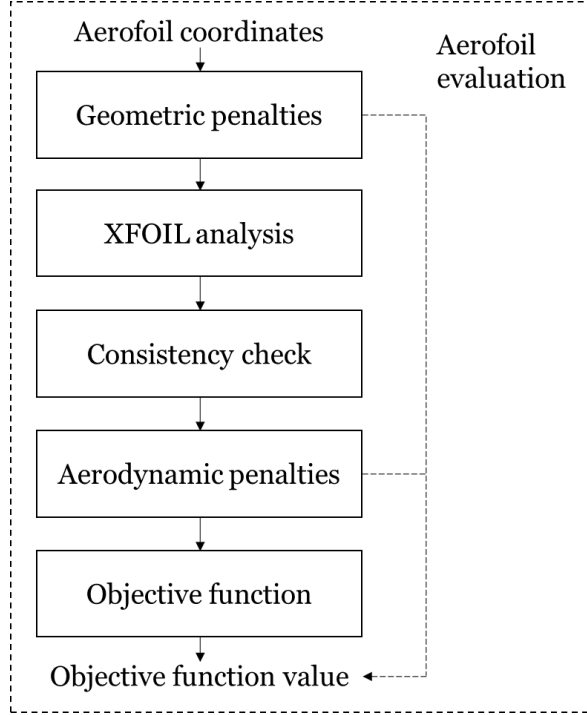


Figure 3.5: Aerofoil evaluation flowchart.

### 3.4.1 Penalties

The aerofoil can be constrained by geometric and aerodynamic properties. While the geometric constraints involve thickness, camber, trailing edge angle, leading edge angles, curvature, panel angles and growth rate, the aerodynamic constraints concern the drag, lift and moment coefficients as well as the RMSBL variable, which is the indicator of XFOIL convergence.

Each property  $j$  generates a penalty value  $\delta_j$  by using the ratio of the property value  $\sigma_j$  and a reference value and whether it is a lower limit or an upper limit, Equation 3.32. The reference value is the property limit, however in the case of the limit being 0 the value used is  $10^{-12}$  to avoid division by 0. A negative  $\delta_j$  means that the property is within its limits and there is no penalty.

$$\delta_j = \begin{cases} \frac{\sigma_j - \sigma_{ref,j}}{|\sigma_{ref,j}|} & \text{if it is a upper limit} \\ \frac{\sigma_{ref,j} - \sigma_j}{|\sigma_{ref,j}|} & \text{if it is a lower limit} \end{cases} \quad (3.32)$$

Each penalty value is compared with a penalty limit to check whether the tool should continue (if it is under the limit) or return the value of the penalty times a million as the objective function value (if it is over the limit), Equation 3.33. The process when aerofoil evaluation returns the value of a penalty times a million is called an exception. The penalty limit decreases during the optimisation to allow higher penalties during the start of the optimisation and force almost no penalties by the end, in order to allow higher exploration during optimi-

sation.

$$Obj = 10^6 \delta_j, \text{ if } \exists \delta_j > \delta_{limit} \quad (3.33)$$

The total penalty value  $\delta$  is the sum of all other positive penalties, Equation 3.34.

$$\delta = \sum_{j=1}^m \delta_j, \text{ if } 0 \leq \delta_j \leq \delta_{limit} \quad (3.34)$$

Regarding the geometric properties, several thickness properties can be constrained, such as the aerofoil minimum thickness, the aerofoil maximum thickness and thicknesses in specified chord positions. Figure 3.6 illustrates an example of a possible aerofoil thickness distribution with the aforementioned properties and limits.

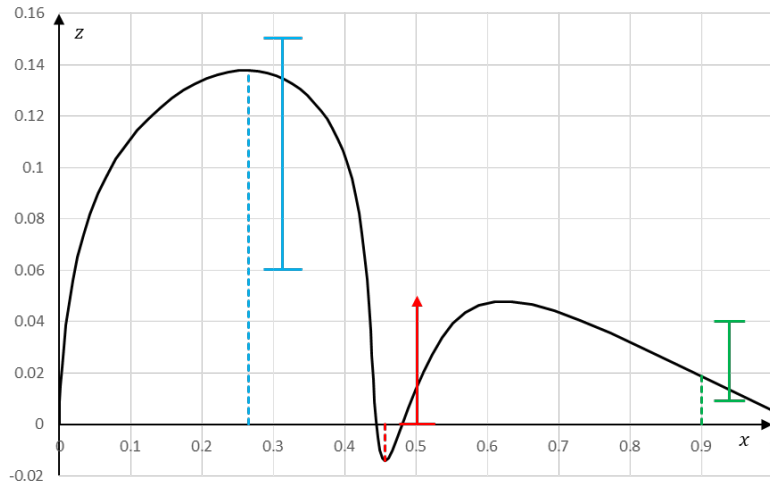


Figure 3.6: Potential aerofoil thickness distribution and relevant thickness properties for penalty calculation.

In the Figure 3.6, the maximum thickness (in blue) is constrained between 0.06 and 0.15 and its value is within the limits. The minimum thickness (in red) must be over 0, it does not satisfy the condition. Finally, the thickness at 90% of the chord length (in green) must be between 0.01 and 0.04, it is within the limits. In this example, the penalty values for maximum thickness and specified thickness are negative while the value for the minimum thickness is positive, additionally it is also very high (over  $10^{10}$ ), stopping the evaluation immediately and returning the minimum thickness penalty value times a million as the objective function value.

While the camber curve is of great significance for the aerofoil performance, the only camber

property used in the current tool is the aerofoil maximum camber, which may be constrained under a lower and upper limit. The leading edge camber angle and trailing edge camber angle as well as other camber properties are not available to be constrained since there was no need in the cases studied in this work.

The aerofoil minimum trailing edge thickness angle is the only trailing edge property available for constraints, upper and lower limits. However this angle refers to the angle near the trailing edge and not at it. A distance from the trailing edge is given, from which the angle is calculated at each point. Figure 3.7 shows a potential aerofoil thickness distribution and various angles.

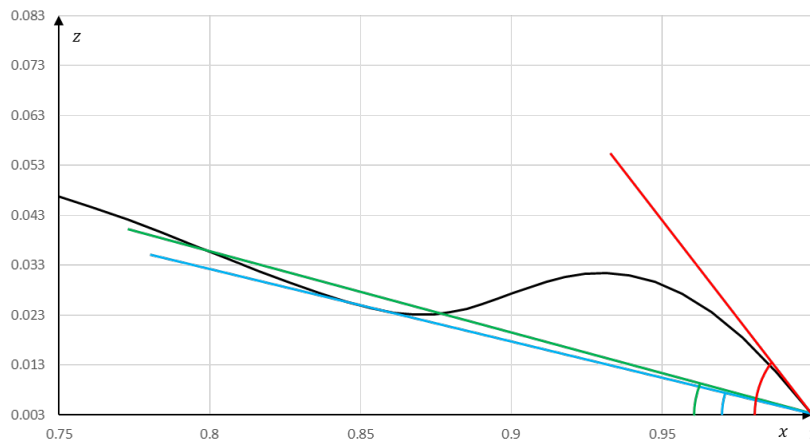


Figure 3.7: Potential aerofoil thickness distribution near trailing edge and angles for penalty calculation.

In the Figure 3.7, at a distance of 0.2 the angle in green is obtained, from 0.8 to 1.0 the minimum trailing edge thickness angle is in blue and true trailing edge thickness angle is in red. The reason for this constraint being available is to control the thickness near the trailing edge.

Two leading edge angles are available to be constrained: the upper surface angle and the lower surface angle. Determination of the angle is done by using the nearest point from the upper and lower surfaces. To these angles three limits are imposed: the maximum absolute value, the minimum absolute value and the maximum difference between its absolute values. These constraints evaluate the bluntness and sharpness of the leading edge and how similar the leading edge is for the upper and lower surfaces.

Regarding curvature, the available property is the number of curvature sign changes over a specified threshold along the upper or lower surfaces. Figure 3.8 shows a potential aerofoil upper surface and its curvature. A curvature threshold of 0.4 is represented in red in Figure 3.8b and position of the sign changes is shown in Figure 3.8a in blue if it is above the threshold and black if it is under, meaning that the upper surface has 4 curvature sign reversals. This constraint is directly linked to XFOIL analysis, since a high number of reversals usually leads to non convergence.

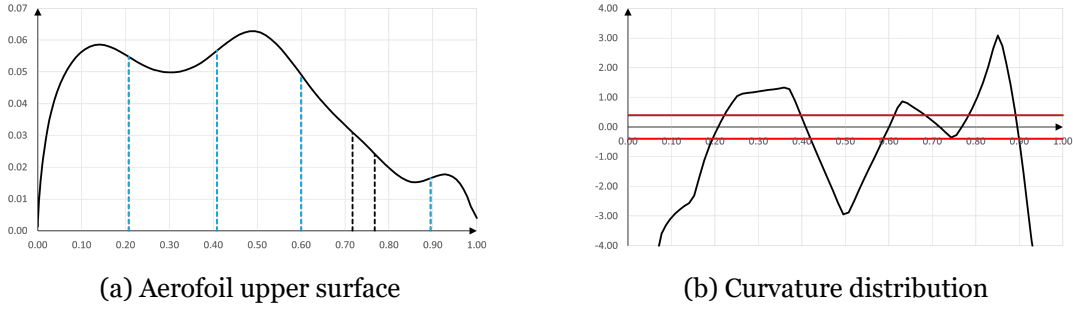


Figure 3.8: Potential aerofoil upper surface and respective curvature distribution for penalty calculation.

The panel angles and growth rate are used to detect high localized changes on the aerofoil surface. The panel angles property refers to the supplementary angle between three sequential points or two sequential panels, the maximum value of all panel angles is constrained. The growth rate is the ratio of two sequential panel lengths. The aerofoil maximum growth rate is constrained.

The convergence aerodynamic penalty checks for all operating points when RMSBL is under  $10^{-4}$ , which is the same value that XFOIL utilises for convergence. Therefore  $10^{-4}$  is its reference value.

The lift and moment coefficients minimum value for specified design points can be constrained as well as the drag coefficient maximum value. Since each design point has a weight these constrains allow for more control over the coefficients values during optimisation.

### 3.4.2 XFOIL analysis

XFOIL by Drela et al. [38] consists of a collection of menu-driven routines which perform the viscous or inviscid analysis and inverse calculations of aerofoils. The XFOIL documentation [48] mentions that XFOIL objective was to combine the speed and accuracy of high-order panel methods with the fully-coupled viscous/inviscid interaction method used in the ISES code developed by Drela and Giles.

According to the XFOIL documentation [48] in the viscous analysis, a two-equation lagged dissipation integral boundary layer formulation and an envelope  $e^n$  transition criterion depict the boundary layers and wake, i.e. the viscous solution. Additionally the incompressible potential flow interacts with it via the surface transpiration model, allowing for proper calculation of limited separation regions. The total velocity for each point on the aerofoil surface and wake is determined from the panel solution, leading to a non-linear elliptic system which is readily solved by a full-Newton method.

XOPTFOIL utilises the XFOIL routines directly from its source code, as external subroutines. To do so all XFOIL variables are declared in its own modules separate from the routines that use them, this is identical to XFOIL with its .INC files. This separation allows for a

straightforward parallelization of XFOIL.

In XOPTFOIL two modules are of particular interest. The first module named `xfoil_inc` is where the main XFOIL variables are declared and stored. The second module `xfoil_driver` is responsible for connecting XOPTFOIL to XFOIL by executing the XFOIL analysis in accordance with the operating points conditions and XFOIL options via the Xfoil analysis routine.

The Xfoil analysis routine input consists of all operating points aerodynamic conditions, XFOIL panelling and run options, aerofoil coordinates and flap variables. Its output are the relevant aerodynamic properties such as angle of attack, lift, drag and moment coefficients and the XFOIL variable RMSBL (root mean squares of the boundary layer) which ascertains XFOIL convergence.

The Xfoil analysis routine implementation is shown in Figure 3.9 and can be summarized as:

1. Call `xfoil_inc` module, initialize its variables according with the XFOIL options, in particular whether it is an inviscid or viscous analysis, the maximum number of iterations, the viscous solution acceleration variable VACCEL, the trip wire positions and global Ncrit, then call BLPINI to initialize the boundary layer parameters;
2. Perform aerofoil handling:
  1. Pass aerofoil coordinates to XFOIL variables;
  2. Run PANGEN routine in order to conform to XFOIL panelling options;
  3. Apply a simple flap on the aerofoil based on the flap hinge position and angle of deflection.
3. Set local values such as Reynolds number, Mach number and Ncrit, run compressibility routine COMSET and check whether to reinitialize the aerofoil boundary layer and set the XFOIL variables (LIPAN and LBLINI) accordingly;
4. Check analysis type:
  - a. If the operating point is not a sequence of angles of attack and it is not using a initialization sequence then:
    - i. Perform single point analysis: pass angle of attack or lift coefficient to XFOIL variables and call SPECAL or SPECCL, respectively, to calculate the inviscid flow then call VISCAL to determine the viscous flow;
    - ii. Check convergence: if the flow has not converged and initialization sequence for non convergence is active, then go to step 4.b or else continue to step 5.
  - b. If the operating point is not a sequence of angles of attack and it is using an initialization sequence, create an initialization sequence of angles of attack or lift coefficients and analyse each point in the sequence in the same manner as the single point analysis in step 4.a.i without reinitialization of the aerofoil boundary layer;
  - c. If the operating point involves an analysis of a given sequence of angles of attack, analyse each point in the sequence in the same manner as the single point analysis in step 4.a.i without reinitialization of the aerofoil boundary layer, store the

- relevant aerodynamic properties for each point and choose which point to pass as result based on the objective;
5. Check whether the current operating point is the last:
    - a. If it is not, continue to step 2 to analyse the next operating point;
    - b. If it is, return the aerodynamic properties and exit this routine.

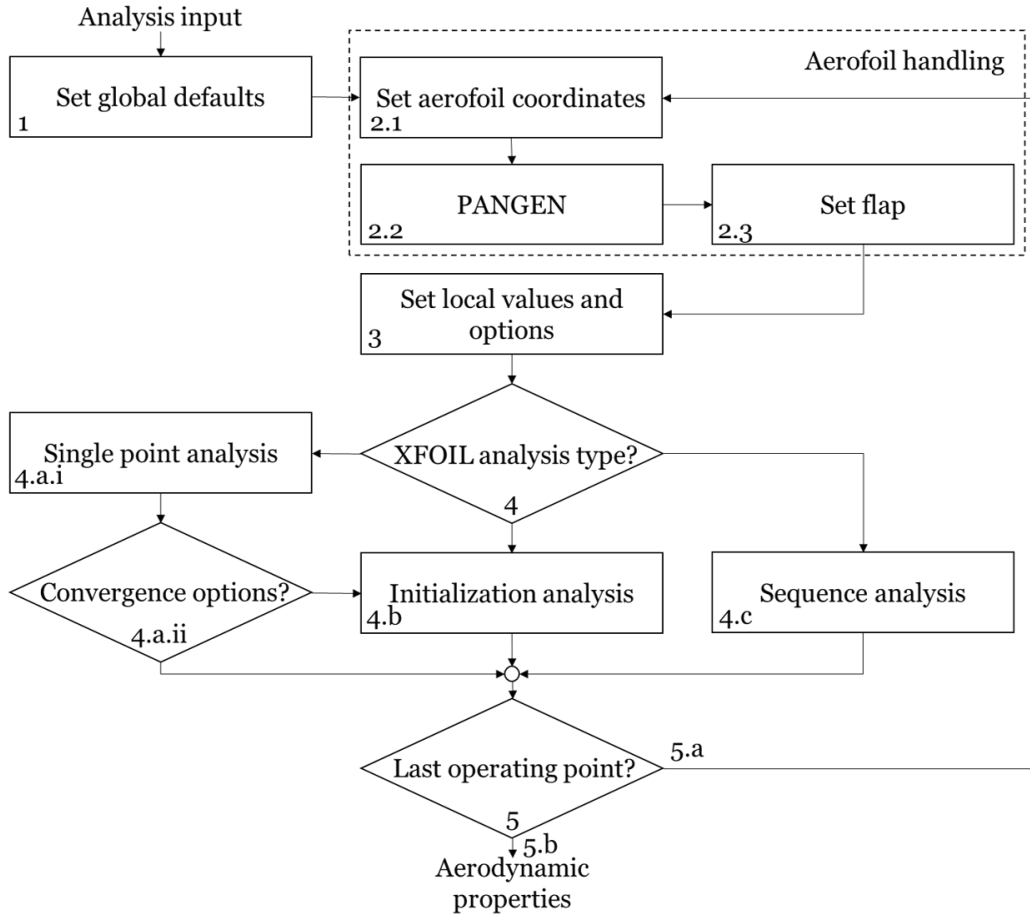


Figure 3.9: Flowchart of the Xfoil analysis routine.

The several parameters that control the analysis routine can be summarized as:

1. General XFOIL options: general  $N_{crit}$  value for the  $e^n$  model, position for upper and lower surface trip wire, whether it is an inviscid or viscous analysis, maximum number of iterations, VACCEL parameter for viscous solution acceleration and whether to reinitialize the boundary layer after each operating point calculation;
2. Standard XFOIL paneling options: number of panels  $NPAN$ , panel bunching parameter  $CVPAR$ , trailing edge over leading edge panel density ratio  $CTERAT$ , refining area over leading edge panel density ratio  $CTRRAT$ , upper surface refining area limits  $XSREF1$  and  $XSREF2$  and lower surface refining area limits  $XPREF1$  and  $XPREF2$ ;
3. Operating point options: type of operating point (single or sequence), whether it uses the angle of attack or lift coefficient as a constant, its value (or start, step and end for

a sequence), Reynolds number, Mach number, Ncrit, flap angle deflection and the flap hinge coordinates;

4. Operating point initialization sequence options: when to start an initialization sequence (always, never or if XFOIL solution has not converged), number of points ( $n_{init}$ ), angle of attack reference ( $\alpha_{0,init}$ ), lift coefficient reference ( $C_{l,0,init}$ ), starting position ( $p_{0,init}$ ) and type of distribution, either linear or sinusoidal.

Regarding obtaining the operating point initialization sequence, the non-dimensional sequence is calculated in Equation 3.35 with  $p_{0,init} \in [0, 1]$ .

$$p_i = \begin{cases} \frac{i-1}{n_{init}-1} \cdot (1 - p_{0,init}) + p_{0,init} & \text{if linear} \\ \sin\left(\frac{\pi}{2} \frac{i-1}{n_{init}-1}\right) \cdot (1 - p_{0,init}) + p_{0,init} & \text{if sinusoidal} \end{cases}, \forall i \in [1, n_{init}] \quad (3.35)$$

Following it, the angle of attack sequence or lift coefficient sequence can be determined in Equation 3.36.

$$\begin{cases} \alpha_i & = \alpha - (1 - p_i) \cdot (\alpha - \alpha_{0,init}) \\ C_{l,i} & = C_l - (1 - p_i) \cdot (C_l - C_{l,0,init}) \end{cases}, \forall i \in [1, n_{init}] \quad (3.36)$$

With this sequence and keeping the same values of all other operating point options, it is possible to systematically analyse each point in the sequence. As an important note, if a point does not converge in a sequence, the boundary layer is reinitialized for the next point.

Considering operating point sequence analysis, this function is only triggered when determining the maximum lift coefficient of an aerofoil for given aerodynamic conditions. Due to the nature of the sequence, i.e., linear with a fixed start, end and step, it should strive to end after the maximum lift coefficient, in a region where convergence is hard to achieve. Additionally, it is impossible to exactly predict where the maximum lift occurs, meaning that a sparse sequence must be used.

After the XFOIL analysis routine is run, a consistency check is executed. Lift and drag coefficients are compared with the overall maximum lift and minimum drag coefficients times a user specified tolerance during the optimisation for each operating point, Equation 3.37.

$$\begin{cases} C_{l,i} > (1 + tol_{lift}) \cdot C_{l,max,i} \\ C_{d,i} < (1 - tol_{drag}) \cdot C_{d,min,i} \end{cases}, \forall i \in [1, N_{op}] \quad (3.37)$$

The points, at which any of the conditions are true, are analysed again at a perturbed Reynolds 0.3% lower than its original. The worst of the two results is kept, that is the lowest lift and moment coefficients, the highest drag coefficient and the highest RMSBL, meaning that the consistency check must also converge. At the end of aerofoil evaluation, the maximum lift coefficient and minimum drag coefficient for each point are updated.

The reason for this consistency check is an attempt at avoiding XFOIL exploitation by the optimisation, i.e. XFOIL analysis presents an incorrect particular value which improves the objective function significantly, then the optimisation attempts to replicate the process. At times, the given aerofoil aerodynamic performance presents peculiar values for drag coefficient or lift coefficient on the operating point, while a small perturbation of angle of attack, lift coefficient or Reynolds number exhibits significantly different results. The Reynolds number was chosen for this perturbation due to the ease of implementation.

### 3.4.3 Objective function

The objective function  $Obj$  is the sum of the relative operating point aerodynamic objectives times the operating point weights plus the total penalty, Equation 3.38. The magnitude of each objective should not influence  $Obj$ , thus the use of relative objectives.

$$Obj = \sum_{i=1}^{N_{op}} \left( \bar{w}_i \cdot \frac{\varphi_i}{\varphi_{i,ref}} \right) + \delta \quad (3.38)$$

In the input file, both the operating points objective and weight are provided to the tool. The weights are normalised by the total weight value, Equation 3.39.

$$\bar{w}_i = \frac{w_i}{\sum_1^{N_{op}} w_i} \quad (3.39)$$

The operating points objective indicate which objective to use, Equation 3.40 shows the main operating points objectives and its equivalent aerodynamic objective ( $\varphi_i$ ). Note that only aerodynamic objectives are available and the aerodynamic objective is the inverse of operating point objective for most cases. Target property indicates that there is a specific value to



be targeted by a given property.

$$\left\{ \begin{array}{l} \varphi_i = \frac{1}{C_l}, \text{ if maximum } C_l \\ \varphi_i = C_d, \text{ if minimum } C_d \\ \varphi_i = \frac{C_d}{C_l}, \text{ if maximum } \frac{C_l}{C_d} \\ \varphi_i = \frac{C_d}{C_l^{\frac{3}{2}}}, \text{ if maximum } \frac{C_l^{\frac{3}{2}}}{C_d} \\ \varphi_i = \left( \frac{prop_{target} - prop}{prop} \right)^2, \text{ if target property} \end{array} \right. , \forall i \in [1, N_{op}] \quad (3.40)$$

The reference aerodynamic objective  $\varphi_{i,ref}$ , is obtained from Equation 3.40 for the initial aerofoil. Given that the relative aerodynamic objective is utilised in the objective function, when the lift coefficient is fixed for a given operating point, several objectives become equivalent (minimum  $C_d$ , maximum  $\frac{C_l}{C_d}$  and maximum  $\frac{C_l^{\frac{3}{2}}}{C_d}$ ) or irrelevant (maximum  $C_l$ ). The operating point objective input also indicates whether to use a sequence of angle of attack when maximizing the lift coefficient.

#### 3.4.4 Weight determination

This section presents the method used for choosing the aerodynamic properties to optimise and the determination of each weight based on four operational objectives and a condition relevant to the case studies. The aerodynamic properties to optimise are a collection of lift and drag coefficients in various aerodynamic conditions. Analysis of each property requires a Reynolds number, Mach number and either angle of attack or lift coefficient to serve as constants.

The objectives are the maximum payload weight, the least amount of time on a set course, maximum flown distance within a set amount of time and the maximum altitude reached within a given time for a small electric UAV. The condition is keeping the take-off distance within given limits.

Regarding the take-off distance, Equations 3.41 and 3.42 present the relevant properties to the takeoff distance  $S_G$  calculation, adapted from the book by Raymer [49]. These are: initial and final velocity  $V_i$  and  $V_f$ , thrust  $T$ , aircraft weight  $W$ , ground friction coefficient  $\mu_G$ , wing area  $S$ , air density  $\rho$  and aircraft lift coefficient and drag coefficient  $C_L$  and  $C_D$ .

$$S_G = \frac{W (V_f^2 - V_i^2)}{2g \left( T - \mu_G W - \frac{\rho S V_{AC}^2}{2} (C_D - \mu_G C_L) \right)} \quad (3.41)$$

with the average velocity during acceleration  $V_{AV}$  being,

$$V_{AV} = \sqrt{\frac{V_f^2 + V_i^2}{2}} \quad (3.42)$$

The final velocity is considered to be the lift off velocity  $V_{LO}$  given by the stall velocity  $V_S$  times a factor, Equation 3.43 and the initial velocity is the wind velocity  $V_W$ , assuming take-off is executed against the wind, when calculating the average velocity, which is relative to the wind. When calculating the distance, the velocities are relative to the ground, thus the initial velocity is zero and the final velocity is the take-off velocity minus the wind speed.

$$V_{LO} = factor \cdot V_S = factor \sqrt{\frac{2W}{\rho S C_{L,max}}} \quad (3.43)$$

Therefore, take-off distance depends on the aircraft maximum lift coefficient, lift coefficient, drag coefficient and weight. Which are dependent on the aerofoil maximum lift coefficient and aerofoil lift and drag coefficients during take-off. By assuming that the initial take-off distance is already near the limit, the condition for take-off distance variation  $\delta S_G$  is established, Equation 3.44.

$$\delta S_G = \frac{\partial S_G}{\partial C_{l,max}} \delta C_{l,max} + \frac{\partial S_G}{\partial C_l} \delta C_l + \frac{\partial S_G}{\partial C_d} \delta C_d + \frac{\partial S_G}{\partial W} \delta W \leq 0 \quad (3.44)$$

By assuming that  $S_G$  does not vary ( $\delta S_G = 0$ ), the weight variation is given by Equation 3.45.

$$\delta W = \left( \frac{\partial S_G}{\partial W} \right)^{-1} \cdot \left( -\frac{\partial S_G}{\partial C_{l,max}} \delta C_{l,max} - \frac{\partial S_G}{\partial C_l} \delta C_l - \frac{\partial S_G}{\partial C_d} \delta C_d \right) \quad (3.45)$$

The payload weight is part of the aircraft weight, leading to Equation 3.46.

$$\delta W_{payload} = \frac{\partial W_{payload}}{\partial W} \delta W \quad (3.46)$$

Thus,  $C_{l,max}$ ,  $C_l$  and  $C_d$  during take-off are the aerodynamic properties to optimise. For analysis  $Re$  and  $M$  serve as constants. Since  $C_{l,max}$  requires knowledge of the lift curve, a sequence of angles of attack must be utilised. For  $C_l$  and  $C_d$  a single angle of attack is used.

The maximum altitude reached within a given time can be represented by the maximum vertical velocity during climbing. Raymer [49] presents the following Equation 3.47 for vertical velocity, where velocity  $V$ , drag  $D$ , thrust  $T$  and weight  $W$  are only variables.

$$V_V = V \left( \frac{T - D}{W} \right) \quad (3.47)$$

Assuming that the angle of climb  $\gamma$  is small, Equation 3.48 establishes the velocity relationships. Therefore the vertical velocity also depends on the lift coefficient.

$$L = W \cos \gamma \approx W \Leftrightarrow V = \sqrt{\frac{2W}{\rho S C_L}} \quad (3.48)$$

From the previous Equations, it is possible to observe that lift coefficient, drag coefficient and weight are the main variables which influence the vertical velocity, Equation 3.49. Due to the presence of weight as a variable, all the variables that impact weight also impact the vertical velocity, as long as the take-off distance condition is forced.

$$\delta V_V = \frac{\partial V_V}{\partial C_l} \delta C_l + \frac{\partial V_V}{\partial C_d} \delta C_d + \frac{\partial V_V}{\partial W} \delta W \quad (3.49)$$

Therefore,  $C_l$  and  $C_d$  during climb are added to the list of properties to optimise. Obviously, the  $Re$ ,  $M$  and  $\alpha$  during climb are utilised as constants for analysis.

Finally the least amount of time on a set course objective is equivalent to maximum velocity. However the course has two stages, sustained turns (turn) and level flights (cruise) according to the first case study regulation [50]. Since in the second case study regulation [51] there is a free course, the same flight course is used, i.e. ten sprints of 100 m, each sprint is followed by 180 degrees turn. Equation 3.50 presents the relationship between the two velocities and the objective, while Equation 3.51 presents the physical relation between time and velocity, i.e. distance  $\hat{d}$ .

$$\delta t_{flight} = \frac{\partial t_{flight}}{\partial V_{turn}} \delta V_{turn} + \frac{\partial t_{flight}}{\partial V_{cruise}} \delta V_{cruise} \quad (3.50)$$

$$t_{flight} = \frac{\hat{S}_{turn}}{V_{turn}} + \frac{\hat{S}_{cruise}}{V_{cruise}} \quad (3.51)$$

For level flight, drag is equal to thrust and lift is equal to weight. A decrease in drag coefficient, when both weight and thrust are constant, forces drag to remain constant, velocity to increase and lift coefficient to decrease, meaning that lift coefficient is not an independent variable, leading to Equation 3.52

$$\delta V = \frac{\partial V}{\partial C_d} \delta C_d \quad (3.52)$$

Considering the turn, and assuming a sustained turn, drag is equal to thrust and lift is equal to weight times a load factor. By assuming the load factor to remain constant along with the same considerations as level flight, turn velocity only depends on aerofoil drag coefficient, Equation 3.53.

$$\delta V = \frac{\partial V}{\partial C_d} \delta C_d \quad (3.53)$$

The  $C_d$  during level flight and during turns are the last properties to be added to the list of properties to optimise. For analysis  $Re$  and  $M$  are utilised as constants, however both lift coefficient or angle of attack are potential constants. Since level flight and sustained turns are closely linked with aircraft weight, the lift coefficient is used as constant for both situations.

The operational objective, maximum flown distance within a set amount of time is also equivalent to maximum velocity, Equation 3.54.

$$\delta \hat{S}_{flight} = \frac{\partial \hat{S}_{flight}}{\partial V_{turn}} \delta V_{turn} + \frac{\partial \hat{S}_{flight}}{\partial V_{cruise}} \delta V_{cruise} \quad (3.54)$$

Assuming that the flight consists solely of level flight and sustained turn, the flown distance

is given by Equation 3.55.

$$\hat{S}_{flight} = t_{turn}V_{turn} + t_{cruise}V_{cruise} \quad (3.55)$$

Having identified the various aerodynamic properties to optimise  $\psi$ , it is now required to determine each weight so that  $\delta Obj \propto -\delta Score$ , i.e. the minimum of the XOPTFOIL objective  $Obj$  corresponds to the maximum of the competition objective  $Score$ . The case study objective is a combination of the operational objectives  $\sigma$  already presented.

Considering that the XOPTFOIL objective function is an aggregation of relative properties, each property weight determines how relevant the relative property is to the objectives. Meaning, XOPTFOIL objective function utilises a first order model to describe the objective. Therefore the weights are in fact the derivatives of the relative objectives by the relative properties, Equation 3.56. Notice that the objectives are also relative, this is a necessity to avoid units in the objective function.

$$\hat{w}_{i,j} = \frac{\partial \frac{\sigma_j}{\sigma_{j,ref}}}{\partial \frac{\psi_i}{\psi_{i,ref}}} = \frac{\partial \sigma_j}{\partial \psi_i} \frac{\psi_{i,ref}}{\sigma_{j,ref}} = \frac{\partial \bar{\sigma}_j}{\partial \psi_i} \quad \forall i \in [1, n_\psi] \quad \forall j \in [1, n_\sigma] \quad (3.56)$$

Since the case objective is a combination of the operational objectives, the weight for the objective function is the combination of all objectives weights for the same property, Equation 3.57.

$$w_i = \sum_{j=1}^{n_\sigma} \hat{w}_{i,j} \quad \forall i \in [1, n_\psi] \quad (3.57)$$

### 3.5 Optimisation

Particle swarm optimisation (PSO) with a variable inertia weight was the optimisation algorithm utilised in this work, identical to the one described by Piotrowski et al. [52], the main difference is the use of rate for the inertia. This algorithm already was part of XOPTFOIL, the only changes made were to the design radius and the design functions limits.

In PSO the design variables are denoted as position  $\mathbf{X}$ . During optimisation the position of each particle  $j$  of the population  $N_{pop}$  changes depending on previous velocity  $\mathbf{V}_{t-1,j}$  and previous position  $\mathbf{X}_{t-1,j}$ , Equation 3.58.

$$\mathbf{X}_{t,j} = \mathbf{X}_{t-1,j} + \mathbf{V}_{t-1,j} \quad \forall j \in [1, N_{pop}] \quad (3.58)$$

Velocity is also updated with each iteration, Equation 3.59. Current particle velocity  $\mathbf{V}_{t,j}$  depends on the previous velocity  $\mathbf{V}_{t-1,j}$  times an inertia weight  $w_t$ , the current particle best position  $\mathbf{X}_{p,best}$  and the previous position  $\mathbf{X}_{t-1,j}$  difference times the cognitive acceleration factor  $c_1$  and the current global (swarm) best position  $\mathbf{X}_{g,best}$  and the previous position  $\mathbf{X}_{t-1,j}$  difference times the social acceleration factor  $c_2$ . Velocity change towards the best positions also depends on two uniform random numbers from 0 to 1  $R_{(0,1),p}$  and  $R_{(0,1),g}$ .

$$\mathbf{V}_{t,j} = w_t \mathbf{V}_{t-1,j} + c_1 (\mathbf{X}_{p,best} - \mathbf{X}_{t-1,j}) R_{(0,1),p} + c_2 (\mathbf{X}_{g,best} - \mathbf{X}_{t-1,j}) R_{(0,1),g} \quad \forall j \in [1, N_{pop}] \quad (3.59)$$

The inertia weight varies during optimisation, Equation 3.60, depending on the previous weight  $w_{t-1}$ , the final weight  $w_f$  and a rate  $w_{rate}$ .

$$w_t = w_{t-1} - w_{rate} (w_{t-1} - w_f) \quad (3.60)$$

From Equations 3.58, 3.59 and 3.60 note the parameters  $c_1$ ,  $c_2$ ,  $w_0$ ,  $w_f$  and  $w_{rate}$  are required. In XOPTFOIL these can be changed by user inputs. Additionally, the algorithm also requires an initial position and velocity for each particle.

The initial positions are chosen at random within the design variables limits as described by Juárez-Castillo et al. [53], Equation 3.61, where  $\mathbf{X}_{max}$  and  $\mathbf{X}_{min}$  are the upper and lower limits of the design variables. Each random number impacts only a single design variable  $i$ .

$$X_{0,i,j} = (X_{i,max} - X_{i,min}) R_{(0,1)} + X_{i,min} \quad \forall i \in [1, N_{DV}] \quad \forall j \in [2, N_{pop}] \quad (3.61)$$

There is one exception, the first particle takes the initial position directly from the initial design variables, Equation 3.62. If no other particles have passed the constraints, this particle will set the global best and force convergence to positions near to it. Eventually some particle should surpass it as global and particle best.

$$\mathbf{X}_{0,j=1} = \mathbf{X}_{init} \quad (3.62)$$

The initial velocities are determined at random up to its limit  $V_{max}$  in any direction (uniform random number from -1 to 1  $R_{(-1,1)}$ ), Equation 3.63.

$$V_{0,i,j} = V_{max} R_{(-1,1)} \quad \forall i \in [1, N_{DV}] \quad \forall j \in [1, N_{pop}] \quad (3.63)$$

The upper ( $X_{max}$ ) and lower ( $X_{min}$ ) limits of the design variables are functions of an absolute initial perturbation ( $\xi_{abs}$ ), a relative initial perturbation ( $\xi_{rel}$ ) and the initial design variables ( $X_{init}$ ) in accordance with Equations 3.64 and 3.65 for each design variable  $i$ . The main change to this algorithm relative to the original in XOPTFOIL, is the introduction of the relative initial perturbation. This perturbation allows more control over the limits without the need to manually set the design variables' limit values.

$$X_{i,max} = X_{i,init} + X_{i,init} \cdot \xi_{rel} + \xi_{abs} \quad \forall i \in [1, N_{DV}] \quad (3.64)$$

$$X_{i,min} = X_{i,init} - X_{i,init} \cdot \xi_{rel} - \xi_{abs} \quad \forall i \in [1, N_{DV}] \quad (3.65)$$

While for most cases the design variables limits are used only for initialization of the population, some variables are constrained, such as flap deflection. When a variable is constrained,  $X_{min}$  and  $X_{max}$  use the constraint limit instead of previous Equations 3.64 and 3.65. The set of all constrained variables is named  $DV_{constrained}$ . Overflow of constraints is handled using Equations 3.66, 3.67, 3.68 and 3.69, by setting the design variable to the limit and inverting the velocity direction and changing its magnitude.

$$X_{t,i,j} = X_{min,i} \text{ if } X_{t,j,i} < X_{min,i} \quad \forall i \in DV_{constrained} \quad \forall j \in [1, N_{pop}] \quad \forall k \quad (3.66)$$

$$V_{t,i,j} = -V_{t,j,i} R_{(0,1)} \text{ if } X_{t,j,i} < X_{min,i} \quad \forall i \in DV_{constrained} \quad \forall j \in [1, N_{pop}] \quad \forall k \quad (3.67)$$

$$X_{t,i,j} = X_{max,i} \text{ if } X_{t,j,i} > X_{max,i} \quad \forall i \in DV_{constrained} \quad \forall j \in [1, N_{pop}] \quad \forall k \quad (3.68)$$

$$V_{t,i,j} = -V_{t,j,i} R_{(0,1)} \text{ if } X_{t,i,j} > X_{max,i} \quad \forall i \in DV_{constrained} \quad \forall j \in [1, N_{pop}] \quad \forall k \quad (3.69)$$

If the speed limit is exceeded, the velocity vector ( $V_{t,j}$ ) modulus is set to the limit without changing the direction using Equation 3.70.

$$V_{t,j} = \frac{V_{max}}{\|V_{t,j}\|} V_{t,j} \text{ if } \|V_{t,j}\| > V_{max} \quad (3.70)$$

The particle swarm optimisation algorithm is summarized in Figure 3.10. Several parts have already been addressed, in particular: initializing position and velocity and computing new positions and velocities. Aerofoil parametrization and aerofoil evaluation are responsible for position evaluation. All positions are known, thus this process can be parallelized. Parallelization simply means that multiple positions are evaluated at the same, i.e. in parallel. Note that finding the best positions is trivial, since the best positions have the lowest evaluation.

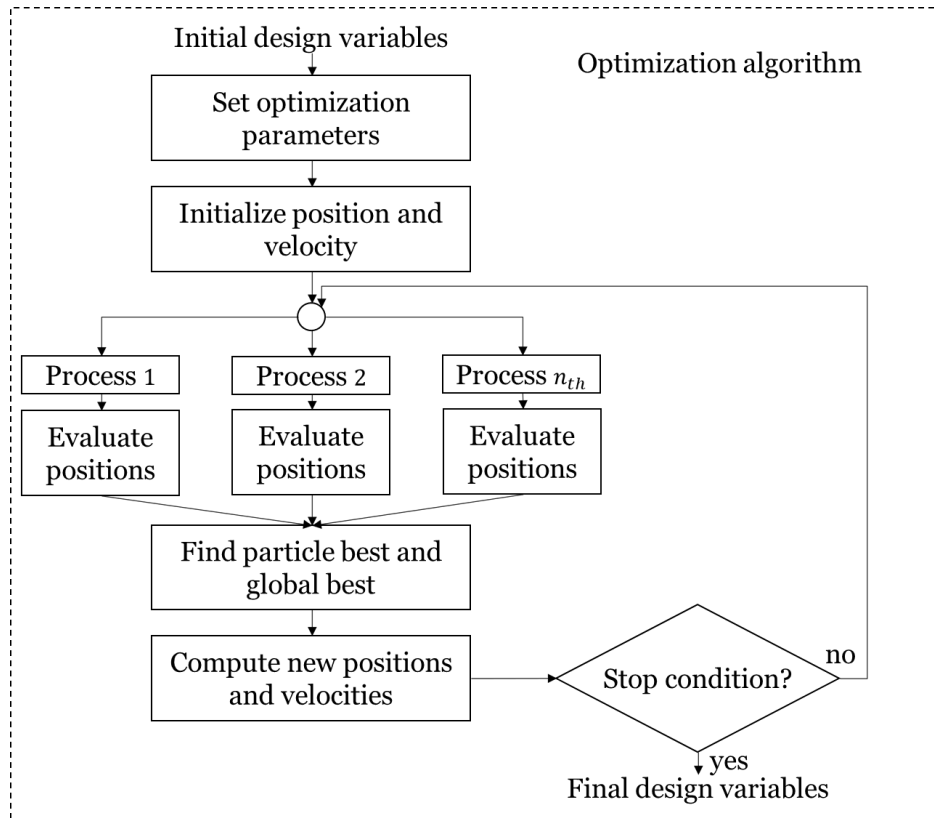


Figure 3.10: Optimisation algorithm flowchart.

The final process in the algorithm is the stop condition. There are two stop conditions, from which a single condition is sufficient to terminate the optimisation, these are:

- The iteration step  $t$  has reached its limit  $max_{steps}$ ;



- The population has converged. The design radius  $r$  measures the diversity of the population, when  $r$  is under the convergence limit  $r_{limit}$  the population has converged.

To calculate the design radius, the design variables are scaled between -1 and 1 for the entire population by the design variables limits, Equation 3.71. This scaling ensures that the magnitude of each design variable has no effect on the design radius.

$$\bar{X}_{i,j} = -1 + 2 \frac{X_{t,i,j} - X_{min,i}}{X_{max,i} - X_{min,i}} \quad \forall i \in [1, N_{DV}] \quad \forall j \in [1, N_{pop}] \quad (3.71)$$

Then the centroid ( $\bar{X}_c$ ) for each design variable is computed, Equation 3.72.

$$\bar{X}_{c,i} = \frac{\sum_{j=1}^{N_{pop}} \bar{X}_{i,j}}{N_{pop}} \quad \forall i \in [1, N_{DV}] \quad (3.72)$$

Finally, the design radius of the population is computed by determining the distance from the position to the centroid and dividing by the number of design variables for each particle, denominated particle radius  $r_j$ . The average of all particle radii is the design radius, Equation 3.73.

$$r = \frac{\sum_{j=1}^{N_{pop}} \frac{\|\bar{\mathbf{X}}_j - \bar{\mathbf{X}}_c\|}{N_{DV}}}{N_{pop}} = \frac{\sum_{j=1}^{N_{pop}} r_j}{N_{pop}} \quad (3.73)$$

Note that in Equation 3.73, when determining the particle radius  $r_j$ , the modulus of difference of the design variables and the centroid was divided by  $N_{DV}$ . This was to decrease how much the particle radius is dependant on the number of design variables. However it does not remove its influence over it, to do so it should be divided by  $2\sqrt{N_{DV}}$ . The corrected design radius  $r_{corrected}$  utilises this division.



# Chapter 4

## Analysis cases

This chapter is divided in three parts: aircraft presentation and the analysis of two case studies. In each case study the problem is defined and the results are presented and discussed. However the case studies have different optimisation objectives and serve different purposes in this work.

The optimisation objectives are two versions of the Air Cargo Challenge competition, 2019 for case 1 and 2022 for case 2. The competition is hosted every two years by the winning team of the previous event, with slight modification to the rules and objectives.

In case 1, different aerofoil parametrization methods are used during optimisation to show case their differences and demonstrate their implementation.

For case 2 a single analysis is performed, however its results are analysed in greater detail and are used to analyse the penalty limit, consistency check and the XFOIL initialization analysis of the tool.

### 4.1 Aircraft parameters and properties

In this section the aircraft used for both case studies is presented and relevant properties are shown. Figure 4.1 shows the aircraft used by the AERO@UBI team in the ACC2019 competition.



Figure 4.1: Aircraft used by the AERO@UBI team in the ACC2019 competition.

In Table 4.1 the values for the wingspan  $b$ , chord length  $c$ , wing area  $S$ , total aircraft weight  $W$ , payload weight  $W_{payload}$ , air density  $\rho$  and air viscosity  $\mu$  are presented for all cases. Notice that the air properties are in this table, altitude is considered at sea level regardless of flight condition. These are the reference values when determining the relative derivatives.

Table 4.1: General aircraft parameters and air properties.

$b$ [m]	$c$ [m]	$S$ [m <sup>2</sup> ]	$W$ [N]	$W_{payload}$ [N]	$\rho$ [kg/m <sup>3</sup> ]	$\mu$ [kg/(m · s)]
3.725	0.3	1.1175	117.5442	80.17	1.225	1.7709E-05

Table 4.2 shows the relevant take-off properties values, particularly, wind velocity  $V_W$ , stall velocity  $V_S$ , lift-off velocity  $V_{LO}$ , average velocity  $V_{AV}$ , lift  $L$ , drag  $D$ , thrust  $T$ , ground friction coefficient  $\mu_G$ , take-off distance  $S_G$ , Reynolds number  $Re$ , angle of attack  $\alpha$ , aircraft maximum lift coefficient  $C_{L,max}$ , aircraft lift coefficient  $C_L$ , aircraft drag coefficient  $C_D$ , aerofoil maximum lift coefficient  $C_{l,max}$ , aerofoil lift coefficient  $C_l$  and aerofoil drag coefficient  $C_d$ . These are the reference values when determining the relative derivatives for take-off.

Table 4.2: Relevant take-off properties.

$V_W$ [m/s]	$V_S$ [m/s]	$V_{LO}$ [m/s]	$V_{AV}$ [m/s]	$L$ [N]	$D$ [N]	$T$ [N]
1.944	9.752	10.727	7.709	36.22	2.184	17.78
$\mu_G$	$S_G$ [m]	$Re$	$\alpha$ [deg]	$C_{L,max}$	$C_L$	$C_D$
0.055	59.94	1.5998E+05	1.483	1.806	0.890	0.0537
$C_{l,max}$	$C_l$	$C_d$				
2.006	0.937	0.0243				

Table 4.3 introduces the values of relevant climb properties, such as aircraft velocity  $V$ , stall velocity  $V_S$ , vertical velocity  $V_V$ , lift  $L$ , drag  $D$ , thrust  $T$ , climb angle  $\gamma$ , aircraft lift coefficient  $C_L$ , aircraft drag coefficient  $C_D$ , angle of attack  $\alpha$ , Reynolds number  $Re$ , aerofoil lift coefficient  $C_l$  and aerofoil drag coefficient  $C_d$ . These are the reference values when determining the relative derivatives for climb.

Table 4.3: Relevant climb properties.

$V$ [m/s]	$V_S$ [m/s]	$V_V$ [m/s]	$L$ [N]	$D$ [N]	$T$ [N]	$\gamma$ [deg]
12.148	9.934	0.960	117.54	6.31	15.60	4.53
$C_L$	$C_D$	$\alpha$ [deg]	$Re$	$C_l$	$C_d$	
1.164	0.0625	4.96	2.521E+05	1.199	0.0155	

In Table 4.4, the values for aircraft velocity  $V$ , stall velocity  $V_S$ , lift  $L$ , drag  $D$ , aircraft lift coefficient  $C_L$ , aircraft drag coefficient  $C_D$ , Reynolds number  $Re$ , angle of attack  $\alpha$ , aerofoil lift coefficient  $C_l$  and aerofoil drag coefficient  $C_d$  are presented for level flight. These are the reference values when determining the relative derivatives for cruise.

The final Table with properties shows the relevant properties values for sustained turn, particularly aircraft velocity  $V$ , stall velocity  $V_S$ , load factor  $n$ , lift  $L$ , drag  $D$ , turn radius  $R$ ,

Table 4.4: Relevant level flight properties.

$V$ [m/s]	$V_S$ [m/s]	$L$ [N]	$D$ [N]	$C_L$	$C_D$
27.522	10.165	117.54	8.86	0.227	0.0171
$Re$	$\alpha$ [deg]	$C_l$	$C_d$		
5.713E+05	0.41	0.258	0.0096		

aircraft lift coefficient  $C_L$ , aircraft drag coefficient  $C_D$ , Reynolds number  $Re$ , angle of attack  $\alpha$ , aerofoil lift coefficient  $C_l$  and aerofoil drag coefficient  $C_d$ . These are the reference values when determining the relative derivatives for turn.

Table 4.5: Relevant sustained turn properties.

$V$ [m/s]	$V_S$ [m/s]	$n$	$L$ [N]	$D$ [N]	$R$ [m]
16.795	9.918	2.315	272.129	15.591	13.775
$C_L$	$C_D$	$Re$	$\alpha$ [deg]	$C_l$	$C_d$
1.410	0.081	348526.268	8.230	1.443	0.016

## 4.2 Case 1 - Air Cargo Challenge 2019

### 4.2.1 Problem definition

The aim is to optimise the wing aerofoil used by the team AERO@UBI in the Air Cargo Challenge 2019, so that it maximizes the score for the competition conditions and restrictions.

The competition score is given by Equation 4.1, where  $m_{cargo}$  is the mass in kg of transported cargo,  $t_{flown}$  is the amount of time in seconds to fly 10 laps,  $a$  is a bonus for no parts lost during flight,  $b$  is a bonus for landing on the field,  $c$  is a bonus for landing within 60 meters,  $d$  is either 1 (valid flight) or 0 (invalid flight) and  $Timebonus$  is related to the installation of the payload on the aircraft as stated in the regulation [50].

$$Score = \left( \frac{m_{cargo}}{t_{flown}} \cdot 2000 + a + b + c \right) \cdot d + Timebonus \quad (4.1)$$

Neither  $a$  nor  $Timebonus$  are related to the aerofoil, thus these are disregarded from the Equation, parameters  $b$  and  $c$  depend mostly on the landing gear and field so they may be disregarded, and  $d$  must have a value of 1, that is, it must be a valid flight. A valid flight occurs when the aircraft takes-off within 60 meters and lands without a crash. This results in Equation 4.2.

$$Score = \frac{m_{cargo}}{t_{flown}} \cdot 2000 \quad (4.2)$$

To maximize  $Score$ , the cargo mass (equivalent to payload weight, gravity is assumed constant) must be maximized and time flown must be minimized. These are the operational objectives, which have the same relative influence on the  $Score$ , Equation 4.3.

$$\begin{cases} \delta Score \propto \delta W_{payload} \\ \delta Score \propto -\delta t_{flight} \end{cases} \quad (4.3)$$

As seen in Section 3.4.4, the aerodynamic properties which influence these are  $C_{l,max}$ ,  $C_l$  and  $C_d$  at take-off,  $C_d$  in the turn and  $C_d$  in the cruise, leading to Equation 4.4, where  $w_i$  is determined using Equation 3.56.

$$\begin{cases} \delta Score \propto w_1 \delta C_{l,max,TO} + w_2 \delta C_{l,TO} + w_3 \delta C_{d,TO} \\ \delta Score \propto w_4 \delta C_{d,cruise} + w_5 \delta C_{d,turn} \end{cases} \quad (4.4)$$

In Appendix A the full Equations for all weights calculations are presented. As an example,  $w_1$  is calculated via Equation 4.5, in which each set of derivatives must be determined as well as the ratios of properties.

$$w_1 = -\frac{\partial W_{payload}}{\partial W} \left( \frac{\partial S_G}{\partial W} \right)^{-1} \frac{\partial S_G}{\partial C_{L,max,TO}} \frac{\partial C_{L,max,TO}}{\partial C_{l,max,TO}} \frac{C_{l,max,TO}}{C_{L,max,TO}} \frac{C_{L,max,TO}}{S_G} \frac{S_G}{W} \frac{W}{W_{payload}} \quad (4.5)$$

Since this aircraft was designed using a mission-based multidisciplinary optimisation [54], the flight time is estimated, as is the cargo mass, the wing polars, the distances travelled and the aerofoil polars. Using this data, it is possible to determine all the relevant aerodynamic properties and derivatives near the design solution, leading to the calculation of the weights, using the full equations in Appendix A and data in Section 4.1 and Subsection 4.2.2. The weights and normalised weights  $\bar{w}_i$  utilised for optimisation are available in Table 4.6.

Table 4.6: Values of weights  $w_i$  and normalised weights  $\bar{w}_i$  used during optimisation.

i	1	2	3	4	5
$w_i$	0.54	0.103	-0.06	-0.196	-0.031
$\bar{w}_i$	0.581	0.11	0.065	0.211	0.033

The normalised weights are used by the XOPTFOIL objective function, which for this case results in Equation 4.6, which aggregates the aerodynamic properties  $C_{l,max,TO}$ ,  $C_{l,TO}$ ,  $C_{d,TO}$ ,  $C_{d,cruise}$  and  $C_{d,turn}$  and the penalty value  $\delta$ . A negative value in the weight simply means that it must be minimized while for a positive one, maximized. Note that operating points 3, 4 and 5 have negative weights prior to normalisation, therefore their corresponding properties  $C_{d,TO}$ ,  $C_{d,cruise}$  and  $C_{d,turn}$  are to be minimized. In Equation 4.6 these properties are inverted, the  $w_3$ ,  $w_4$  and  $w_5$  sign change to positive, followed by normalisation resulting in  $\bar{w}$ , present in Table 4.6.

$$Obj = \bar{w}_1 \frac{C_{l,max,TO,ref}}{C_{l,max,TO}} + \bar{w}_2 \frac{C_{l,TO,ref}}{C_{l,TO}} + \bar{w}_3 \frac{C_{d,TO}}{C_{d,TO,ref}} + \bar{w}_4 \frac{C_{d,cruise}}{C_{d,cruise,ref}} + \bar{w}_5 \frac{C_{d,turn}}{C_{d,turn,ref}} + \delta \quad (4.6)$$

with operating points in Table 4.7.

Table 4.7: Operating points for case 1.

Operating Point	1	2	3	4	5
Objective	max $C_{l,max}$	max $C_l$	min $C_d$	min $C_d$	min $C_d$
$\bar{w}$	0.581	0.110	0.065	0.211	0.033
$Re$	160,000	160,000	160,000	571,300	348,500
$\alpha$	8 to 15, step: 1	1.5	1.5	-	-
$C_l$	-	-	-	0.258	1.443
$M$	0.02	0.02	0.02	0.08	0.05
$hinge_x$	0.83	0.83	0.83	0.83	0.83
$defl$	8	8	8	-8	0

subject to the constraints:

1. Lower value of maximum thickness ratio at 0.1, no restriction on upper maximum thickness;
2. Minimum thickness trailing edge angle of 4 deg;
3. Trailing edge thickness ratio of 0.003;
4. Angles' maximum, minimum and difference values of the two points closest to the leading edge, of 89.99, 80.00 and 20.00 degrees, respectively;
5. The maximum angle between any three consecutive points of 25 deg;
6. Number of curvature sign reversals at the upper surface and lower surface of the aerofoil of 4 each;
7. Flap hinge position between 0.7 and 0.9 in  $x/c$  on the lower surface of the aerofoil;

8. Flap deflection between -10 deg and 15 deg.

#### 4.2.2 Relative derivatives - Case 1

In study case 1, the main concern was that there were weights to compare the parametrization methods, meaning the relative derivatives either have little accuracy or are simply incorrect due to human error. The following Tables 4.8 and 4.9 present the used values.

Table 4.8: Used relative derivatives related to take-off for case 1.

$\frac{\partial W_{payload}}{\partial W}$	$\frac{\partial \bar{W}}{\partial \bar{S}_G}$	$\frac{\partial \bar{S}_G}{\partial C_{L,max}}$	$\frac{\partial \bar{S}_G}{\partial C_L}$	$\frac{\partial \bar{S}_G}{\partial C_D}$
1	0.60	-1.0	-0.18	0.2
$\frac{\partial C_{L,max}}{\partial C_{l,max}}$	$\frac{\partial C_L}{\partial C_l}$	$\frac{\partial C_D}{\partial C_d}$		
0.9	0.95	0.5		

Table 4.9: Used relative derivatives related to flight time for case 1.

$\frac{\partial t_{flight}}{\partial V_{cruise}}$	$\frac{\partial t_{flight}}{\partial V_{turn}}$	$\frac{\partial V_{cruise}}{\partial C_{D,cruise}}$	$\frac{\partial V_{turn}}{\partial C_{D,turn}}$	$\frac{\partial C_{D,cruise}}{\partial C_{d,cruise}}$	$\frac{\partial C_{D,turn}}{\partial C_{d,turn}}$
-0.698	-0.302	-0.5	-0.5	0.561	0.204

The actual derivatives are presented in the following Tables 4.10 and 4.11.

Table 4.10: Actual relative derivatives related to take-off for case 1.

$\frac{\partial W_{payload}}{\partial W}$	$\frac{\partial \bar{W}}{\partial \bar{S}_G}$	$\frac{\partial \bar{S}_G}{\partial C_{L,max}}$	$\frac{\partial \bar{S}_G}{\partial C_L}$	$\frac{\partial \bar{S}_G}{\partial C_D}$
1.466	1.590	-1.040	-0.1787	0.1967
$\frac{\partial C_{L,max}}{\partial C_{l,max}}$	$\frac{\partial C_L}{\partial C_l}$	$\frac{\partial C_D}{\partial C_d}$		
1.111	1.052	0.453		

Table 4.11: Actual relative derivatives related to flight time for case 1.

$\frac{\partial t_{flight}}{\partial V_{cruise}}$	$\frac{\partial t_{flight}}{\partial V_{turn}}$	$\frac{\partial V_{cruise}}{\partial C_{D,cruise}}$	$\frac{\partial V_{turn}}{\partial C_{D,turn}}$	$\frac{\partial C_{D,cruise}}{\partial C_{d,cruise}}$	$\frac{\partial C_{D,turn}}{\partial C_{d,turn}}$
-0.720	-0.280	-0.496	-0.496	0.561	0.204

Utilising the actual relative derivatives values would result in the weights presented in Table 4.12. The main reason for using the incorrect values in this work is that for this section the main concerns are the parametrization methods comparison and off design performance. The difference between weights should have a small impact on these results.

Table 4.12: Actual weights for case 1.

i	1	2	3	4	5
$w_i$	1.0655	0.1734	-0.0821	-0.2003	-0.0284
$\bar{w}_i$	0.6876	0.1119	0.0530	0.1292	0.0183



### 4.2.3 Optimisation cases and conditions

In this case study there are several optimisation cases, which are the combination of the parametrization method and number of design variables for parametrization.

Aerofoil optimisation is executed at cases *A*, *B*, and *C* for each parametrization method, except for Bezier-PARSEC 3333 parametrization (BPP). From case *A* to *B*, the number of design variables for surface representation increases from 6 to 12 and from *B* to *C*, 12 to 24. Adding the 4 design variables for the flaps to the aerofoil number of design variables, the total number of design variables for each case is obtained, shown in Table 4.13. BPP has only ten design variables for the aerofoil shape since the trailing edge thickness and position are defined and constant.

There are 4 design variables for the flaps: three deflections, one for each flight condition ( $defl_{TO}, defl_{cruise}, defl_{turn}$ ), and the flap hinge position along the chord ( $hinge_x$ ).

Table 4.13: Total number of design variables used in each optimisation case for each parametrization method.

Case	BSP	CSF	HH	BPP
<i>A</i>	10	10	10	14
<i>B</i>	16	16	16	-
<i>C</i>	28	28	28	-

Additionally, the initial perturbations vary depending on the parametrization, presented in Table 4.14. The values of the initial perturbations were set to allow a comparable initial design space.

Table 4.14: Initial perturbations for each parametrization method.

	BSP	CSF	HH	BPP
$\xi_{abs}$	0.02	0.1	0.1	0.01
$\xi_{rel}$	0.5	0.5	0	0.5

The optimisation constants can be consulted in Table 4.15. While a population size ( $p_{size}$ ) of 40 is not the ideal for this algorithm according to Piotrowski et al. [52], it is expected to perform adequately since Skinner et al. [9] indicates 30 to 40 population size as the most commonly used for aerofoil optimisation.

Table 4.15: Optimisation constants for analysis case 1.

$max_{steps}$	$p_{size}$	$V_{max}$	$c_1$	$c_2$	$w_0$	$w_f$	$w_{rate}$	$\delta_0$	$\delta_f$
500	40	0.025	1.4	1	1.8	0.8	0.02	0.1	0.0001

The maximum number of iterations ( $max_{steps}$ ) of 500 was set in order to allow optimisation until population diversity is low for most cases, indicated by a design radius near 0.005. The penalty limit varies from 0.1 to 0.0001 during optimisation to permit some penalties at the start of the optimisation, meaning that at start penalties have a 10% tolerance. The remaining parameters were already in use for XOPTFOIL.

The values used for XFOIL panelling are in Table 4.16, XFOIL analysis used 200 maximum iterations for VISCAL and an acceleration parameter of 0.001. The initialization sequence parameters can be found in Table 4.17, a sinusoidal distribution was employed.

Table 4.16: XFOIL panelling variables

NPAN	CVPAR	CTERAT	CTRRAT	XSREF1	XSREF2	XPREF1	XPREF2
200	1.00	0.15	0.20	1.00	1.00	1.00	1.00

Table 4.17: XFOIL initialization analysis parameters.

$n_{init}$	$\alpha_{0,init}$	$C_{l,0,init}$	$(p_{0,init})$
5	2.0	0.5	0.7

#### 4.2.4 Results and discussion

The resulting aerofoils are shown in Figure 4.2 along with the original aerofoil. The trend shows a preference for a higher maximum thickness nearer the leading edge and reduction in thickness on the lower surface, which in turn increases the maximum camber of the aerofoils. Table 4.18 presents these properties. In BSP case  $C$ , CSF case  $C$  and HH case  $C$  several curvature reversals are visible and significantly impact the aerofoil geometry. This is possibly due to a higher number of design variables in these cases. Nonetheless, other cases also exhibit a higher number of curvature reversals when compared to the original aerofoil, it is expected more restrictive optimisation constraints would reduce these.

Table 4.18: Resulting aerofoil properties for each study case.

Case	$Thickness_{max}$	$x_{Thickness,max}$	$Camber_{max}$	$x_{Camber,max}$
Original	0.13	0.242	0.06	0.528
BSP case $A$	0.159	0.287	0.071	0.48
BSP case $B$	0.136	0.218	0.07	0.543
BSP case $C$	0.134	0.198	0.068	0.598
CSF case $A$	0.118	0.194	0.066	0.519
CSF case $B$	0.145	0.222	0.079	0.499
CSF case $C$	0.139	0.215	0.069	0.456
HH case $A$	0.125	0.215	0.068	0.493
HH case $B$	0.142	0.221	0.077	0.463
HH case $C$	0.135	0.201	0.079	0.51
BPP case $A$	0.148	0.227	0.07	0.529

The design variables density distribution from the first iteration up to the one-hundredth are shown in Figure 4.3. As previously mentioned, the initial perturbation parameters control

this variation, naturally the higher concentrations are located near local minimums of  $Obj$ .

For the BPP case  $A$ ,  $D1$  to  $D5$  on thickness surface correspond to leading edge radius, maximum thickness value, position and curvature and trailing edge angle in rad, respectively, while  $D1$  to  $D5$  on camber surface correspond to leading edge angle, maximum camber value, position and curvature and trailing edge angle in rad, respectively.

The design variables variation decreases with iterations and presents the same behaviour of the design radius, per definition. The design radius for all iterations is presented in Figure 4.4. It shows CSF case  $A$  and BPP case  $A$  solutions have a very high design radius, 0.0199 and 0.0517 respectively. Meaning that 500 iterations were insufficient to reduce the diversity of the population. However, the design radius has not presented a significant variation since iteration 60 or 70 thus the number of iterations would be significantly higher than 500 to reduce the design radius by an order of magnitude.

The count of optimisation aerofoil evaluation types is presented in Table 4.19. An aerofoil evaluation types is determined by the kind of exit from the aerofoil evaluation. The exceptions mentioned in Section 3.4.1 are most of the aerofoil evaluation types, the only exception being *Conv*, when XFOIL solution has converged and the objective function is returned as the evaluation. *Thick*, *TEAngle*, *LEAngles*, *Curv*, *PAngle*, *Nonconv* refer to exceptions due to the penalties aerofoil thickness, trailing edge angle, leading edge angle, curvature reversals, panel angles and non convergence of the XFOIL analysis, respectively.

Table 4.19: Count of the optimisation evaluation type for each optimisation case.

Case	<i>Thick</i>	<i>TEAngle</i>	<i>LEAngles</i>	<i>Curv</i>	<i>PAngle</i>	<i>Non conv</i>	<i>Conv</i>
BSP case $A$	216	989	15	0	4	2058	16718
BSP case $B$	244	990	72	0	4	726	17964
BSP case $C$	525	2430	110	1267	0	749	14919
CSF case $A$	271	2911	0	0	7	368	16443
CSF case $B$	348	1371	0	0	0	1206	17075
CSF case $C$	195	517	0	1	0	395	18892
HH case $A$	186	1157	4	49	42	237	18325
HH case $B$	380	1567	6	148	39	602	17258
HH case $C$	409	1968	23	228	8	332	17032
BPP case $A$	6988	8	0	0	352	460	12192

The higher count of *Thick* in BPP case  $A$  occurs because while the design variables have constraints for this case, the tool does not check them until it tries to generate the aerofoil. If an invalid set of design variables is given, the returned aerofoil has no thickness nor camber, triggering the condition.

For the same optimisation type, the number of *TEAngle* increases with the number of design variables, which is to be expected. The CSF is the exception to this behaviour. This is explained by the use of Bernstein polynomials in this parametrization which limits local

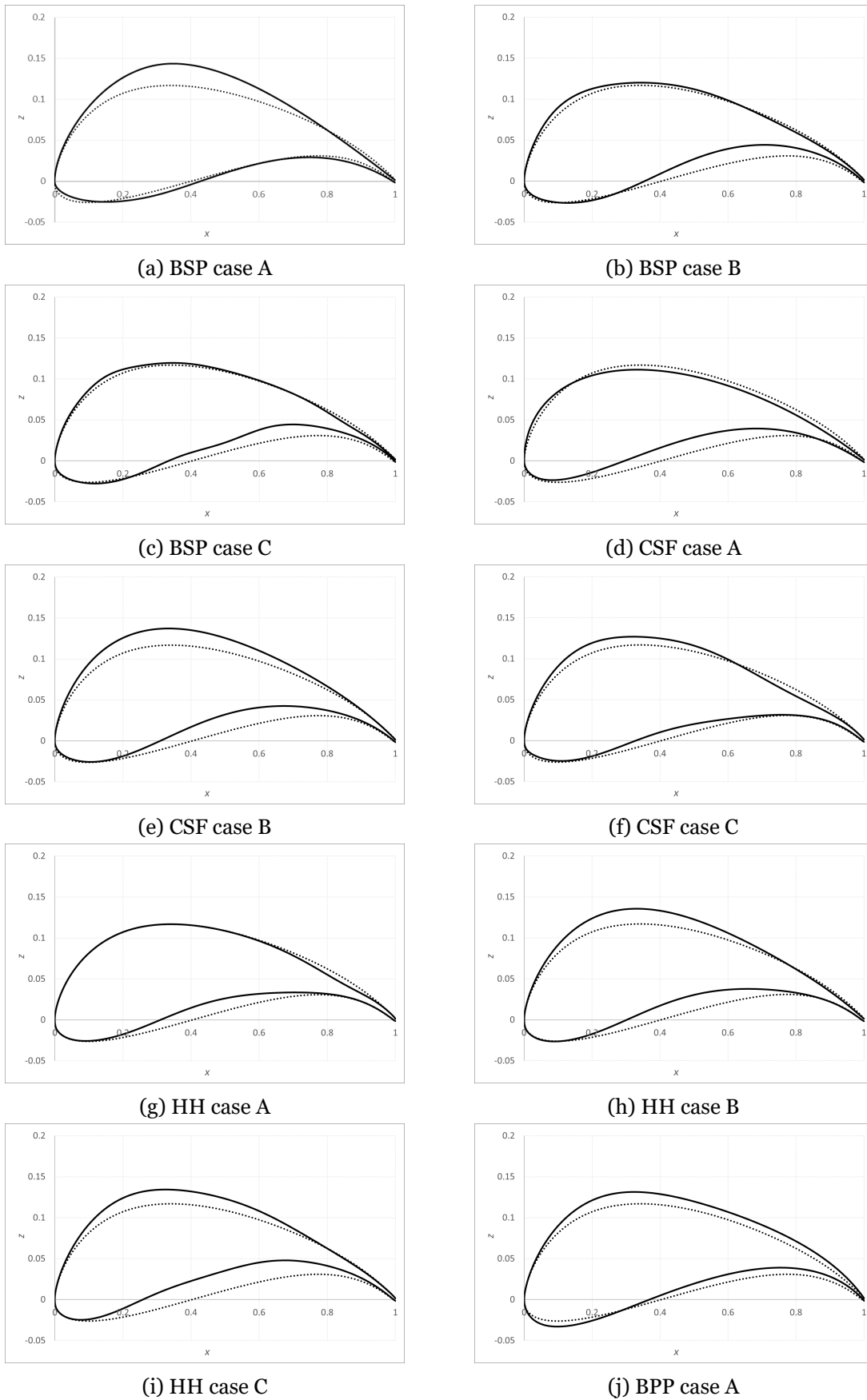
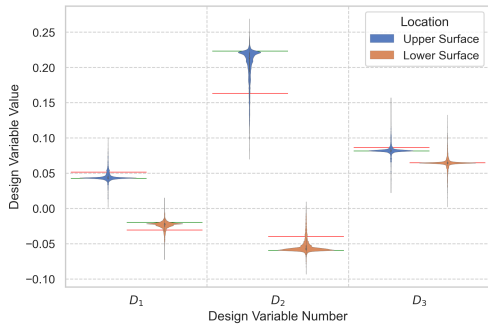
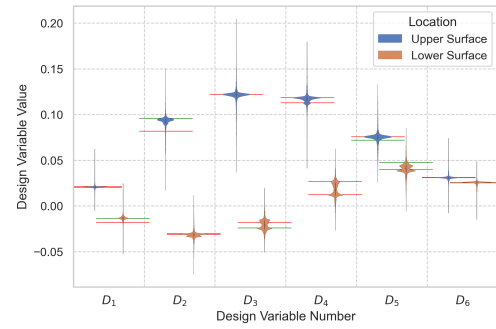


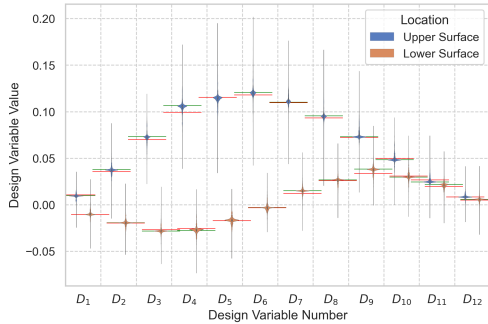
Figure 4.2: Optimised aerofoils (solid line) and original aerofoil (dashed line) for all study cases.



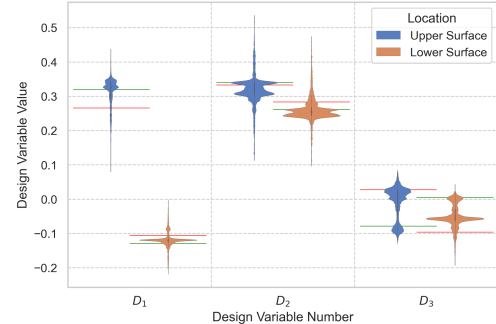
(a) BSP case A



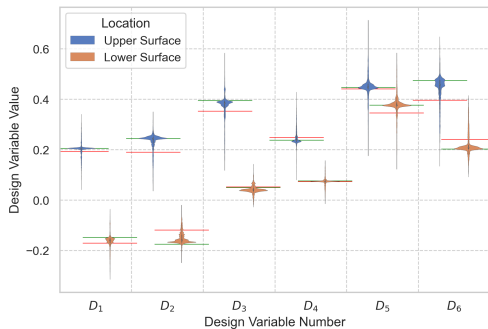
(b) BSP case B



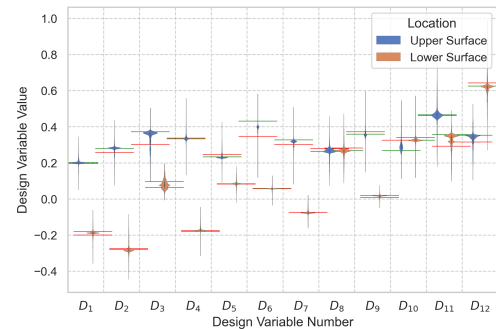
(c) BSP case C



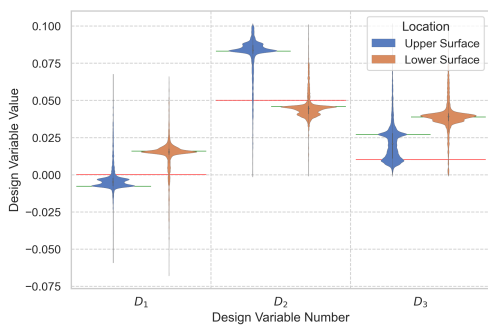
(d) CSF case A



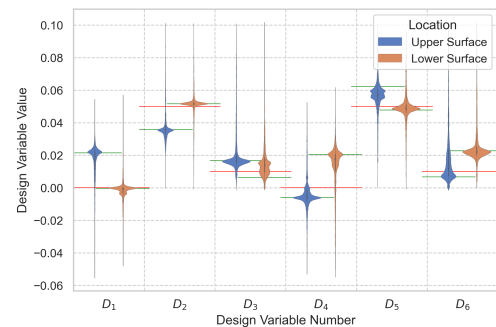
(e) CSF case B



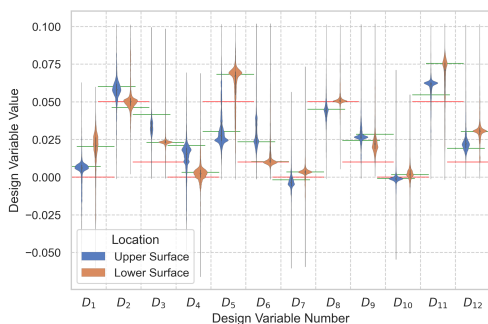
(f) CSF case C



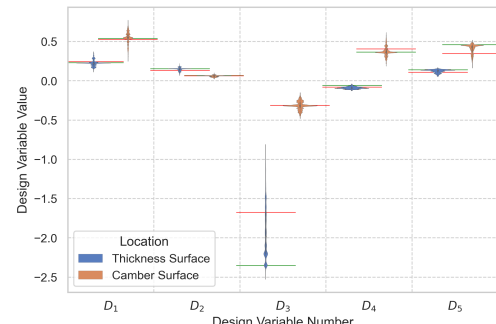
(g) HH case A



(h) HH case B



(i) HH case C



(j) BPP case A

Figure 4.3: Violin graph of all design variables up to iteration 100. Red line marks initial variables and green line the best design variables at iteration 100.

changes on the aerofoil and trailing edge. This also explains the lower number of  $C_{urv}$  for CSF.

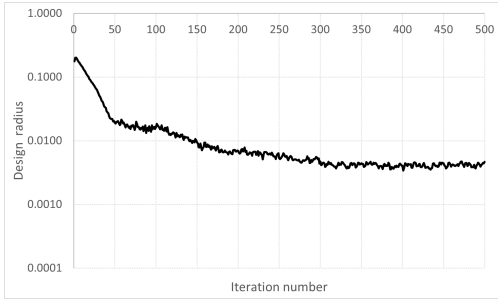
The resulting flap design variables are shown in Table 4.20. In almost all cases the flap deflection during cruise is at the constraint minimum. This shows that if that constraint was altered it may have been possible to decrease the drag coefficient. The exception is the BPP case A, which increased the deflection when compared to the initial condition, probably due to an insufficient number of iterations. This is supported by the relative high design radius in Figure 4.4.

Table 4.20: Resulting flap design variables.

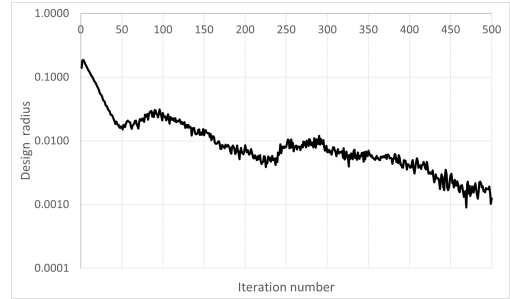
Case	$defl_{TO}$	$defl_{cruise}$	$defl_{turn}$	$hinge_x$
Original	8	-8	0	0.83
BSP case A	14.53	-10	2.45	0.817
BSP case B	10.88	-9.98	2.42	0.834
BSP case C	9.92	-9.75	1.53	0.855
CSF case A	13.4	-9.96	1.45	0.863
CSF case B	10.68	-9.97	0.11	0.809
CSF case C	11.48	-10	1.41	0.798
HH case A	12.36	-10	-0.01	0.833
HH case B	12.51	-10	-3.93	0.807
HH case C	8.83	-9.99	-0.36	0.799
BPP case A	10.05	-1.99	-4.64	0.802

The aerodynamic properties of the resulting aerofoils are shown in Table 4.21, as well as the objective function ( $Obj$ ) and an indicator of the improvement over the original aerofoil ( $1 - Obj$ ). The aerodynamic properties consistently improved are the maximum lift coefficient and lift coefficient during take-off which together account for almost seventy percent of the objective function weights. It is only natural these are properties the optimisation algorithm focused on.

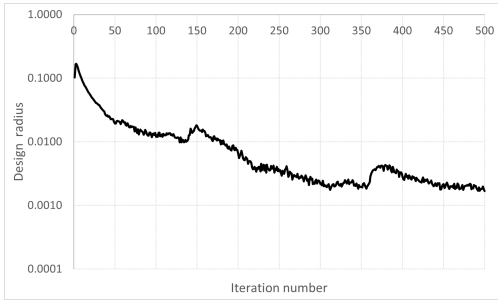
The parametrization method with the lowest value of the objective function is the B-Spline parametrization for all cases. The Class Shape Function and Hicks-Henne have similar results and the Bezier-PARSEC parametrization has the lowest improvement of all.



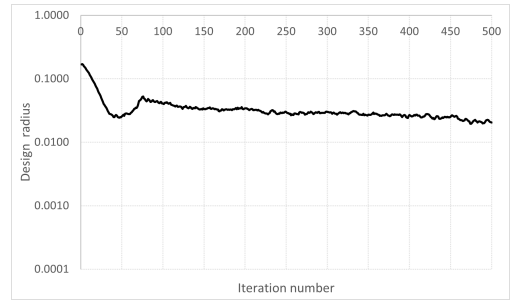
(a) BSP case A



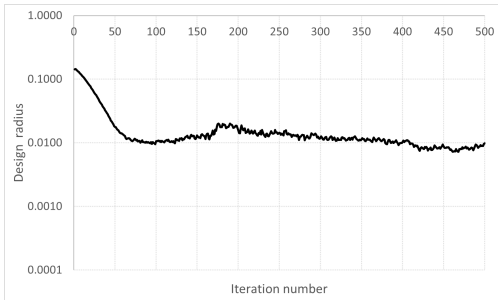
(b) BSP case B



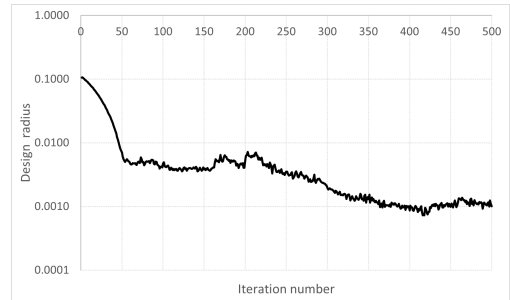
(c) BSP case C



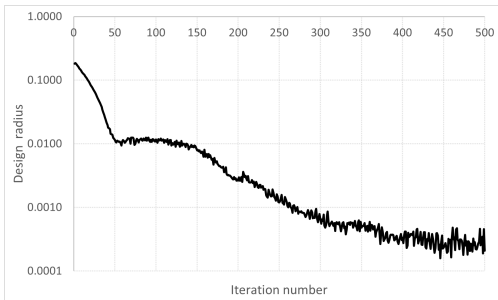
(d) CSF case A



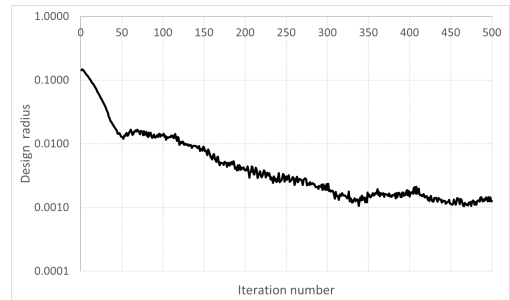
(e) CSF case B



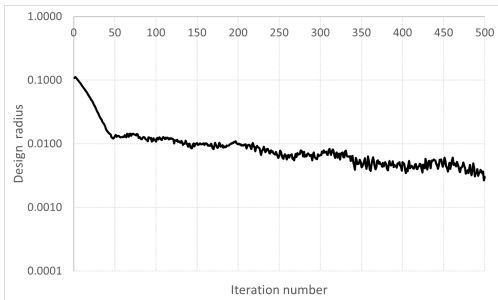
(f) CSF case C



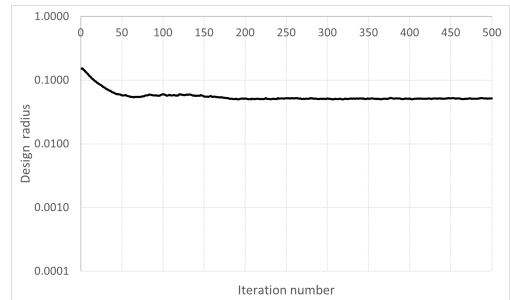
(g) HH case A



(h) HH case B



(i) HH case C



(j) BPP case A

Figure 4.4: Design radius during optimisation for all study cases.

Table 4.21: Aerodynamic properties for the resulting aerofoil of each study case.

Case	$C_{l,max,TO}$	$C_{l,TO}$	$C_{d,TO}$	$C_{d,cruise}$	$C_{d,turn}$	$Obj$	$1 - Obj$
Original	1.993	1.328	0.0183	0.0090	0.0150	1.0000	0.00%
BSP case A	2.244	1.680	0.0263	0.0094	0.0153	0.9509	4.91%
BSP case B	2.221	1.488	0.0218	0.0090	0.0165	0.9447	5.53%
BSP case C	2.234	1.455	0.0201	0.0086	0.0172	0.9312	6.88%
CSF case A	2.037	1.468	0.0200	0.0089	0.0149	0.9809	1.91%
CSF case B	2.258	1.602	0.0242	0.0097	0.0152	0.9512	4.88%
CSF case C	2.252	1.570	0.0215	0.0095	0.0153	0.9418	5.82%
HH case A	2.046	1.512	0.0195	0.0088	0.0139	0.9699	3.01%
HH case B	2.273	1.634	0.0244	0.0098	0.0149	0.9493	5.07%
HH case C	2.284	1.545	0.0214	0.0098	0.0152	0.9409	5.91%
BPP case A	2.246	1.509	0.0264	0.0103	0.0154	0.9823	1.77%

The correlation coefficient between  $Obj$  and the number of design variables for BSP, CSF and HH are 0.9996, 0.7857 and 0.8274 respectively. While the number of design variables correlates with how much optimisation occurs, it is unclear which effect has a higher influence: the greater original aerofoil parametrization accuracy or a more diverse design space.

Table 4.22: Accuracy of the parametrized original aerofoil.

Case	$RMSE_{upper}$	$RMSE_{lower}$
BSP case A	$2.21 \times 10^{-3}$	$1.79 \times 10^{-3}$
BSP case B	$1.24 \times 10^{-4}$	$3.35 \times 10^{-4}$
BSP case C	$2.41 \times 10^{-5}$	$6.04 \times 10^{-5}$
CSF case A	$2.49 \times 10^{-3}$	$2.13 \times 10^{-3}$
CSF case B	$7.64 \times 10^{-5}$	$2.49 \times 10^{-4}$
CSF case C	$3.57 \times 10^{-5}$	$6.30 \times 10^{-5}$
HH case A	0	0
HH case B	0	0
HH case C	0	0
BPP case A	$4.64 \times 10^{-3}$	$4.27 \times 10^{-3}$

A higher number of design variables increases the design space according to Masters et al. [32] and increases the accuracy of the parametrized original aerofoil, Table 4.22, which is used to initialize the optimisation. Table 4.23 presents the relevant aerodynamic properties for the initial aerofoil and the initial objective value  $Obj_0$  for each case. For BSP and CSF,  $Obj_0$  correlates with  $Obj$ , with correlation coefficient of 0.739 and 0.966, it appears that for CSF the aerofoil accuracy is a higher factor than for BSP. Notice that for HH only the design space is influenced by the number of design variables.

Since the initial optimisation aerofoil is not the original aerofoil, each case starts at a different point of optimisation  $Obj_0$ .

Referring to Table 4.21, the BSP case C has the lowest value of  $Obj$ , with a  $C_{l,max,TO}$  of 2.234, 12% higher than the original aerofoil, and a  $C_{d,cruise}$  of 0.0086, 3% lower. To evaluate



Table 4.23: Relevant aerodynamic properties for the initial aerofoil and its initial objective value for each case.

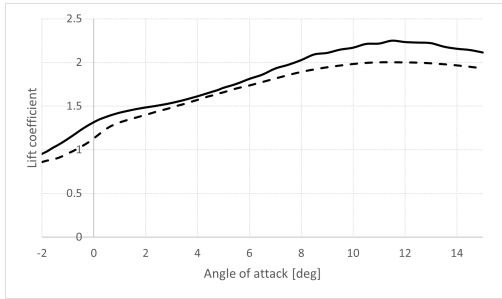
Case	$C_{l,max,TO}$	$C_{l,TO}$	$C_{d,TO}$	$C_{d,cruise}$	$C_{d,turn}$	$Obj_0$
Original	1.993	1.328	0.0183	0.0090	0.0150	1.000
BSP case A	1.836	1.353	0.0173	0.0086	0.0133	1.032
BSP case B	1.932	1.334	0.0184	0.0092	0.0149	1.023
BSP case C	1.927	1.329	0.0183	0.0090	0.0150	1.020
CSF case A	1.868	1.336	0.0179	0.0086	0.0133	1.023
CSF case B	2.003	1.339	0.0184	0.0092	0.0147	1.001
CSF case C	1.993	1.328	0.0183	0.0090	0.0150	1.000
HH case A	1.992	1.330	0.0183	0.0090	0.0149	1.002
HH case B	1.992	1.330	0.0183	0.0090	0.0149	1.002
HH case C	1.992	1.330	0.0183	0.0090	0.0149	1.002
BPP case A	2.035	1.354	0.0236	0.0111	0.0173	1.061

the aerofoil off-design performance, polars for each operating condition were calculated, as shown in Figure 4.5. The operating conditions are shown in Table 4.24. Note that the original aerofoil refers to the aerofoil at the start of optimization for BSP case C with flap deflection of 8.0, -8.0 and 0.0 degrees for take-off, cruise and turn respectively with flap hinge at 0.83, while BSP case C final aerofoil has flap deflections of 9.92, -9.75 and 1.53 degrees with flap hinge at 0.855. Flap hinge is located on the aerofoil lower surface.

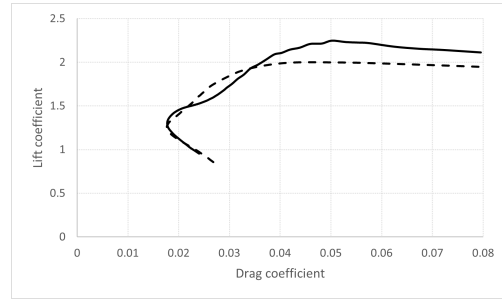
Table 4.24: Off-design conditions.

Case	$Re$	$Re\sqrt{C_l}$	$M$	$M\sqrt{C_l}$
Take-off	160,000	-	0.02	-
Cruise	-	290,000	-	0.04
Turn	-	420,000	-	0.06

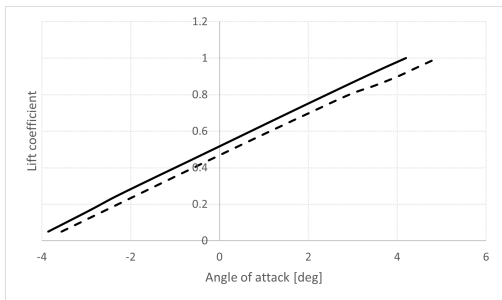
As expected, the improved aerodynamic characteristics are concentrated near the operating points. This is observed for take-off for operating points 2 and 3, where there is a lift coefficient increase and drag reduction near the angle of attack of 1.5 deg, Figures 4.5a and 4.5b. Also, for operating point 4, there is a significant drag coefficient reduction near the lift coefficient of 0.258 is observed, Figures 4.5c and 4.5d. However, there is no improvement in the drag coefficient for operating point 5, lift coefficient of 1.443, Figures 4.5e and 4.5f. This shows that from the optimisation results an aerofoil with better aerodynamic performance only near the optimisation points.



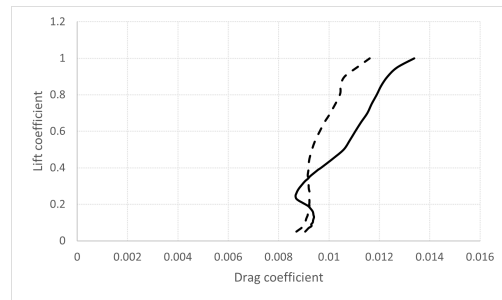
(a) Lift coefficient for take-off



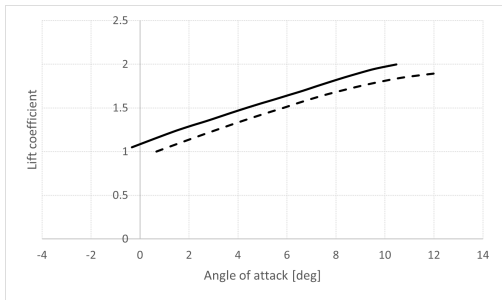
(b) Drag polar for take-off



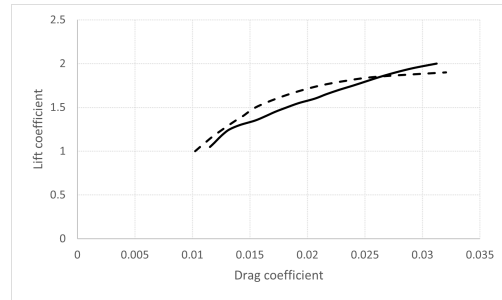
(c) Lift coefficient for cruise



(d) Drag polar for cruise



(e) Lift coefficient for turn



(f) Drag polar for turn

Figure 4.5: BSP case *C* polars (solid lines) and original aerofoil polars (dashed lines) for each operating condition near the operating point.

## 4.3 Case 2 - Air Cargo Challenge 2022

### 4.3.1 Problem definition

The objective is to optimise the wing aerofoil of the aircraft from AERO@UBI, which participated on the 2019 edition, for the up coming 2022 edition score formula.

Comparing to 2019, in the 2022 edition [51] several relevant changes have been made:

- Flight performance is directly relative to other teams performance;
- Flight performance now depends on:
  - Payload transported during the flight;
  - Distance flown during 120 seconds;
  - Altitude reached within 60 seconds after take-off.
- Flight course is now free, however it must be above 10 meters and under 120 meters;
- Take-off distance within 40 meters gives a bonus to performance and it must be within 60 meters.
- A limiting box was introduced, which would not allow the 2019 aircraft to compete.

While the aircraft may not be able to compete, the aerofoil can still be optimised and the methodology can be applied to other aircraft.

The competition points are given by Equation 4.7, with  $S_{payload}$ ,  $S_{distance}$  and  $S_{altitude}$  being the partial score for payload, distance and altitude,  $B_1$ ,  $B_2$  and  $B_3$  are bonus points for loading time, unloading time and payload prediction,  $B_{take-off}$  is a factor depending on take-off distance and  $P_{flight}$  is a penalty for when altitude limits are not respected or parts are lost.

$$Score = \left( \frac{S_{payload} + S_{distance} + S_{altitude}}{3} + B_1 + B_2 + B_3 \right) \cdot B_{take-off} \cdot P_{flight} \quad (4.7)$$

$B_1$ ,  $B_2$ ,  $B_3$  and  $P_{flight}$  do not depend on the aircraft flight performance, leaving Equation 4.8 as the one of interest for aerofoil design.

$$Score = \left( \frac{S_{payload} + S_{distance} + S_{altitude}}{3} \right) \cdot B_{take-off} \quad (4.8)$$

where the partial scores are determined by Equation 4.9. In which  $W_{max,other}$ ,  $\hat{S}_{max,other}$  and  $PS_{altitude,max,other}$  are the maximum payload weight flown, the flight distance and the altitude pre-score by any team.

$$\begin{cases} S_{payload} &= 1000 \frac{W}{W_{max,other}} \\ S_{distance} &= 1000 \frac{\hat{S}}{\hat{S}_{max,other}} \\ S_{altitude} &= 1000 \frac{PS_{altitude}}{PS_{altitude,max,other}} \end{cases} \quad (4.9)$$

The altitude pre-score is given by Equation 4.10. Notice that the pre-score maximum occurs near an altitude of 100 m.

$$PS_{altitude} = -3.92 \times 10^{-5} h_{60s}^4 + 1.08 \times 10^{-2} h_{60s}^3 - 1.156 h_{60s}^2 + 64.2 h_{60s} - 537 \quad (4.10)$$

The take-off factor is calculated via Equation 4.11.

$$\begin{cases} B_{take-off} &= 0 \text{ if } S_G > 60 \\ B_{take-off} &= 1 \text{ if } 40 < S_G \leq 60 \\ B_{take-off} &= 1.1 \text{ if } S_G \leq 40 \end{cases} \quad (4.11)$$

Maximizing *Score* means maximizing payload weight, flight distance within 120 s and altitude within 60 s. These operational objectives are assumed to have the same influence on the *Score*, Equation 4.12.

$$\begin{cases} \delta Score \propto \delta W_{payload} \\ \delta Score \propto \delta \hat{S}_{flight} \\ \delta Score \propto \delta h_{60s} \end{cases} \quad (4.12)$$

In Section 3.4.4 the aerodynamic properties which influence these have been identified,  $C_{l,max}$ ,  $C_l$  and  $C_d$  at take-off,  $C_d$  in the turn,  $C_d$  in the cruise and  $C_l$  and  $C_d$  during climb, leading to Equation 4.13, where  $w_i$  is determined using Equation 3.56.

$$\begin{aligned} \delta Score \propto & w_1 \delta C_{l,max,TO} + w_2 \delta C_{l,TO} + w_3 \delta C_{d,TO} \\ & + w_4 \delta C_{d,cruise} + w_5 \delta C_{d,turn} + w_6 \delta C_{l,climb} + w_7 \delta C_{d,climb} \end{aligned} \quad (4.13)$$

As explained in analysis case 1, this aircraft was designed using a mission-based multidisciplinary optimisation [54]. With the full Equations in Appendix A and data in Section 4.1 and Subsection 4.3.2 it is possible to determine the weights and normalised weights  $\bar{w}_i$  required for optimisation, Table 4.25.

Table 4.25: Values of weights  $w_i$  and normalised weights  $\bar{w}_i$  used during optimisation for case 2.

i	1	2	3	4	5	6	7
$w_i$	0.2137	0.0348	-0.0165	-0.2003	-0.0284	0.1678	-0.1690
$\bar{w}_i$	0.2573	0.0419	0.0198	0.2412	0.0342	0.2021	0.2036

s The normalised weights are utilised by the XOPTFOIL objective function, which for this case results in Equation 4.14, which aggregates the aerodynamic properties  $C_{l,max,TO}$ ,  $C_{l,TO}$ ,  $C_{d,TO}$ ,  $C_{d,cruise}$ ,  $C_{d,turn}$ ,  $C_{l,climb}$  and  $C_{d,climb}$  and the penalty value  $\delta$ . In this case operating points 3, 4, 5 and 7 have negative  $w$  therefore  $C_{d,TO}$ ,  $C_{d,cruise}$ ,  $C_{d,turn}$  and  $C_{d,climb}$  are to be minimized, leading to inversion in Equation 4.14. Note that once inverted, the negative sign is negated allowing for normalisation in  $\bar{w}$ .

$$\begin{aligned}
 Obj = & \bar{w}_1 \frac{C_{l,max,TO,ref}}{C_{l,max,TO}} + \bar{w}_2 \frac{C_{l,TO,ref}}{C_{l,TO}} + \bar{w}_3 \frac{C_{d,TO}}{C_{d,TO,ref}} + \bar{w}_4 \frac{C_{d,cruise}}{C_{d,cruise,ref}} + \bar{w}_5 \frac{C_{d,turn}}{C_{d,turn,ref}} \\
 & + \bar{w}_6 \frac{C_{l,climb,ref}}{C_{l,climb}} + \bar{w}_7 \frac{C_{d,v}}{C_{d,climb,ref}} + \delta
 \end{aligned} \quad (4.14)$$

with operating points in Table 4.26.

Table 4.26: Operating points for case 2.

Operating Point	1	2	3	4	5	6	7
Objective	max $C_{l,max}$	max $C_l$	min $C_d$	min $C_d$	min $C_d$	max $C_l$	min $C_d$
$\hat{w}$	0.2573	0.0419	0.0198	0.2412	0.0342	0.2021	0.2036
$Re$	160,000	160,000	160,000	571,300	348,500	252,100	252,100
$\alpha$	8 to 17, step:1	1.5	1.5	-	-	5.0	5.0
$C_l$	-	-	-	0.258	1.443	-	-
$M$	0.02	0.02	0.02	0.08	0.05	0.04	0.04
$hinge_x$	0.83	0.83	0.83	0.83	0.83	0.83	0.83
$defl$	8	8	8	-8	0	0	0

subject to the constraints:

1. Lower value of maximum thickness at 0.1, no restriction on upper maximum thickness;
2. Minimum thickness trailing edge angle of 4 deg after 0.8 in  $x/c$ ;
3. Trailing edge thickness of 0.003;
4. Angles' maximum, minimum and difference values of the two points closest to the leading edge, of 89.99, 80.00 and 20.00 degrees, respectively;

5. The maximum angle between any three consecutive points of 25 deg;
6. The maximum distance ratio between two panels being up to 10 times the maximum on the initial aerofoil;
7. Number of curvature sign reversals at the upper surface and lower surface of the aerofoil of 3 each, with 0.1 being the threshold for curvature reversal;
8. Flap hinge position between 0.7 and 0.9 in  $x$  on the lower surface of the aerofoil;
9. Flap deflection between -10 deg and 15 deg.

#### 4.3.2 Relative derivatives - Case 2

In case 2 the derivatives were determined again, the obtained values are presented in the following Tables 4.27, 4.28 and 4.29.

Table 4.27: Relative derivatives related to take-off.

$\frac{\partial \overline{W}_{payload}}{\partial \overline{W}}$	$\frac{\partial \overline{W}}{\partial \overline{S}_G}$	$\frac{\partial \overline{S}_G}{\partial \overline{C}_{L,max}}$	$\frac{\partial \overline{S}_G}{\partial \overline{C}_L}$	$\frac{\partial \overline{S}_G}{\partial \overline{C}_D}$
1.466	1.590	-1.040	-0.1787	0.1967
$\frac{\partial \overline{C}_{L,max}}{\partial \overline{C}_{l,max}}$	$\frac{\partial \overline{C}_L}{\partial \overline{C}_l}$	$\frac{\partial \overline{C}_D}{\partial \overline{C}_d}$		
1.111	1.052	0.453		

Table 4.28: Relative derivatives related to climb.

$\frac{\partial \overline{V}_V}{\partial \overline{C}_L}$	$\frac{\partial \overline{V}_V}{\partial \overline{C}_D}$	$\frac{\partial \overline{V}_V}{\partial \overline{W}}$	$\frac{\partial \overline{C}_L}{\partial \overline{C}_l}$	$\frac{\partial \overline{C}_D}{\partial \overline{C}_d}$
0.173	-0.679	-1.172	0.971	0.249

Table 4.29: Relative derivatives related to flight distance.

$\frac{\partial \overline{S}_{flight}}{\partial \overline{V}_{cruise}}$	$\frac{\partial \overline{S}_{flight}}{\partial \overline{V}_{turn}}$	$\frac{\partial \overline{V}_{cruise}}{\partial \overline{C}_{D,cruise}}$	$\frac{\partial \overline{V}_{turn}}{\partial \overline{C}_{D,turn}}$	$\frac{\partial \overline{C}_{D,cruise}}{\partial \overline{C}_{d,cruise}}$	$\frac{\partial \overline{C}_{D,turn}}{\partial \overline{C}_{d,turn}}$
0.720	0.280	-0.496	-0.496	0.561	0.204

#### 4.3.3 Optimisation case and conditions

discretization For the current analysis, a single optimisation case is under scrutiny. Based on the BSP case  $C$  from analysis 1, the highest performing case. The parametrization method in use is BSP, with 24 variables for parametrization and 5 for the flap. The flap variables are the deflection for take-off  $defl_{TO}$ , cruise  $defl_{cruise}$ , turn  $defl_{turn}$  and climb  $defl_{climb}$ , and the flap hinge position along the chord ( $hinge_x$ ).

The optimisation constants can be consulted in Table 4.30. Relative to analysis case 1, the maximum number of iterations has been increased to 1000, which should allow the convergence stop condition to trigger and the initial penalty limit has been increased to 0.5, in order to permit even greater design variety.

Table 4.30: Optimisation constants for analysis case 2.

$max_{steps}$	$p_{size}$	$V_{max}$	$c_1$	$c_2$	$w_0$	$w_f$	$w_{rate}$	$\delta_0$	$\delta_f$	$\xi_{abs}$	$\xi_{rel}$	$tol_{lift}$	$tol_{drag}$
1000	40	0.025	1.4	1	1.8	0.8	0.02	0.5	0.0001	0.02	0.5	0.005	0.005

The values used for XFOIL panelling are in Table 4.31, XFOIL analysis used 200 maximum iterations for VISCAL and an acceleration parameter of 0.001. The initialization sequence parameters can be found in Table 4.32, a sinusoidal distribution was employed.

Table 4.31: XFOIL panelling variables

NPAN	CVPAR	CTERAT	CTRRAT	XSREF1	XSREF2	XPREF1	XPREF2
200	1.00	0.15	0.20	1.00	1.00	1.00	1.00

Table 4.32: XFOIL initialization analysis parameters.

$n_{init}$	$\alpha_{0,init}$	$C_{l,0,init}$	$(p_{0,init})$
10	5.0	0.7	0.5

#### 4.3.4 Results and discussion

The aerofoil optimisation stopped at the maximum number of iterations, with a solution objective of 0.92779 and a design radius of 0.00318. The resulting aerofoil is presented in Figure 4.6, with properties shown in Table 4.33. While the aerofoil surfaces have been changed, the majority of the characteristics did not, particularly minimum thickness  $th_{min}$ , maximum thickness  $th_{max}$ , the leading edge angle maximum, minimum and difference  $LE_{angle,max}$ ,  $LE_{angle,min}$  and  $LE_{angle,dif}$ , maximum panel angle  $PAN_{angle}$  and number of curvature reversals in the lower surface  $Curv_{rev,lower}$ .

The most significant aerofoil modifications have occurred between 0.4 and 0.6 x/c, where both surfaces positions were moved upwards, which increased the aerofoil maximum camber  $cb_{max}$ , and 0.8 and 0.9 x/c where the upper surface is significantly lower relative to the lower surface. This has reduced the aerofoil thickness in the region and, thus, the trailing edge thickness angle  $TE_{th,angle}$ . Additionally it increased the number of curvature reversals on the upper surface  $Curv_{rev,upper}$ .

Table 4.33: Resulting aerofoil properties.

Aerofoil	$th_{min}$	$th_{max}$	$TE_{th,angle}$	$cb_{max}$	$LE_{angle,max}$	$LE_{angle,min}$
Original	0.00286	0.1303	6.51	0.0602	89.76	87.88
Final	0.00236	0.1292	4.00	0.0650	89.62	87.90
Aerofoil	$LE_{angle,dif}$	$Curv_{rev,upper}$	$Curv_{rev,lower}$	$PAN_{angle}$	$GrowthRate_{max}$	$N_{non\ conv}$
Original	1.877	0	1	7.39	9.74	0
Final	1.721	2	1	7.81	14.38	0

The final flap design, presented in Table 4.34, has a hinge located nearer the trailing edge

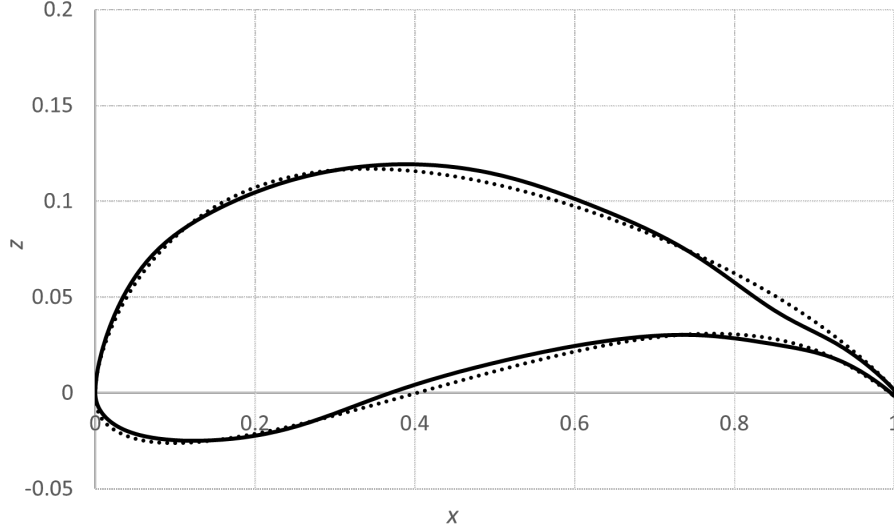


Figure 4.6: Optimised aerofoil (solid line) and original aerofoil (dashed line) for case study 2.

with similar deflections during turn and climb to the original. The minimum flap deflection is used for cruise, which suggests there may have been possible to obtain a lower drag coefficient if the minimum was lower. In take-off the flap deflection is significantly higher than the original and case 1 BSP case *C*. Interestingly the corresponding case 1 has a higher lift coefficient for take-off with a lower deflection and similar hinge position.

Table 4.34: Resulting flap design variables.

Aerofoil	$defl_{TO}$	$defl_{cruise}$	$defl_{turn}$	$defl_{climb}$	$hinge_x$
Original	8.00	-8.00	0.00	0.00	0.830
Final	13.67	-10.00	0.01	0.61	0.860

Table 4.35 presents the final aerodynamic coefficients for the relevant conditions, the objective function value  $Obj$ , the total improvement over the original aerofoil  $1 - Obj$  and the partial improvement per operating point  $1 - Obj_p$ . Based on the respective objective (maximum lift coefficient or minimum drag coefficient) almost all coefficients show an improvement, the only exception being the drag coefficient for take-off. Given that the  $C_{l,TO}$ ,  $C_{d,TO}$  and  $C_{d,turn}$  have the lowest weights, it was expected that these could be detrimental to  $Obj$ . Despite their weight  $C_{l,TO}$  and  $C_{d,turn}$  contribute 1.165% to  $1 - Obj$ , 16.1% of the total improvement.  $C_{d,climb}$  has the greatest contribution with 2.380%. With the current value of  $Obj$ ,  $Score$  is estimated to increase by 6.46%.

Table 4.35: Aerodynamic properties for the resulting aerofoil.

Aerofoil	$C_{l,max,TO}$	$C_{l,TO}$	$C_{d,TO}$	$C_{d,cruise}$	$C_{d,turn}$	$C_{l,climb}$	$C_{d,climb}$	$Obj$	$1 - Obj$
Original	1.999	1.345	0.01874	0.00916	0.01484	1.411	0.01577	1.0000	0.00%
Final	2.118	1.540	0.02006	0.00863	0.01209	1.483	0.01393	0.9278	7.22%
$1 - Obj_p$	1.437%	0.530%	-0.140%	1.400%	0.635%	0.981%	2.380%	-	-



Figure 4.7 shows the design radius and the solution objective during the optimisation. The design radius starts by increasing during the first 3 iterations, mainly because many of the design variables are not constrained and possess random velocities. The initial aerofoil remains as the global best until iteration 26 meaning the solution *Obj* is constant. From iterations 3 to 26 the design radius decreases rapidly because all particles move towards the global best, which currently is the initial aerofoil.

Most of the solution *Obj* variation happens between iteration 26 and 400, 0.99781 to 0.92874. From iteration 400 onwards, the solution *Obj* changes very slightly until 0.92779.

Regarding the design radius, it either decreases or oscillates around some value. Between iteration 200 to 340 it oscillates near 0.013 and from 580 onwards it oscillates around 0.003. In all the remaining intervals, 26 to 200 and 340 to 580, it generalisably decreases.

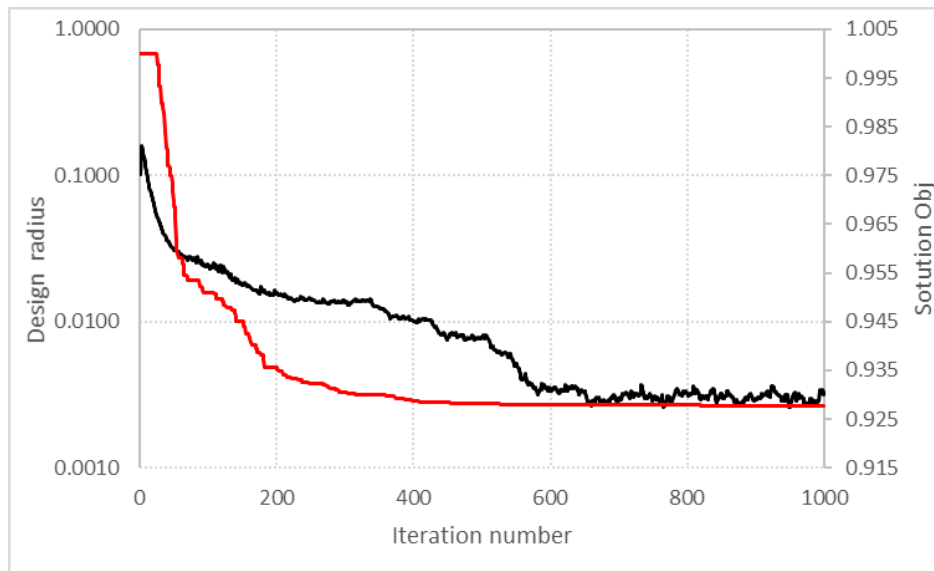


Figure 4.7: Solution objective function value in red and design radius in black during optimisation.

Figure 4.8 presents the type of aerofoil evaluation for each iteration. *Thick*, *TEAngle*, *Camber*, *LEAngles*, *Curv*, *PAngle*, *Growth*, *Non conv*, *TotalP* refer to exceptions due to the penalties aerofoil thickness, trailing edge angle, aerofoil camber, leading edge angle, curvature reversals, panel angles, growth rate, non convergence of the XFOIL analysis and total penalty, respectively. *Conv* denotes when the XFOIL solution has converged.

Analysing the Figure 4.8, at the start of the optimisation most evaluations were geometric exceptions, mainly *Thick*, *TEAngle* and *Curv*. From iteration 26 to 200, the number of *Conv* rapidly increases, taking the place of the geometric exceptions as the most numerous type of evaluation, the frequency of the later continually decreases during the optimisation. From iterations 380 to 670, *Non conv* frequency was significantly higher. From 670 to 1000, it kept being a common evaluation type together with *Conv* and *Curv*.

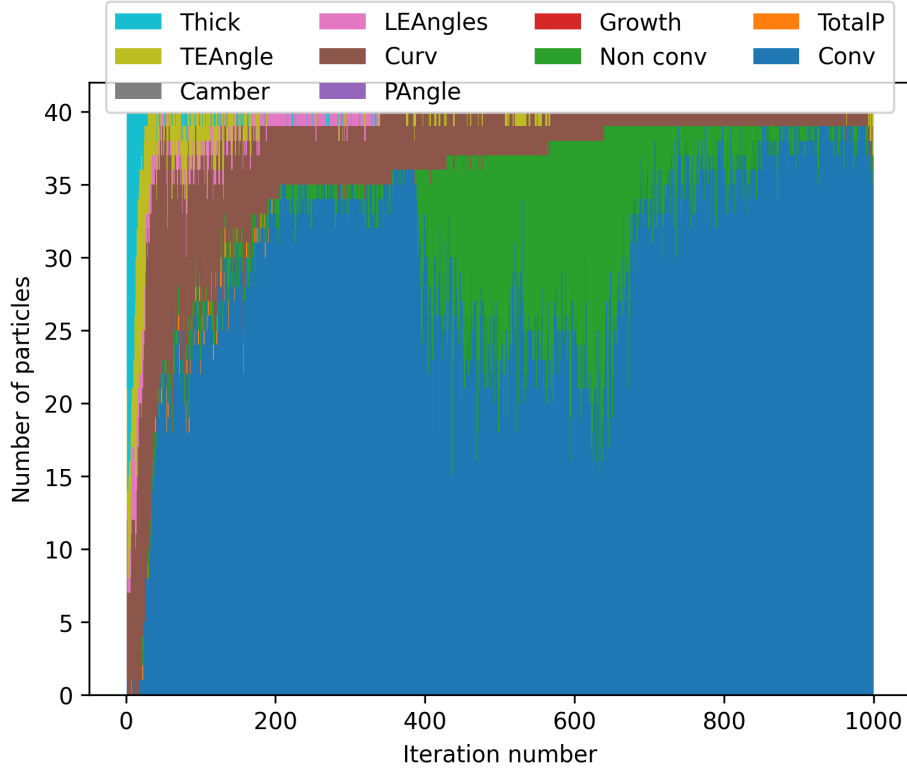


Figure 4.8: Aerofoil evaluation type count for each iteration during optimisation.

An increase in the number of *Curv* after iteration 335 was expected, since the number of curvature reversals per surface decreases from 4 to 3, this decrease is due to the penalty limit linear descent. However, there was no increase in *Curv*, this means the average number of curvature reversals already was smaller or equal to 3.

The total number of evaluations is presented in Figure 4.9, where it can be confirmed that *Conv*, *Non conv* and *Curv* are the most common aerofoil evaluations during the optimisation. Notice that there are no *Camber* evaluations, because aerofoil camber is not constrained and the maximum panel angle of 25 deg constraint was always fulfilled within the penalty limit, since *PAngle* is zero. It is important to note that the small number of *Growth* and *TotalP* instances, may result from XOPTFOIL checking the penalties sequentially. If only the total penalty was checked, all exceptions would be *TotalP* and if the *Growth* was checked sooner it would have a higher count.

The design variables density distribution and point distribution for the first one-hundred iterations is shown in Figure 4.10, where *Passed* refers to the *Conv* aerofoil evaluation type and *All* refers to all evaluation types. The flap design variables are scaled between 0 and 1, with 0 being its minimum limit and 1 its maximum limit,  $F_1, F_2, F_3, F_4$  are the flap deflections and  $F_5$  is the flap hinge position.  $D_1$  to  $D_{12}$  are the vertical positions of the control points.

Notice that Figures 4.10a and 4.10c have a greater interval than Figures 4.10b and 4.10d. While *All* interval is a consequence of initial perturbations and conditions, the *Passed* in-

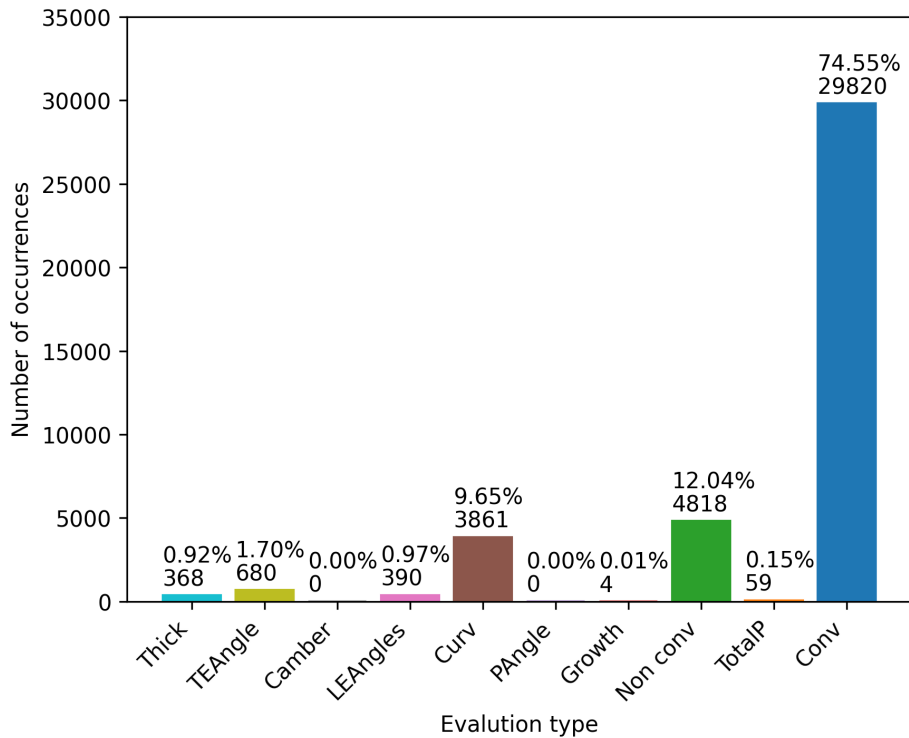


Figure 4.9: Total aerofoil evaluation type count for the optimisation.

terval is defined by the *All* interval and the ability to pass all constraints and converge in XFOIL.

By iteration 100, the design variables have concentrated in even smaller intervals, where the density distribution is high, this is in accordance with the design radius, which decreases from iteration 3 to 100.

The aerodynamic properties have varied greatly during the optimisation. Figure 4.11 presents the variation of angle of attack for the maximum lift coefficient, maximum lift coefficient, lift coefficient and drag coefficient in take-off,  $\alpha_{C_{l,max,TO}}$ ,  $C_{l,max,TO}$ ,  $C_{l,TO}$ ,  $C_{d,TO}$ . In all of the properties, there is a higher range of values between 1 to 200 iterations, at this point most converge.

The angle of attack for the maximum lift coefficient varies from 8 to 17 degrees, the sequence analysis limits. By the end of the optimisation it continues to vary from 12 to 15 degrees. By analysing  $C_{l,max,TO}$ , it is possible to observe that by the final parts of the optimisation, some values of the minimum  $C_{l,max,TO}$  oscillate between set levels. This is probably the cause of the angle variation.

$C_{l,max,TO}$  initially decreases during the first 100 iterations, however onwards it increases and stays near the maximum value. Notice that there are several values higher than the final value, these were not selected as solution due to the other properties. Both  $C_{l,TO}$  and  $C_{d,TO}$  mostly increase during the optimisation.

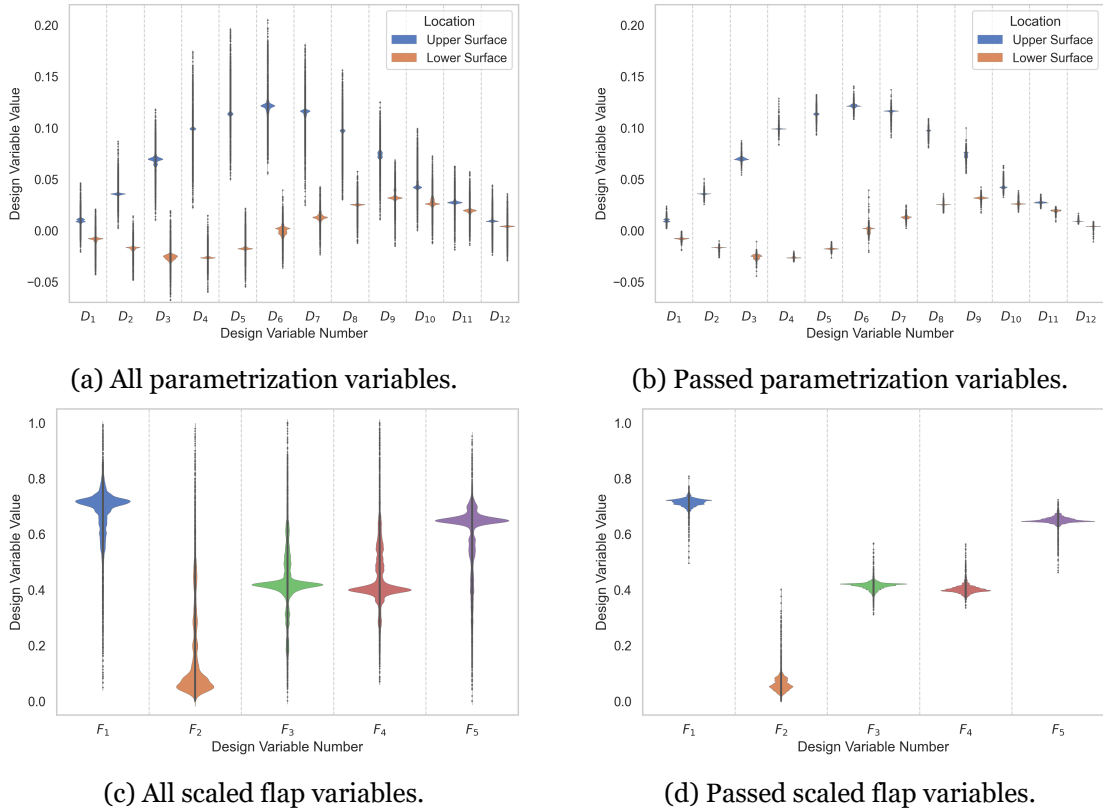


Figure 4.10: Violin graph of design variables up to iteration 100 for case 2.

Regarding the cruise, turn and climb properties in Figure 4.12, the drag coefficients change very early during optimisation, they cause the decrease of  $C_{l,max,TO}$ , then remain stagnant. In a similar fashion to  $C_{l,TO}$ ,  $C_{l,climb}$  changes rapidly for the initial 200 iterations and mostly increases until iteration 400.

From the maximum values of the penalty  $\delta$  in Figure 4.13b it is possible to visualize the penalty limit variation from 0.5 to 0.0001. Note that until iteration 230 there was a significant level of one third, corresponding to the curvature reversals penalty. By iteration 335 this level already was insignificant, thus there was no increase in the number of exceptions. No solution had any penalty. From Figure 4.13a it is possible to see the relation between  $Obj$  and  $\delta$ .

Not a single solution had a penalty value different from zero. At this point it is important to find whether the penalty limit had any effect on the optimisation outcome. Figure 4.14 presents the number of particles and the number of particle best per iteration with a non zero penalty. At the start of the optimisation the penalty limit allowed several particles to become particle best, this continued on a lesser frequency during the optimisation. Table 4.36 summarizes the finds, from 6695 particles with a non zero penalty, 108 were particle bests.

In order to estimate how useful was initialization sequence when doing XFOIL analysis, the

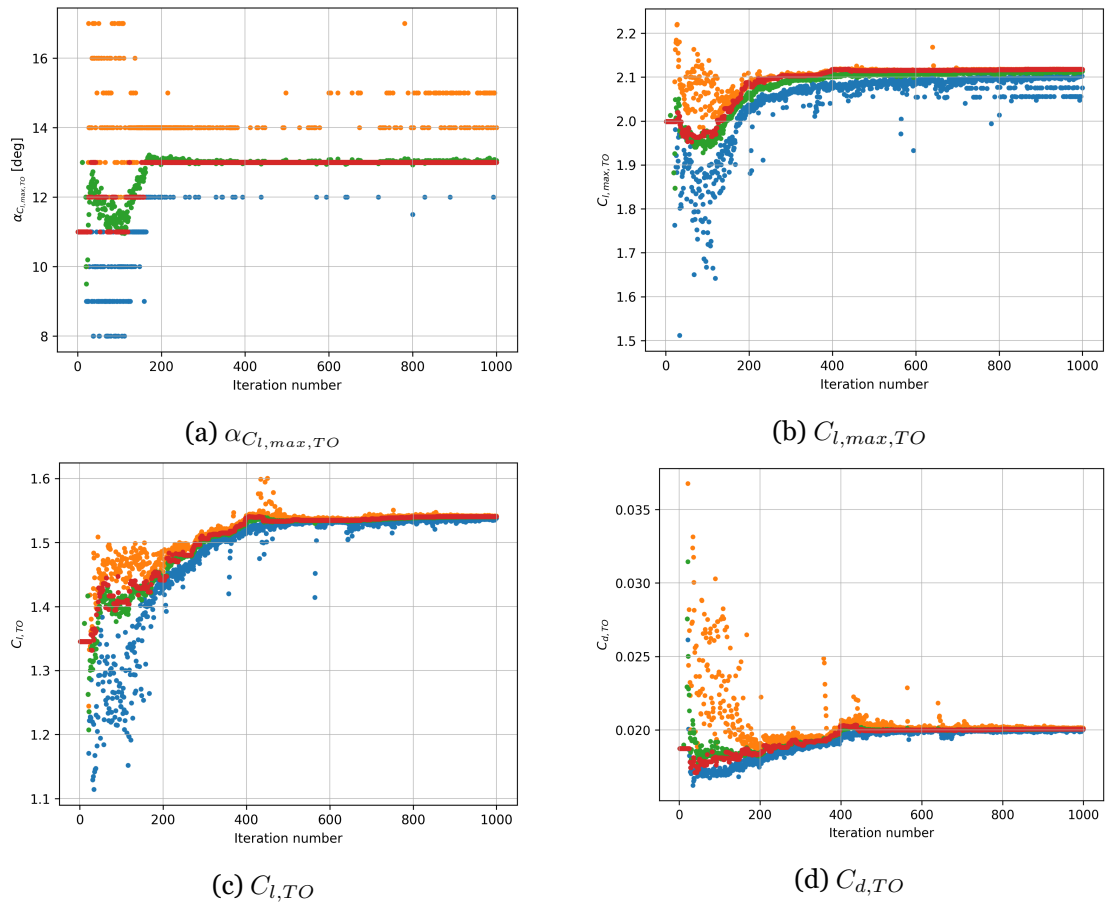


Figure 4.11: Take-off properties maximum (in orange), average (in green), minimum (in blue) and global best value (in red) per population for *Conv* aerofoil evaluation during optimisation.

Table 4.36: Number of particles, particle best and global best with a non zero penalty value.

	$Particles_{\delta>0}$	$PB_{\delta>0}$	$GB_{\delta>0}$
Count	6695	108	0

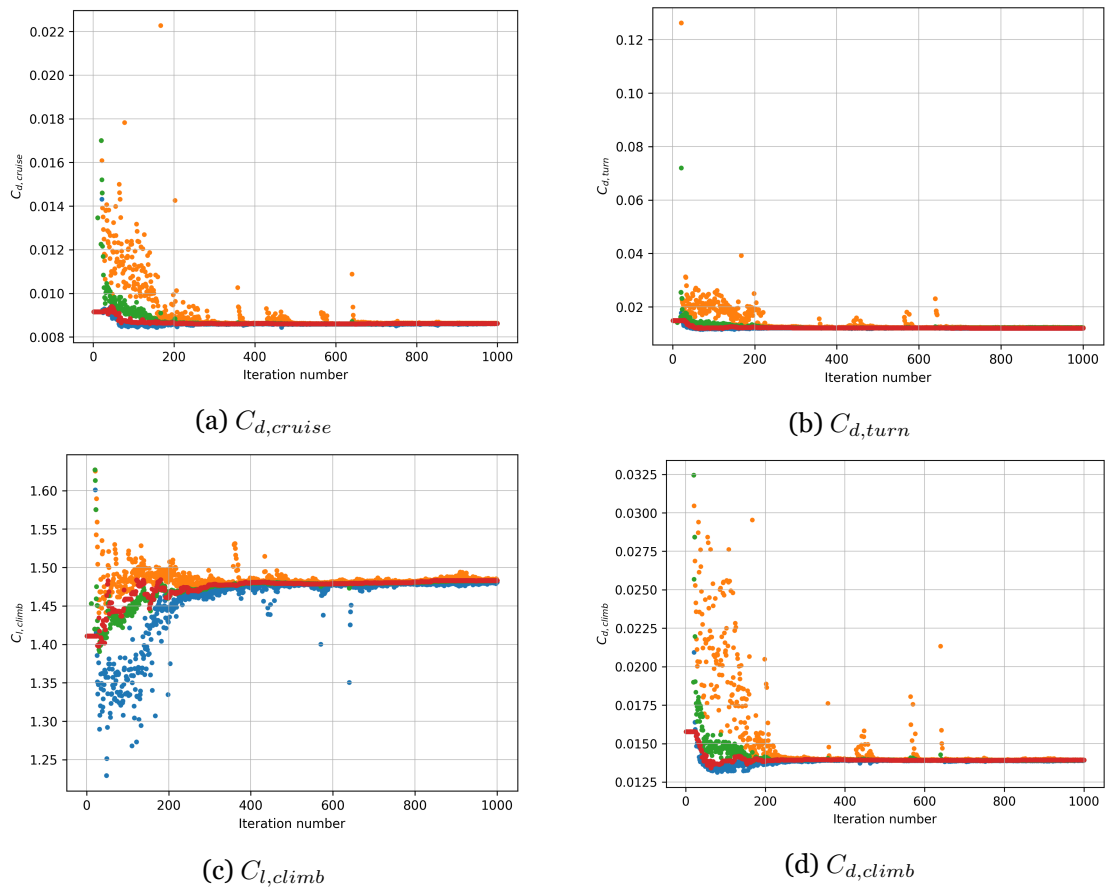


Figure 4.12: Cruise, turn and climb properties maximum (in orange), average (in green), minimum (in blue) and global best value (in red) per population for *Conv* aerofoil evaluation during optimisation.

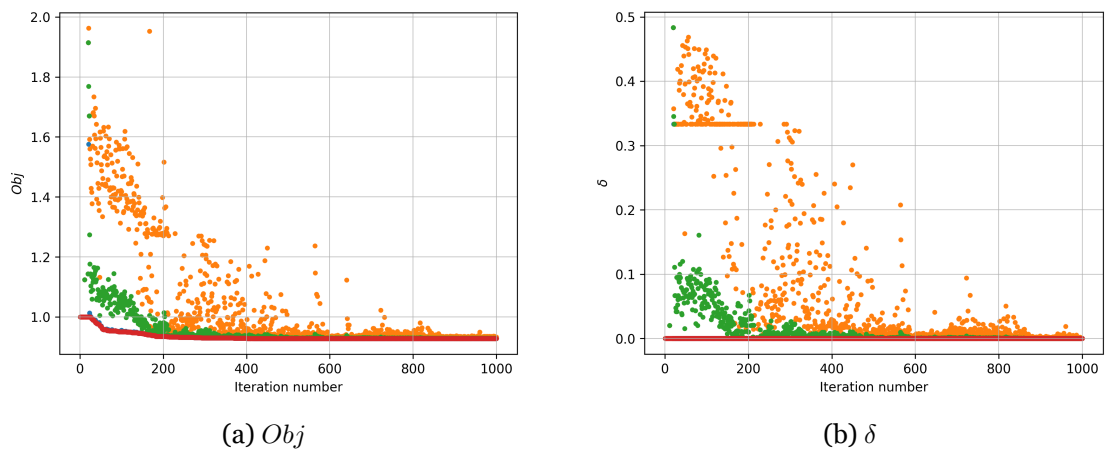


Figure 4.13:  $Obj$  and  $\delta$  maximum (in orange), average (in green), minimum (in blue) and global best value (in red) per population for *Conv* aerofoil evaluation during optimisation.

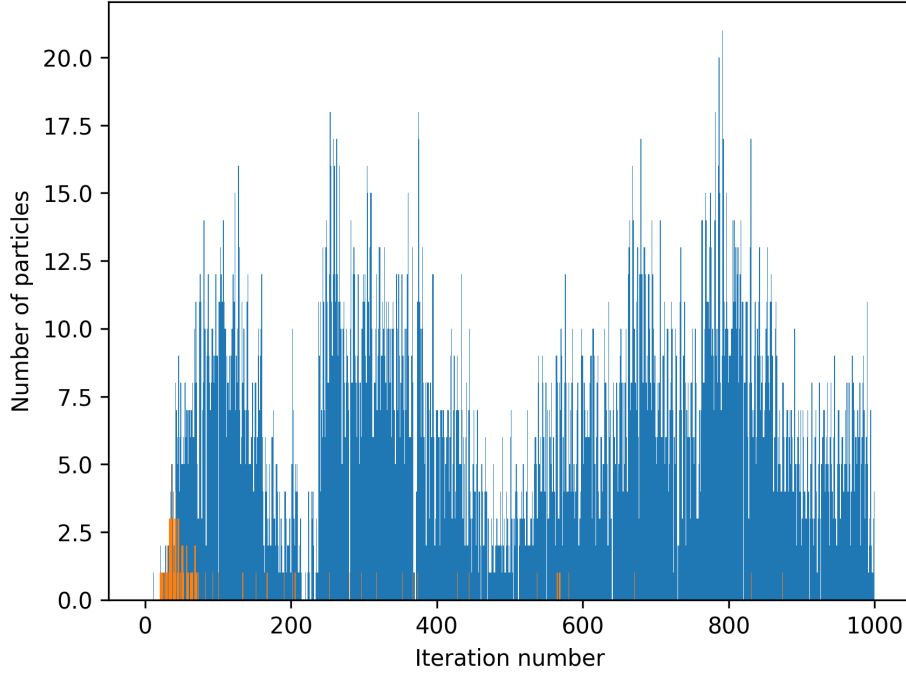


Figure 4.14: Number of particles with a non zero penalty per iteration (blue) and number of particle best with a non zero penalty.

number of each analysis type (single point analysis  $SPA$ , initialization sequence analysis  $IA$  or sequence analysis  $SA$ ), which routine executed the analysis (normal evaluation  $N$  or consistency check  $C$ ) and resolution (convergence  $Conv$  or non convergence  $Non\ conv$ ) are presented in Table 4.37. The number of particle best and global best with at least an initialization sequence is also shown  $PB_{with\ IA}$  and  $GB_{with\ IA}$ .

Table 4.37: XFOIL analysis count for the optimisation.

	$SPA_{N,Conv}$	$IA_{N,Conv}$	$SA_{N,Conv}$	$IA_{N,Non\ Conv}$	$PB_{with\ IA}$
Count	199229	3700	34635	4902	211
	$SPA_{C,Conv}$	$IA_{C,Conv}$	$SA_{C,Conv}$	$IA_{C,Non\ Conv}$	$GB_{with\ IA}$
Count	94	3	23	4	16

Table 4.38 presents the total values for each type of analysis and the corresponding number of VISCAL calls. Note that VISCAL is responsible for most of the tool execution time.

Out of 8609 initialization analysis, only 3703 converged or 43.0% and it was responsible for 14.78% of execution time. However it resulted in 211 particle best and 16 global best that would not have been found. By finding these solutions it affected the optimisation significantly.

Regarding the consistency check, the number of checks is insignificant. As soon as, a maximum lift coefficient is found there is a consistency check, however if no new maximums are found then no new check is performed. In the same manner, as soon as no minimum drag

coefficients are found, no check are done. By observing Figures 4.11 and 4.12, most maxima and minima are found at the start of the optimisation. During optimisation there was only a single value that when checked, yielded a relative difference greater than 1%.

Sequence analysis is integral to the determination of maximum lift coefficient during take-off, however it is also the most expensive analysis and lacks precision. Increasing precision leads to higher computational costs.

Table 4.38: Total XFOIL analysis and Viscal counts.

	<i>SPA<sub>Total</sub></i>	<i>IA<sub>Total</sub></i>	<i>SA<sub>Total</sub></i>	Total
Call count	199323	8609	34658	237684
VISCAL count	199323	94699	346580	640602
VISCAL ratio	31.11%	14.78%	54.10%	100%



# Chapter 5

## Conclusions

For the purpose of this work, the tool XOPTFOIL was modified. The parametrization methods B-Spline, Class Shape Functions and Bezier-PARSEC were added; plain flap hinge position and trailing edge thickness were introduced as design variables; XFOIL non convergence options were introduced; constraints became relative to the original aerofoil; design radius function was changed; relative initial perturbation and constraint limit parameters were added; and maximum lift coefficient optimization type can now use a sequence of angles of attack.

In case study 1, an aerofoil was optimized for the Air Cargo Challenge 2019 conditions using different aerofoil parametrizations and number of design variables. From the results, it was shown that a higher number of design variables leads to higher aerodynamic performance in the resulting aerofoils. The B-Spline parametrization results in higher performance, while Class Shape Functions and Hicks-Henne have similar results and Bezier-PARSEC the lowest. However, Class Shape Functions present less curvature reversals and trailing edge angle changes during optimization with higher numbers of design variables when compared to other parametrizations. It was also shown that the optimized aerofoil designs have higher aerodynamic performance than the original aerofoil near the operating points, particularly the drag coefficient during cruise which has worse off-design performance.

Case study 2 focused on a single analysis of the same aerofoil for the Air Cargo Challenge 2022 objectives. Results showed that the consistency check is inexpensive and may catch some outliers during the early stages of the optimization. The penalty function did not directly affect the solution, however it did affect some of the particle best particularly at the start of the optimization and therefore shaped the optimization path. The initialization analysis used to correct XFOIL non convergence managed to fix over 40% of non convergence cases with significant impact on the execution time. The sequence analysis used to determine the maximum lift coefficient worked, however it has the most cost and low precision. It does not scale well for higher precision both requiring more points and increased cost.

Both cases showed that the constraint of the number of curvature reversals was insufficient and generally inadequate as is currently implemented.

## **5.1 Future work**

For future works it would be of interest to study the impact of initial perturbations, constraints limits and optimization parameters on the optimised aerofoils. The use of a different type of penalty function or even removing it in favor of a constraint objective may be beneficial for curvature constraints. A different approach for maximum lift determination is of interest. Utilising a gradient method may yield better results for a lower cost. The use of multiple objective optimization algorithms would eliminate the weight determination process and provide a set of aerofoils that could then be compared using the aircraft equations without linearization. Utilising an extremely robust aerodynamic solver may eliminate the need for several constraints.

# Bibliography

- [1] A. S. Saeed, A. B. Younes, C. Cai, and G. Cai, "A survey of hybrid Unmanned Aerial Vehicles," *Progress in Aerospace Sciences*, vol. 98, pp. 91–105, 2018. doi: 10.1016/j.paerosci.2018.03.007. 1
- [2] TechNavio, "UAV Market by Application and Geography - Forecast and Analysis 2020-2024," 2020. [Online]. Available: <https://www.technavio.com/report/uav-market-industry-analysis> 1
- [3] A. Tummala, R. K. Velamati, D. K. Sinha, V. Indraja, and V. H. Krishna, "A review on small scale wind turbines," *Renewable and Sustainable Energy Reviews*, vol. 56, pp. 1351–1371, 2016. doi: 10.1016/j.rser.2015.12.027. 1
- [4] B. H. Fiedler and M. S. Bukovsky, "The effect of a giant wind farm on precipitation in a regional climate model," *Environmental Research Letters*, vol. 6, no. 4, p. 045101, 2011. doi: 10.1088/1748-9326/6/4/045101. 1
- [5] D. W. Keith, J. F. Decarolis, D. C. Denkenberger, D. H. Lenschow, S. L. Malyshev, S. Pacala, and P. J. Rasch, "The influence of large-scale wind power on global climate," *Proceedings of the National Academy of Sciences of the United States of America*, vol. 101, no. 46, pp. 16 115–16 120, 2004. doi: 10.1073/pnas.0406930101. 1
- [6] C. Wang and R. G. Prinn, "Potential climatic impacts and reliability of very large-scale wind farms," *Atmospheric Chemistry and Physics*, vol. 10, no. 4, pp. 2053–2061, 2010. doi: 10.5194/acp-10-2053-2010. 1
- [7] V. de Brederode, *Aerodinâmica Incompressível - Fundamentos*. IST - Instituto Superior Técnico, 2014. 3
- [8] M. Selig, "Low Reynolds Number Airfoil Design Lecture Notes," 2020. [Online]. Available: <https://m-selig.ae.illinois.edu/pubs/Selig-2003-VKI-LRN-Airfoil-Design-Lecture-Series.pdf> 5
- [9] S. N. Skinner and H. Zare-Behtash, "State-of-the-art in aerodynamic shape optimisation methods," *Applied Soft Computing*, vol. 62, pp. 933–962, jan 2018. doi: 10.1016/J.ASOC.2017.09.030. 5, 10, 11, 49
- [10] D. A. Masters, N. J. Taylor, T. Rendall, C. B. Allen, and D. J. Poole, "Review of Aerofoil Parameterisation Methods for Aerodynamic Shape Optimisation," in *53rd AIAA Aerospace Sciences Meeting*. American Institute of Aeronautics and Astronautics, Jan. 2015. doi: 10.2514/6.2015-0761. 6, 7, 8, 9, 18, 20

- [11] D. Nelson, “Numerical Optimization of Airfoils in Low Reynolds Number Flows,” *Journal of Aircraft*, vol. 46, no. 1, pp. 331–337, 2009. doi: 10.2514/1.36859. 6
- [12] V. Braibant and C. Fleury, “Shape optimal design using B-splines,” *Computer Methods in Applied Mechanics and Engineering*, vol. 44, no. 3, pp. 247–267, 1984. doi: 10.1016/0045-7825(84)90132-4. 6
- [13] H. Sobieczky, “Geometry Generator for CFD and Applied Aerodynamics,” in *New Design Concepts for High Speed Air Transport*, ser. International Centre for Mechanical Sciences (Courses and Lectures), H. Sobieczky, Ed. Springer, Vienna, 1997, vol. 366, pp. 137–157. doi: 10.1007/978-3-7091-2658-5\_9. 6
- [14] B. M. Kulfan and J. E. Bussoletti, ““Fundamental” Parametric Geometry Representations for Aircraft Component Shapes,” in *11th AIAA/ISSMO Multidisciplinary Analysis and Optimization Conference*, Sep. 2006. doi: 10.2514/6.2006-6948. 6, 7, 21
- [15] B. M. Kulfan, “Universal Parametric Geometry Representation Method,” *Journal of Aircraft*, vol. 45, no. 1, pp. 142–158, 2008. doi: 10.2514/1.29958. 6, 7, 21
- [16] A. Jameson, “Aerodynamic design via control theory,” *Journal of Scientific Computing*, vol. 3, no. 3, pp. 233–260, 1988. doi: 10.1007/BF01061285. 6, 8
- [17] R. M. Hicks and P. A. Henne, “Wing design by numerical optimization,” *Journal of Aircraft*, vol. 15, no. 7, pp. 407–412, 1978. doi: 10.2514/3.58379. 6, 8, 18
- [18] D. Chauhan, P. Chandrashekarappa, and R. Duval, “Wing shape optimization using FFD and twist parameterization,” in *12th Aerospace Society of India CFD Symposium*, Bangalore, India, Aug. 2010. [Online]. Available: <https://hal.inria.fr/inria-00537316> 6, 8
- [19] T. C. S. Rendall and C. B. Allen, “Unified fluid–structure interpolation and mesh motion using radial basis functions,” *International Journal for Numerical Methods in Engineering*, vol. 74, no. 10, pp. 1519–1559, 2008. doi: 10.1002/nme.2219. 6
- [20] G. Carpentieri, M. J. L. van Tooren, and B. Koren, “Aerodynamic Shape Optimization by Means of Sequential Linear Programming Technique,” in *Proceedings of the European Conference on Computational Fluid Dynamics, Egmond aan Zee, The Netherlands. ECCOMAS CFD 2006*, Sep. 2006. [Online]. Available: <https://repository.tudelft.nl/islandora/object/uuid:f25d2c00-294d-4f18-9f99-827f3cffb09b/> 6
- [21] L. Piegl and W. Tiller, *The NURBS Book*, 2nd ed., ser. Monographs in Visual Communications. Springer, Berlin, Heidelberg, 1997. 6

- [22] C. de Boor, *A Practical Guide to Splines*. Springer-Verlag New York, 1978, vol. Applied Mathematical Sciences, no. 27. 6, 20
- [23] H. Sobieczky, “Parametric Airfoils and Wings,” in *Recent Development of Aerodynamic Design Methodologies*, ser. Notes on Numerical Fluid Mechanics, K. Fujii and G. Dulikravich, Eds. Vieweg+Teubner Verlag, 1999, vol. 65, pp. 71–87. doi: 10.1007/978-3-322-89952-1\_4. 7
- [24] R. W. Derksen and T. Rogalsky, “Bezier-PARSEC: An optimized aerofoil parameterization for design,” *Advances in Engineering Software*, vol. 41, no. 7–8, pp. 923–930, 2010. doi: 10.1016/j.advengsoft.2010.05.002. xi, 7, 22
- [25] Kulfan, B. M., “Modification of CST airfoil representaiton methodology.” [Online]. Available: <http://www.brendakulfan.com/docs/CST8.pdf> 7, 21
- [26] I.-C. Chang, F. Torres, and C. Tung, “Geometric Analysis of Wing Sections,” National Aeronautics and Space Administration, Ames Research Center: Moffett Field, California 94035-1000, Technical Memorandum 110346, april 1995. [Online]. Available: <https://ntrs.nasa.gov/citations/19950018209> 7, 18
- [27] D. J. J. Toal, N. W. Bressloff, A. J. Keane, and C. M. E. Holden, “Geometric Filtration Using Proper Orthogonal Decomposition for Aerodynamic Design Optimization,” *AIAA Journal*, vol. 48, no. 5, pp. 916–928, 2010. doi: 10.2514/1.41420. 7
- [28] T. W. Sederberg and S. R. Parry, “Free-form deformation of solid geometric models,” in *Proceedings of the 13th annual conference on Computer graphics and interactive techniques*, 1986, pp. 151–160. doi: 10.1145/15886.15903. 8
- [29] C. Allen and T. Rendall, “Unified Approach to CFD-CSD Interpolation and Mesh Motion Using Radial Basis Functions,” in *25th AIAA Applied Aerodynamics Conference*, Jun. 2007. doi: 10.2514/6.2007-3804. 8
- [30] V. Sripawadkul, M. Padulo, and M. Guenov, “A Comparison of Airfoil Shape Parameterization Techniques for Early Design Optimization,” in *13th AIAA/ISSMO Multidisciplinary Analysis Optimization Conference*, Sep. 2010. doi: 10.2514/6.2010-9050. xiii, 8, 9
- [31] D. Rajnarayan, A. Ning, and J. A. Mehr, “Universal Airfoil Parameterization Using B-Splines,” in *2018 Applied Aerodynamics Conference*, Jun. 2018. doi: 10.2514/6.2018-3949. 8
- [32] D. A. Masters, N. J. Taylor, T. C. S. Rendall, C. B. Allen, and D. J. Poole, “Geometric Comparison of Aerofoil Shape Parameterization Methods,” *AIAA Journal*, vol. 55, no. 5,

- pp. 1575–1589, 2017. doi: 10.2514/1.J054943. xi, 8, 9, 10, 20, 21, 56
- [33] T. tian Zhang, Z. guo Wang, W. Huang, and L. Yan, “A review of parametric approaches specific to aerodynamic design process,” *Acta Astronautica*, vol. 145, pp. 319–331, 2018. doi: 10.1016/j.actaastro.2018.02.011. xi, 8, 9, 10
- [34] D. A. Vicente, P. V. Gamboa, and M. A. R. Silvestre, “Parameterization formulations for aerofoil shape optimization,” in *Proceedings of 4th International Conference on Engineering Optimization, Lisbon, Portugal, 10-11 September, 2014*. xiii, 9, 11
- [35] A. Arias-Montano, C. A. C. Coello, and E. Mezura-Montes, “Multiobjective Evolutionary Algorithms in Aeronautical and Aerospace Engineering,” *IEEE Transactions on Evolutionary Computation*, vol. 16, no. 5, pp. 662–694, 2012. doi: 10.1109/TEVC.2011.2169968. 11
- [36] R. Eberhart and J. Kennedy, “A new optimizer using particle swarm theory,” in *MHS’95. Proceedings of the Sixth International Symposium on Micro Machine and Human Science, 1995*, pp. 39–43. doi: 10.1109/MHS.1995.494215. 11
- [37] J. Kennedy and R. Eberhart, “Particle swarm optimization,” in *Proceedings of ICNN’95 - International Conference on Neural Networks*, vol. 4, 1995, pp. 1942–1948. doi: 10.1109/ICNN.1995.488968. 11
- [38] M. Drela, “XFOIL: An analysis and design system for low Reynolds number airfoils,” in *Low Reynolds Number Aerodynamics*, ser. Lecture Notes in Engineering, T. J. Mueller, Ed. Springer, Berlin, Heidelberg, 1989, vol. 54. doi: 10.1007/978-3-642-84010-4\_1. 12, 28
- [39] J. Morgado, R. Vizinho, M. Silvestre, and J. Páscoa, “XFOIL vs CFD performance predictions for high lift low Reynolds number airfoils,” *Aerospace Science and Technology*, vol. 52, pp. 207–214, 2016. doi: 10.1016/j.ast.2016.02.031. 12
- [40] M. Gunasekaran and R. Mukherjee, “Behaviour of trailing wing(s) in echelon formation due to wing twist and aspect ratio,” *Aerospace Science and Technology*, vol. 63, pp. 294–303, 2017. doi: 10.1016/j.ast.2017.01.009. 12
- [41] S. Zhang, H. Li, and A. A. Abbasi, “Design methodology using characteristic parameters control for low Reynolds number airfoils,” *Aerospace Science and Technology*, vol. 86, pp. 143–152, 2019. doi: 10.1016/j.ast.2019.01.003. 12
- [42] D. Prosser, “XOPTFOIL,” 2017, Computational tool. [Online]. Available: <https://github.com/montagdude/Xoptfoil/tree/master> 12, 13

- [43] Fons, “Python XFOIL optimization toolbox,” 2014, Computational tool. [Online]. Available: <https://github.com/The-Fonz/xfoil-optimization-toolbox> 12
- [44] W. Chen, K. Chiu, and M. D. Fuge, “Bézier-GAN,” 2019, Computational tool. [Online]. Available: <https://github.com/IDEALLab/bezier-gan> 12
- [45] W. Chen, K. Chiu, and M. D. Fuge, “Airfoil Design Parameterization and Optimization Using Bézier Generative Adversarial Networks,” *AIAA Journal*, vol. 58, no. 11, pp. 4723–4735, 2020. doi: 10.2514/1.J059317. 12
- [46] X. Wei, X. Wang, and S. Chen, “Research on parameterization and optimization procedure of low-Reynolds-number airfoils based on genetic algorithm and Bezier curve,” *Advances in Engineering Software*, vol. 149, p. 102864, 2020. doi: 10.1016/j.advengsoft.2020.102864. 12
- [47] R. Palmeira, “XOPTFOIL,” 2022, Computational tool. [Online]. Available: <https://github.com/r-palmeira-pt> 15
- [48] M. Drela and H. Youngren, *XFOIL 6.9 User Primer*, 2001. [Online]. Available: [https://web.mit.edu/drela/Public/web/xfoil/xfoil\\_doc.txt](https://web.mit.edu/drela/Public/web/xfoil/xfoil_doc.txt) 28
- [49] D. P. Raymer, *Aircraft Design: A Conceptual Approach*, 2nd ed., ser. EDUCATION SERIES, J. A. Schetz, Ed. American Institute of Aeronautics and Astronautics, 1992. 33, 35
- [50] Air Cargo Challenge 2019, “Regulations for Air Cargo Challenge 2019 in Stuttgart,” 2018. [Online]. Available: <http://www.euroavia.de/ACC/documents/regulation.pdf> 35, 45
- [51] Air Cargo Challenge 2022, “Participation Handbook,” 2021. [Online]. Available: [https://akamodell-muenchen.de/wp-content/uploads/2021/03/regulations\\_acc\\_2022\\_munich\\_v01\\_11.pdf](https://akamodell-muenchen.de/wp-content/uploads/2021/03/regulations_acc_2022_munich_v01_11.pdf) 35, 59
- [52] A. P. Piotrowski, J. J. Napiorkowski, and E. A. Piotrowska, “Population size in Particle Swarm Optimization,” *Swarm and Evolutionary Computation*, vol. 52, p. 100718, 2020. doi: 10.1016/j.swevo.2020.100718. 37, 49
- [53] E. Juárez-Castillo, H.-G. Acosta-Mesa, and E. Mezura-Montes, “Empirical study of bound constraint-handling methods in Particle Swarm Optimization for constrained search spaces,” in *2017 IEEE Congress on Evolutionary Computation (CEC)*, 2017, pp. 604–611. doi: 10.1109/CEC.2017.7969366. 38
- [54] P. F. Albuquerque, P. V. Gamboa, and M. A. Silvestre, “Mission-Based Multidisciplinary

Aircraft Design Optimization Methodology Tailored for Adaptive Technologies,” *Journal of Aircraft*, vol. 55, no. 2, pp. 755–770, 2018. doi: 10.2514/1.C034403. 46, 61



# Appendix A

## Full weights equations

As stated in Section 3.4.4 each weight is related to a property to optimize. Additionally weight determination depends on which operational objectives are utilised.

### A.1 Analysis case 1

In case 1 there are only two objectives, maximum payload weight  $W_{payload}$  and minimum time flown  $t_{flight}$ , meaning that the relevant aerodynamic properties are  $C_{l,max}$ ,  $C_l$  and  $C_d$  at take-off (TO),  $C_d$  in the turn and  $C_d$  in the cruise, leading to Equation A.1, where  $w_i$  is determined using Equation 3.56.

$$\delta Score \approx w_1 \delta C_{l,max,TO} + w_2 \delta C_{l,TO} + w_3 \delta C_{d,TO} + w_4 \delta C_{d,cruise} + w_5 \delta C_{d,turn} \quad (\text{A.1})$$

Expanding Equation 3.56 for  $w_1$ , Equation A.2 is obtained.

$$w_1 = \frac{\partial W_{payload}}{\partial C_{l,max,TO}} \frac{C_{l,max,TO}}{W_{payload}} + \frac{\partial t_{flight}}{\partial C_{l,max,TO}} \frac{C_{l,max,TO}}{t_{flight}} \quad (\text{A.2})$$

According to Equation 3.50,  $t_{flight}$  is not influenced by  $C_{l,max,TO}$ . From Equations 3.46 and 3.45 it is possible to obtain Equation A.3.

$$w_1 = -\frac{\partial W_{payload}}{\partial W} \left( \frac{\partial S_G}{\partial W} \right)^{-1} \frac{\partial S_G}{\partial C_{L,max,TO}} \frac{\partial C_{L,max,TO}}{\partial C_{l,max,TO}} \frac{C_{l,max,TO}}{C_{L,max,TO}} \frac{C_{L,max,TO}}{S_G} \frac{S_G}{W} \frac{W}{W_{payload}} \quad (\text{A.3})$$

In the same manner, Equations A.4 and A.5 are determined for  $w_2$  and  $w_3$ , respectively.

$$w_2 = -\frac{\partial W_{payload}}{\partial W} \left( \frac{\partial S_G}{\partial W} \right)^{-1} \frac{\partial S_G}{\partial C_{L,TO}} \frac{\partial C_{L,TO}}{\partial C_{l,TO}} \frac{C_{l,TO}}{C_{L,TO}} \frac{C_{L,TO}}{S_G} \frac{S_G}{W} \frac{W}{W_{payload}} \quad (\text{A.4})$$

$$w_3 = -\frac{\partial W_{payload}}{\partial W} \left( \frac{\partial S_G}{\partial W} \right)^{-1} \frac{\partial S_G}{\partial C_{D,TO}} \frac{\partial C_{D,TO}}{\partial C_{d,TO}} \frac{C_{d,TO}}{C_{D,TO}} \frac{C_{D,TO}}{S_G} \frac{S_G}{W} \frac{W}{W_{payload}} \quad (\text{A.5})$$

For  $w_4$ , the expansion of Equation 3.56 results in Equation A.6.

$$w_4 = \frac{\partial W_{payload}}{\partial C_{d,cruise}} \frac{C_{d,cruise}}{W_{payload}} + \frac{\partial t_{flight}}{\partial C_{d,cruise}} \frac{C_{d,cruise}}{t_{flight}} \quad (\text{A.6})$$

Since the drag coefficient influence on the payload weight is small, it will not be considered. Using Equations 3.50 and 3.52 results in Equation A.7.

$$w_4 = \frac{\partial t_{flight}}{\partial V_{cruise}} \frac{\partial V_{cruise}}{\partial C_{D,cruise}} \frac{\partial C_{D,cruise}}{\partial C_{d,cruise}} \frac{C_{d,cruise}}{C_{D,cruise}} \frac{C_{D,cruise}}{V_{cruise}} \frac{V_{cruise}}{t_{flight}} \quad (\text{A.7})$$

In the same manner, using Equations 3.50 and 3.53, not considering the drag coefficient influence on the payload weight, the expansion of Equation 3.56 results in Equation A.8.

$$w_5 = \frac{\partial t_{flight}}{\partial V_{turn}} \frac{\partial V_{turn}}{\partial C_{D,turn}} \frac{\partial C_{D,turn}}{\partial C_{d,turn}} \frac{C_{d,turn}}{C_{D,turn}} \frac{C_{D,turn}}{V_{turn}} \frac{V_{turn}}{t_{flight}} \quad (\text{A.8})$$

Additionally one relationship is utilised to determine part of Equations A.7 and A.8, Equation A.9 by considering that the turn velocity and the cruise velocity are similar.

$$\left\{ \begin{array}{l} \frac{\partial t_{flight}}{\partial V_{turn}} \frac{V_{turn}}{t_{flight}} = -\frac{\hat{S}_{turn}}{V_{turn}^2} \frac{V_{turn}}{\frac{\hat{S}_{turn}}{V_{turn}} + \frac{\hat{S}_{cruise}}{V_{cruise}}} = -\frac{\hat{S}_{turn}}{\hat{S}_{turn} + \hat{S}_{cruise}} \frac{V_{turn}}{V_{cruise}} \approx -\frac{\hat{S}_{turn}}{\hat{S}_{turn} + \hat{S}_{cruise}} \\ \frac{\partial t_{flight}}{\partial V_{cruise}} \frac{V_{cruise}}{t_{flight}} = -\frac{\hat{S}_{cruise}}{V_{cruise}^2} \frac{V_{cruise}}{\frac{\hat{S}_{turn}}{V_{turn}} + \frac{\hat{S}_{cruise}}{V_{cruise}}} = -\frac{\hat{S}_{cruise}}{\hat{S}_{turn} \frac{V_{cruise}}{V_{turn}} + \hat{S}_{cruise}} \approx -\frac{\hat{S}_{cruise}}{\hat{S}_{turn} + \hat{S}_{cruise}} \end{array} \right. \quad (\text{A.9})$$

## A.2 Analysis case 2

In case 2 there are three objectives: maximum payload weight  $W_{payload}$ , flight distance within 120 s  $\hat{S}_{flight}$  and altitude within 60 s  $h_{60s}$ . In Section 3.4.4 the aerodynamic properties which influence these have been identified,  $C_{l,max}$ ,  $C_l$  and  $C_d$  at take-off,  $C_d$  in the turn,  $C_d$  in the cruise and  $C_l$  and  $C_d$  during climb, leading to Equation 4.13, where  $w_i$  is determined using

Equation 3.56.

$$\begin{aligned} \delta Score \propto w_1 \delta C_{l,max,TO} + w_2 \delta C_{l,TO} + w_3 \delta C_{d,TO} \\ + w_4 \delta C_{d,cruise} + w_5 \delta C_{d,turn} + w_6 \delta C_{l,climb} + w_7 \delta C_{d,climb} \end{aligned} \quad (\text{A.10})$$

Expanding Equation 3.56 for  $w_1$ , Equation A.11.

$$w_1 = \frac{\partial W_{payload}}{\partial C_{l,max,TO}} \frac{C_{l,max,TO}}{W_{payload}} + \frac{\partial \hat{S}_{flight}}{\partial C_{l,max,TO}} \frac{C_{l,max,TO}}{\hat{S}_{flight}} + \frac{\partial h_{60s}}{\partial C_{l,max,TO}} \frac{C_{l,max,TO}}{h_{60s}} \quad (\text{A.11})$$

According to Equation 3.54,  $\hat{S}_{flight}$  is not influenced by  $C_{l,max,TO}$ . From Equations 3.46, 3.45 and 3.49 it is possible to obtain Equation A.12.

$$\begin{aligned} w_1 = - \frac{\partial W_{payload}}{\partial W} \left( \frac{\partial S_G}{\partial W} \right)^{-1} \frac{\partial S_G}{\partial C_{L,max,TO}} \frac{\partial C_{L,max,TO}}{\partial C_{l,max,TO}} \frac{C_{l,max,TO}}{C_{L,max,TO}} \frac{C_{L,max,TO}}{S_G} \frac{S_G}{W} \frac{W}{W_{payload}} \\ - \frac{\partial h_{60s}}{\partial V_V} \frac{\partial V_V}{\partial W} \left( \frac{\partial S_G}{\partial W} \right)^{-1} \frac{\partial S_G}{\partial C_{L,max,TO}} \frac{\partial C_{L,max,TO}}{\partial C_{l,max,TO}} \frac{C_{l,max,TO}}{C_{L,max,TO}} \frac{C_{L,max,TO}}{S_G} \frac{S_G}{W} \frac{W}{V_V} \frac{V_V}{h_{60s}} \end{aligned} \quad (\text{A.12})$$

In the same manner, Equations A.13 and A.14 are determined for  $w_2$  and  $w_3$ , respectively.

$$\begin{aligned} w_2 = - \frac{\partial W_{payload}}{\partial W} \left( \frac{\partial S_G}{\partial W} \right)^{-1} \frac{\partial S_G}{\partial C_{L,TO}} \frac{\partial C_{L,TO}}{\partial C_{l,TO}} \frac{C_{l,TO}}{C_{L,TO}} \frac{C_{L,TO}}{S_G} \frac{S_G}{W} \frac{W}{W_{payload}} \\ - \frac{\partial h_{60s}}{\partial V_V} \frac{\partial V_V}{\partial W} \left( \frac{\partial S_G}{\partial W} \right)^{-1} \frac{\partial S_G}{\partial C_{L,TO}} \frac{\partial C_{L,TO}}{\partial C_{l,TO}} \frac{C_{l,TO}}{C_{L,TO}} \frac{C_{L,TO}}{S_G} \frac{S_G}{W} \frac{W}{V_V} \frac{V_V}{h_{60s}} \end{aligned} \quad (\text{A.13})$$

$$\begin{aligned} w_3 = - \frac{\partial W_{payload}}{\partial W} \left( \frac{\partial S_G}{\partial W} \right)^{-1} \frac{\partial S_G}{\partial C_{D,TO}} \frac{\partial C_{D,TO}}{\partial C_{d,TO}} \frac{C_{d,TO}}{C_{D,TO}} \frac{C_{D,TO}}{S_G} \frac{S_G}{W} \frac{W}{W_{payload}} \\ - \frac{\partial h_{60s}}{\partial V_V} \frac{\partial V_V}{\partial W} \left( \frac{\partial S_G}{\partial W} \right)^{-1} \frac{\partial S_G}{\partial C_{D,TO}} \frac{\partial C_{D,TO}}{\partial C_{d,TO}} \frac{C_{d,TO}}{C_{D,TO}} \frac{C_{D,TO}}{S_G} \frac{S_G}{W} \frac{W}{V_V} \frac{V_V}{h_{60s}} \end{aligned} \quad (\text{A.14})$$

For  $w_4$ , the expansion of Equation 3.56 results in Equation A.15.

$$w_4 = \frac{\partial W_{payload}}{\partial C_{d,cruise}} \frac{C_{d,cruise}}{W_{payload}} + \frac{\partial \hat{S}_{flight}}{\partial C_{d,cruise}} \frac{C_{d,cruise}}{\hat{S}_{flight}} + \frac{\partial h_{60s}}{\partial C_{d,cruise}} \frac{C_{d,cruise}}{h_{60s}} \quad (\text{A.15})$$

Since the drag coefficient influence on the weight is small, it will not be considered, meaning that it does not influence payload weight nor altitude. Using Equations 3.54 and 3.52 results in Equation A.16.

$$w_4 = \frac{\partial \hat{S}_{flight}}{\partial V_{cruise}} \frac{\partial V_{cruise}}{\partial C_{D,cruise}} \frac{\partial C_{D,cruise}}{\partial C_{d,cruise}} \frac{C_{d,cruise}}{C_{D,cruise}} \frac{C_{D,cruise}}{V_{cruise}} \frac{V_{cruise}}{\hat{S}_{flight}} \quad (\text{A.16})$$

In the same manner, using Equations 3.54 and 3.53, not considering the drag coefficient influence on the weight, the expansion of Equation 3.56 results in Equation A.17.

$$w_5 = \frac{\partial \hat{S}_{flight}}{\partial V_{turn}} \frac{\partial V_{turn}}{\partial C_{D,turn}} \frac{\partial C_{D,turn}}{\partial C_{d,turn}} \frac{C_{d,turn}}{C_{D,turn}} \frac{C_{D,turn}}{V_{turn}} \frac{V_{turn}}{\hat{S}_{flight}} \quad (\text{A.17})$$

Additionally: one relationship is used to determine part of Equations A.16 and A.17, Equation A.18.

$$\begin{cases} \frac{\partial \hat{S}_{flight}}{\partial V_{turn}} \frac{V_{turn}}{\hat{S}_{flight}} = t_{turn} \frac{V_{turn}}{t_{turn} V_{turn} + t_{cruise} V_{cruise}} = \frac{t_{turn}}{t_{turn} + t_{cruise}} \frac{V_{cruise}}{V_{turn}} \\ \frac{\partial \hat{S}_{flight}}{\partial V_{cruise}} \frac{V_{cruise}}{\hat{S}_{flight}} = t_{cruise} \frac{V_{cruise}}{t_{turn} V_{turn} + t_{cruise} V_{cruise}} = \frac{t_{cruise}}{t_{turn} \frac{V_{turn}}{V_{cruise}} + t_{cruise}} \end{cases} \quad (\text{A.18})$$

For  $w_6$ , the expansion of Equation 3.56 results in Equation A.19.

$$w_6 = \frac{\partial W_{payload}}{\partial C_{l,climb}} \frac{C_{l,climb}}{W_{payload}} + \frac{\partial \hat{S}_{flight}}{\partial C_{l,climb}} \frac{C_{l,climb}}{\hat{S}_{flight}} + \frac{\partial h_{60s}}{\partial C_{l,climb}} \frac{C_{l,climb}}{h_{60s}} \quad (\text{A.19})$$

Neither payload weight nor flight distance depend on the lift coefficient during climb, using Equations 3.47 and 3.48, results in Equation A.20.

$$w_6 = \frac{\partial h_{60s}}{\partial V_V} \frac{\partial V_V}{\partial C_{L,climb}} \frac{\partial C_{L,climb}}{\partial C_{l,climb}} \frac{C_{l,climb}}{C_{L,climb}} \frac{C_{L,climb}}{V_V} \frac{V_V}{h_{60s}} \quad (\text{A.20})$$

In the same manner,  $w_7$  is calculated via Equation A.21.

$$w_7 = \frac{\partial h_{60s}}{\partial V_V} \frac{\partial V_V}{\partial C_{D,climb}} \frac{\partial C_{D,climb}}{\partial C_{d,climb}} \frac{C_{d,climb}}{C_{D,climb}} \frac{C_{D,climb}}{V_V} \frac{V_V}{h_{60s}} \quad (\text{A.21})$$

The relative derivative of altitude in 60s by vertical velocity is given by Equation A.22.

$$\frac{\partial h_{60s}}{\partial V_V} \frac{V_V}{h_{60s}} = t_{climb} \frac{V_V}{t_{climb} V_V} = 1 \quad (\text{A.22})$$

